MBE Growth of Semiconductor Quantum Structures with Type-II Band Alignment and CdSe Thin Films for Device Applications

by

Zheng Ju

A Dissertation Presented in Partial Fulfillment
of the Requirements for the Degree
Doctor of Philosophy

Approved October 2023 by the
Graduate Supervisory Committee:

Yong-Hang Zhang, Chair
David J. Smith
Shane R. Johnson
Fernando A. Ponce

ARIZONA STATE UNIVERSITY

December 2023

ABSTRACT

The first part of this dissertation focuses on quantum structures with type-II band alignment, which are designed for applications in infrared photodetection and optical nonlinearity. A short- and mid-wavelength infrared dual-band optically-addressed photodetector structure has been designed and fabricated by molecular beam epitaxy, which is used to demonstrate the operational principles of optical address for extended tri-band detection. High-resolution x-ray diffraction and photoluminescence measurement were used to characterize the samples and revealed excellent crystalline quality and optical properties. An analytical model has been developed to address the effects of luminescence coupling and light leakage effects in optically-addressed tri-band photodetectors in terms of the absorber thicknesses and photoluminescence quantum efficiencies.

Beyond superlattices, asymmetric quantum wells with type-II band alignment find application in optical nonlinearity enhancement which is the result of increased wavefunction overlap and larger electric dipole moments of the interband transitions compared to the conventional structures with type-I band edge alignment. The novel type-II AQW structure exhibits interband second-order susceptibility tensor elements ranging between 20 pm/V to 1.60×10^3 pm/V for nearly-resonant optical rectification and difference frequency generation applications at near-infrared and terahertz wavelengths, an improvement of nearly one order of magnitude over the type-I structures and one to three orders of magnitude over natural crystals such as $LiNbO_3$, KTP, or GaAs. A factor of 2-3 further enhancement of the tensor elements is achieved by optimizing the well widths and band offsets of the type-II asymmetric quantum wells.

The second part of the dissertation reports the study of CdSe thin films with mixed zincblende and wurtzite phases grown on lattice-matched InAs(100) substrate using molecular beam epitaxy. These CdSe thin films reveal single-phase zincblende (ZB) structure with high crystalline quality with low defect density. In contrast, CdSe layers grown on lattice-matched InAs(111)B (As-terminated) substrates under different growth temperatures and Cd/Se flux ratios all have their demonstrated mixed ZB and wurtzite phases in coexistence confirmed by high-resolution x-ray diffraction, transmission electron microscopy and photoluminescence measurements. The reason for these properties is due to the small formation energy difference between the ZB and WZ phases of CdSe, which has been confirmed by density functional theory simulations.

ACKNOWLEDGMENTS

I am profoundly grateful to my advisor, Professor Yong-Hang Zhang, for his unwavering support, guidance, and expertise throughout this research journey. His mentorship, vision and dedication have been instrumental in shaping the direction of my research and encouraging me to adopt a broader perspective in my future career. I would like to extend my appreciation to Professor David J. Smith whose teachings, feedback, and insights have enriched my academic experience and contributed significantly to my research work. I would also like to express my gratitude to Dr. Shane Johnson for generously sharing his invaluable expertise in molecular beam epitaxy and guidance on repairing and maintenance of the equipment, and Professor Fernando A. Ponce for his exceptional teaching and sharing his industrial experience and advice.

I would like to thank my senior colleagues and formal group members, Professor Yang Zhang, Dr. Cheng-Ying Tsai, Dr. Stephen Schaefer, Dr. Jia Ding, Dr. Calli Campbell, and Dr. Maxwell Lassis. Their mentorship and training have made me a proficient MBE grower and an independent researcher. I would also like to thank current group members, Tyler McCarthy, Xin Qi, Allison McMinn, Xiaoyang Liu and Razine Hossein for their help in material characterization, machine maintenance and theory discussion.

I would like to thank the ASU NanoFab staff, Kevin Hilgers, Kevin Norquist, Scott Ageno, Carrier Sinclair and Jaime Quintero who have provided professional semiconductor process, mask design, and consultation. I would like to show my appreciation to my best friends and roommates Dr. Han Li and Dr. Shujie Fan for the constructive discussions, their support, and their companionship over the past five years. I would also like to thank my great friends Dr. Jing Bai, Dr. Yanze Wu, Shi Lu, Ziyi He,

Ziyi Wang, Ting-An Yen, Fan Zhang, Sida Xue and Yuhong Lu for enriching my academic and personal life.

Finally, I would like to extend my deepest gratitude to my parents Qian Ju and Dongmei Zhao and my grandparents Juhua Chen and Chengde Zhao for their support, encouragement, and sacrifices throughout my academic journey. Their endless love and belief in me have been a constant source of motivation and inspiration.

This work was financially supported partially by Center for the U.S. Office of Naval Research, Army Research Office, First Solar Inc, Applied Materials Inc., and Northrop Grumman Corporation. I also acknowledge the use of high-resolution X-ray diffraction system in the LeRoy Eyring Center for Solid State Science at Arizona State University.

TABLE OF CONTENTS

Page

LIST OF TABLES

LIST OF FIGURES

Figure Page

Figure Page

Figure Page

LIST OF ACRONYMS

ACQW – asymmetric coupled quantum well

ASQW – asymmetric stepped quantum well

CSS – closed-space sublimation

CB – conduction band

DFT – density functional theory

DH – double-heterostructure

DGF – difference frequency generation

FFT – fast Fourier transform

IB – interband

IR – infrared

ISB – intersubband

LWIR – long- wavelength infrared

LWSL – long- wavelength infrared superlattice

MOCVD – metal-organic chemical vapor deposition

MWIR – mid- wavelength infrared

MWSL – mid- wavelength infrared superlattice

MBE – molecular beam epitaxy

NEP – noise equivalent power

OR – optical rectification

PL – photoluminescence

RHEED – reflection high-energy electron diffraction

SEM – scanning electron microscopy

SFG – sum frequency generation

SHG – second-harmonic generation

SIMS – secondary ion mass spectrometry

SSPL – steady-state photoluminescence

SWIR – short-wavelength infrared

TEM – transmission electron microscopy

TRPL – time-resolved photoluminescence

T2SL – type-II superlattice

UHV – ultra-high vacuum

VB – valence band

WZ – wurtzite

XRD – x-ray diffraction

ZB – zincblende

CHAPTER 1

INTRODUCTION

1.1 Background

The discoveries of heterojunctions and superlattices (SL) have garnered immense interests from researchers and scientists.[1,2] Numerous optoelectronics applications such as light-emitting diodes (LEDs), quantum cascade lasers (QCLs), solar cells and quantum-well infrared photodetectors (QWIPs) have been invented by using synthetic semiconductor quantum structures.[3] Epitaxial growth techniques, such as MBE and metal-organic chemical vapor deposition (MOCVD), have proven their ability to produce high-quality, dislocation-free epitaxial films on lattice-matched commercial substrates, enabling the manufacture of various types of devices mentioned above.[4]

The bandgap vs. lattice constant diagram of common semiconductors is illustrated In Fig. 1; many cost-effective, commercially available substrates enabled the growth of lattice-matched binary and ternary compounds. For instance, materials like MgS, AlAs, and ZnSe, which share a similar lattice constant of 5.62 Å, can be effectively grown on Ge or GaAs substrates. A similar approach can be extended to materials like ZnTe, CdSe, and AlSb, which can be grown on InAs or GaSb substrates with a lattice constant of 6.1 Å, as well as CdTe, MgTe, HgTe, and α-Sn, which can be grown on InSb substrates with a lattice constant of 6.5 Å. The extensive range of heterovalent epitaxial growth techniques involving the monolithic integration of III-V, II-VI, and IV-VI semiconductors offers the capability for the desirable bandgap- and wavefunction-engineering for novel device designs with new functionalities. Additionally, the observation and prediction of intriguing low-dimensional quantum phenomena should be noteworthily highlighted, such as the two-

dimensional electron gas (2DEG) and the electrical field-induced topological insulator (TI), occurring at the heterovalent interfaces of IV, II-VI, and III-V compound semiconductors due to their distinct electronic configurations.[5]

In contrast to indirect bandgap materials like Silicon and Germanium, III-V and II-VI materials with direct bandgaps possess significantly higher absorption coefficients. The property renders them better suited and preferred for high-efficiency optoelectronic devices. Additionally, as illustrated in FIG. 1, the bandgaps of III-V and II-VI semiconductors can cover a broad spectrum from ultra-violet (UV) to very long wavelength IR. Certain compounds, like HgTe and HgSe, are known to exhibit a zero bandgap.

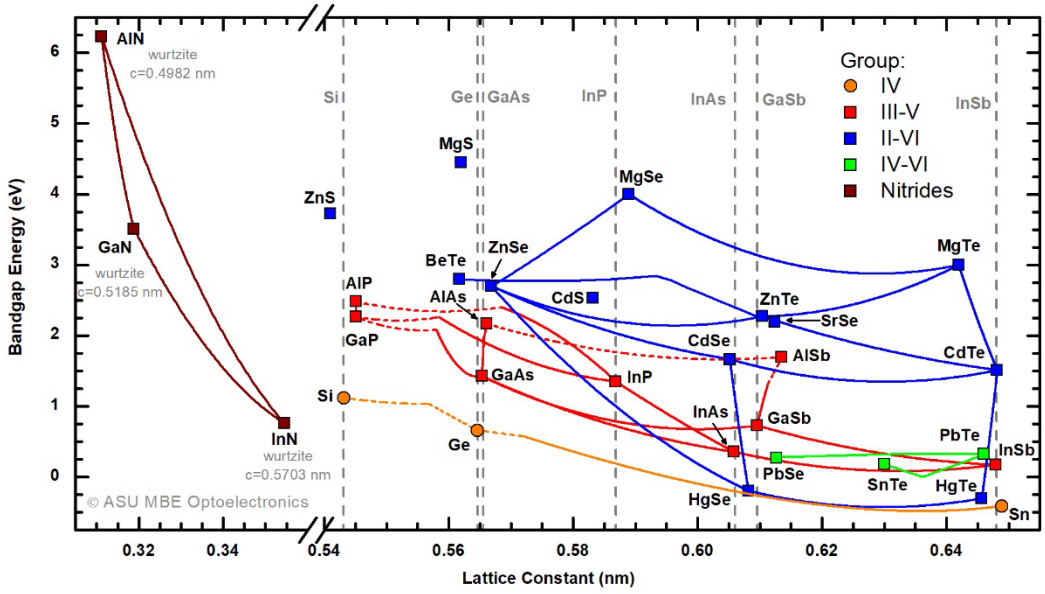

FIG. 1. A diagram for the bandgap energies vs. lattice constants of common semiconductors. The dashed grey line indicates the corresponding lattice constants of commercially available substrates.

1.2 Infrared Photodetector Technology

Infrared (IR) radiation is defined as electromagnetic radiation with wavelengths ranging from 780 nm to 1 mm. This range can be categorized into the following sub-ranges: (1) near infrared (NIR), 0.78 μm to 1.4 μm; (2) short-wavelength infrared (SWIR), 1.4 μm to 3 μm; (3) mid-wavelength infrared (MWIR), 3 μm to 5 μm; (4) long-wavelength infrared (LWIR), 8 μm to 12 μm; (5) very long-wavelength infrared (VLWIR), 12 μm to 1000 μm.[6] The radiation intensity and its spectral distribution from a blackbody in thermal equilibrium at a certain temperature are described by the Planck's law, which gives the spectral density of radiation per unit wavelength per unit area. The Planck's law is formulated in the followings:

$$B_\lambda(\lambda, T) = \frac{2\pi hc^2}{\lambda^5} \frac{1}{e^{hc/\lambda kT} - 1} \ (\mathrm{W \cdot cm^{-2} \mu m^{-1}}) \tag{1}$$

$$B_p(\lambda, T) = \frac{2\pi c}{\lambda^4} \frac{1}{e^{hc/\lambda kT} - 1} \ (\mathrm{photons \cdot s^{-1} cm^{-2} \mu m^{-1}}), \tag{2}$$

where λ is the wavelength, T is the temperature, h is the Plank's constant, c is the speed of light, and k is the Boltzmann's constant. With temperature increases, the total amount of energy emitted at any wavelength increases while the wavelength of peak emission blue-shifts. Derived from Eq. 1 and 2, the Wien displacement law for maximum energy and for maximum photons can be obtained as Eq. 3 and 4:

$$\lambda_{\mathrm{mw}} \mathrm{T} = 2898 \ (\mu\mathrm{m \cdot K}) \quad \text{For energy}_{\max} \tag{3}$$

$$\lambda_{\mathrm{mp}} \mathrm{T} = 3670 \ (\mu\mathrm{m \cdot K}) \quad \text{For photons}_{\max} \tag{4}$$

For instance, the sun, which closely approximates a blackbody (or grey body) due to its temperature of 6000 K, emits a continuous spectrum with a peak in the visible light range.

For the object at ambient temperature of 300 K , λ_{mw} and λ_{mp} are at 9.66 and 12.2 μm, respectively.

Infrared photodetector technology is among the most vital technologies in defense and commercial applications. It plays a pivotal role in sensing and imaging, encompassing tasks like target aiming, detection, and enhancing night vision capabilities. Significant progress in IR photodetector technology did not occur until the 1950s. Lead-salt detectors, extrinsic Silicon photoconductive detectors, and narrow-bandgap semiconductors were reported for IR detection applications. Lead-salt materials like PbS and PbSe continue to be the most used options for low-cost photoconductive detectors in numerous applications within the 1-5 μm spectral range to this day. [7-9].

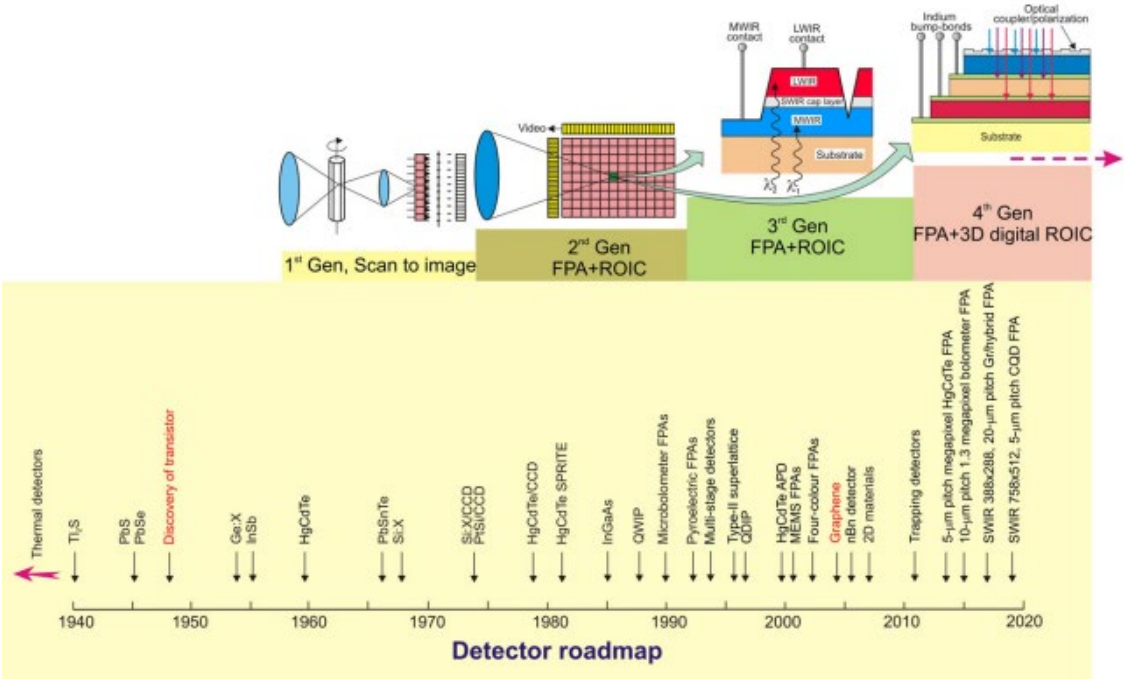

FIG. 2. History of infrared detector and system development[10]

In 1959, Lawson and his colleagues made a breakthrough by discovering HgCdTe (MCT) alloys with adjustable bandgaps. These MCT-based photodetectors outperformed

extrinsic silicon and lead-tin telluride devices of that era and remain the leading choice for IR photodetectors today.[9] The MCT ternary-alloy system offers a wide range of flexibility in detector design, allowing for the tuning of bandgaps spanning from the MWIR range of 1-3 μm to the LWIR range of 8-15 μm.[9] This discovery sparked the development of detector devices such as scanning systems, staring system-electronically scanned, staring systems with large numbers of pixels, multi-color functionality, etc. These advancements are summarized in FIG. 2.[10] With over 60 years of research and development, the growth and fabrication processes of the MCT ternary-alloy system have become well established. Additionally, there have been substantial enhancements in crystalline quality, and a deeper understanding of physics has been achieved, including surface properties and band structures. In LWIR MCT detectors, the minority carrier lifetime is constrained primarily by intrinsic Auger recombination. The small effective mass results in a lower limit of tunneling currents, which in turn may limit the range of wavelengths that can be effectively detected, particularly in the longer wavelength range.[11]

1.3 Type-II Superlattices

Fig. 3 shows heterojunctions can be classified into three main types, namely Type-I (straddling gap), Type-II (staggered gap), and Type-III (broken gap), based on the band alignment at the interface between adjacent layers.[12] Type-II (staggered gap) means both the conduction band edge and the valence band edge of one material are lower than both band edges of the other material. Therefore, electrons are localized within one material, while holes are localized within the other material. Type-II superlattices (T2SLs) were first proposed by Sai-Halasz *et al.* and subsequently realized by Sakaki *et al.* at the IBM T. J. Watson Research Center in 1977 by stacking multiple layers with staggered gaps using the same materials [13,14]. By modifying either the composition or the layer thickness of the superlattice, it is possible to control the process through which electronic subbands are formed. This, in essence, constitutes effective bandgap engineering. The band alignment at the interface between neighboring semiconductor layers has a more significant effect on tuning the effective bandgap compared to varying the layer thickness.

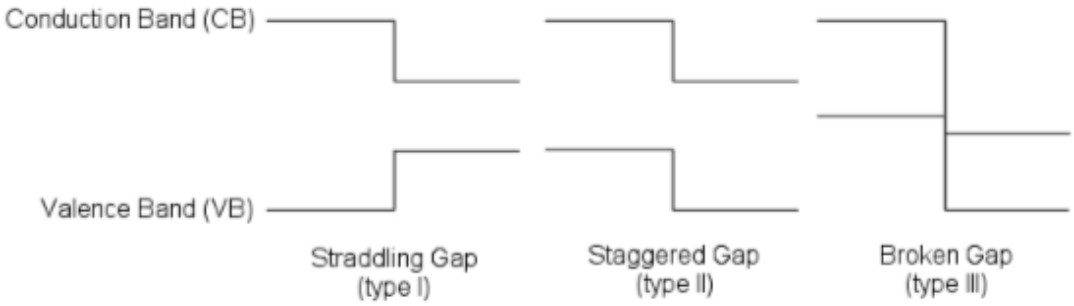

FIG. 3. Three types of band alignment for semiconductor heterojunction [12]

Type-II superlattices (T2SLs) have been demonstrated by using nearly lattice-matched materials like InAs/GaSb and InGaAs/GaAsSb for infrared detectors. The InAs/GaSb

T2SLs have several properties which makes them suitable for infrared detectors and offer an alternative low-cost approach to its counterpart HgCdTe, in terms of lower band-to-band tunneling due to larger electron effective masses and surface leakage currents and suppressed Auger recombination, enabling higher operation temperatures and longer wavelength.[15] Nevertheless, despite decades of research, the limitations of InAs/GaSb T2SLs have become apparent: It is challenging to achieve significant thickness in T2SLs on InAs or GaSb substrates without the introduction of metamorphic buffer layers or strain-compensated structures.[16] Furthermore, the material's lifetime falls short of its theoretical potential, which impedes its further advancement for use in optoelectronic devices. [17,18]

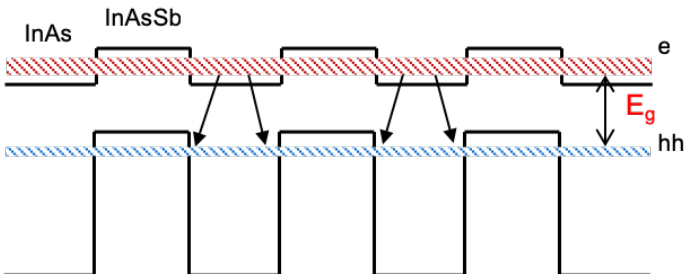

FIG. 4. Band edge diagram and mini-bands of $InAs/InAs_{1-x}Sb_x$ T2SLs. The transition energy can be tunable by changing period thickness and Sb composition.[19]

The schematic diagram of the band edge alignment for an $InAs/InAs_{1-x}Sb_x$ T2SL known as Ga free T2SLs is depicted in FIG. 4, and its adjustable bandgaps are illustrated in the photoluminescence spectra measured at 12K, as presented in FIG. 5(a).[19] An increase in either the thickness of the InAs layers or the Sb composition in the InAsSb layers will lead to a reduction in the effective bandgap of the materials. $InAs/InAs_{1-x}Sb_x$ T2SLs can achieve strain-balance to a GaSb substrate with fixed thicknesses for InAs and $InAs_{1-x}Sb_x$ layers as the former is tensile while the latter (with $x > 0.09$) is compressive strained. Hence, in theory, strained-balanced $InAs/InAs_{1-x}Sb_x$ T2SLs can be grown to an

infinite thickness on GaSb substrates without generating misfit dislocations. FIG. 5(b) shows the HRXRD (004) $\omega - 2\theta$ profile and simulation for a sample which consists of a strain-balanced MWSL InAs/$InAs_{1-x}Sb_x$ T2SL and a LWSL InAs/$InAs_{1-x}Sb_x$ T2SL. The MWSL region is 4.5 μm thick and comprises unintentionally doped n-type 2.14 nm/1.5 nm InAs/$InAs_{0.782}Sb_{0.218}$ T2SLs. The LWSL region is composed of 100-nm-thick undoped 9.78 nm/4.22 nm InAs/$InAs_{0.7}Sb_{0.3}$ T2SLs.[20] Discovered by Prins *et al.* in 2012, the main reason for "Ga-free" InAs/InAsSb T2SLs to have long lifetime over conventional InAs/GaSb T2SLs with gallium was unveiled. The defect energy levels in InAs/InAsSb T2SLs are predominantly located in the conduction band. Consequently, these defect levels do not function as Shockley-Read-Hall recombination centers, unlike the case in the traditional InAs/GaSb T2SLs. This absence of recombination centers results in a longer carrier lifetime.[21] This material system gained further recognition due to the achievement of a record carrier lifetime exceeding 400 ns experimentally.[22] This lifetime improvement represents a remarkable advancement, surpassing conventional InAs/GaInAs T2SLs by more than one order of magnitude.[22] These advantage of the Ga-free T2SLs materials makes it ideal for future IR photodetector applications.[21]

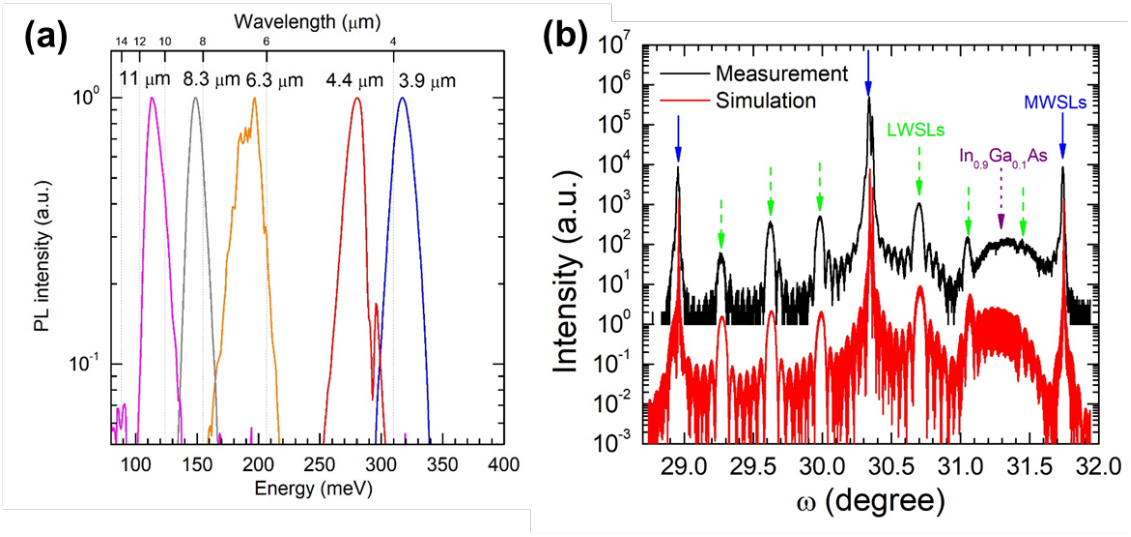

FIG. 5. (a) Normalized 12 K PL spectra from InAs/$InAs_{1-x}Sb_x$ T2SLs samples to show the tunable bandgaps. The discontinuities at 200 and 290 meV are the results of CO_2 absorption. [19] (b) $\omega - 2\theta$ XRD of a sample which consists of two strain-balanced T2SLs. [20]

1.4 Ga-Free InAs/InAsSb Type-II Superlattice Photodetectors

FIG.6 provides a concise timeline-style overview of the evolution of T2SLs, including the progression of InAs/InAsSb T2SLs.[23] Until 2010, the InAs/InAsSb system received significantly less attention compared to the InAs/GaSb system. However, over the past decade, there has been a swift advancement in their fabrication, primarily attributed to their exceptional defect tolerance and resilient material properties. Most T2SL devices have traditionally been produced using MBE. However, there has been a growing interest in utilizing MOCVD for T2SL growth, driven by its potential for more cost-effective and higher throughput.[24,25] Significant advancements in the development of $InAs/InAs_xSb_{1-x}$ T2SLs detectors and FPAs have been made by many research groups: such as the Jet Propulsion Laboratory (JPL) , the research group led by Prof. Razeghi at Northwestern University and the research group led by Prof. Zhang at Arizona State University. These research groups have demonstrated the $InAs/InAs_xSb_{1-x}$ T2SL based photodetectors with operating cutoff wavelength from 5 to 14μm which surpasses the limitations of traditional bulk III-V IR detectors based on InGaAs and InSb. The primary technological challenge for the fabrication of superlattice-based devices is the growth of the materials, especially of the high-quality absorbers with sufficient thickness to achieve high efficiency. In the case of InAs/InAsSb T2SL photodetectors, a 5 μm thick absorber is typically enough to achieve a sufficiently high quantum efficiency (QE). This thickness can yield a QE of approximately 50% due to the longer effective lifetime and diffusion length, when compared to InAs/GaSb T2SL photodetectors. Table 1 compiles information from various literature sources regarding InAs/InAsSb-based T2SL IR photodetectors. Key industry leaders like IQE and Teledyne have reported astonishingly high peak quantum efficiency

up to 72% in MWIR InAs/$InAs_xSb_{1-x}$ T2SL photodetectors.[34,41] Additionally, they have achieved over 50% peak quantum efficiency from the devices fabricated on high-index GaSb wafers.[42] InAs/$InAs_xSb_{1-x}$ T2SL photodetectors are primarily fabricated in two configurations: p-n junction photodiodes and barrier detectors. The operational principle of barrier detectors involves enabling the passage of one type of carrier (either electrons or holes) while obstructing the other, which is why they are referred to as "unipolar barriers." Consequently, the unipolar barrier concept assumes a nearly zero offset approximation within one band and a substantial barrier in the other band throughout the heterostructure. Among various types of unipolar barrier detectors, the nBn detector is the most widely favored.[23] The InAs/InAsSb T2SL photodiodes are mainly based on conventional p-i-n heterostructures. The advantage of the structure is that the low minority carrier concentration in high bandgap materials enables the suppression of diffusion dark current and yields higher R_dA product and detectivity. Compared to p-n junction InAs/InAsSb T2SL photodiodes, SLs barrier structures are more generally efficient. *Kim et al.* demonstrated the first InAs/InAsSb T2SL based nBn IR photodetectors in 2013 with the operating cutoff wavelength 13.2 μm and 0.24 A/W responsivity. After then, the InAs/InAsSb T2SL-based nBn structure underwent significant development and was later adopted for the F-35 fighter aircraft in 2018 as part of the VISTA program.[26]

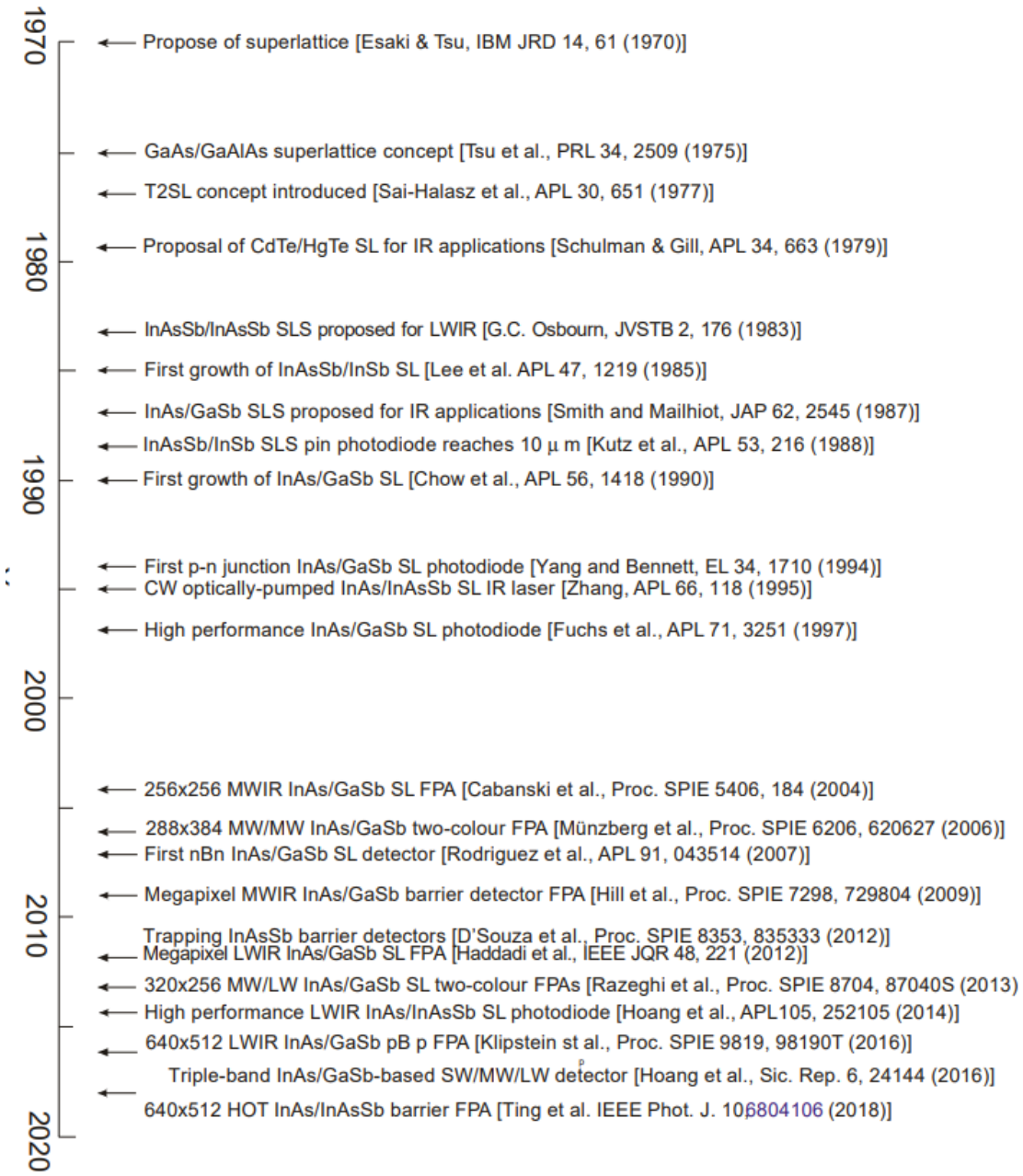

FIG. 6. Roadmap development of T2SL IR photodetectors including InAs/InAsSb photodetectors [23]

The barrier structure photodetector design (nBn or pBp) is also capable of multiband detection. Krishna *et al.* have demonstrated dual-band barrier detectors based on nBn or pBp InAs/GaSb SL.[27,28] Razeghi *et al.* later presented InAs/InAsSb T2SL nBn

and pBp photodetectors with improved performance.[29,30] Dual-band barrier structures can be relatively easily produced, mainly because of the highly advanced III-V materials growth techniques. A typical dual-band barrier T2SLs detector comprises two narrow bandgap absorbers that are optimized for two distinct IR spectral regions. These absorbers are separated by a wide bandgap barrier layer, typically around 0.1 μm thick. This architecture effectively blocks the majority carrier current flow between the two electrodes due to the substantial energy offset. However, it poses no barrier for the photo-generated minority carriers. Both barriers should be characterized by negligibly small valence band (VB) or conduction band (CB) discontinuities with respect to both materials. The regions corresponding to the absorbers (channels) are selectively activated based on the polarity of the applied voltage.

Table 1. Ga-free InAs/InAsSb superlattice infrared detectors and their reported performance

Composition	SL period [nm]	Polarity [n,i,p]	Aperture size [μm]	Absorber thickness [μm]	T_{op} [K]	λ_c	J_d [A/cm^2], T_{op} [K], V_{bias}[V]	Responsivity [A/W] or QE	Detectivity [cm Hz$^{1/2}$/W]	Reference
InAs/InAs$_{0.62}$Sb$_{0.38}$	18.4	nBn	S=410	2.2	77	13.2	5×10^{-4}, 77, -0.3	R=0.24A/W	1×10^{8}	Kim et al.[26]
InAs/InAs$_{0.57}$Sb$_{0.43}$	14.7	pN	d=100-400	2.3	77	14.6	0.7, 77, -0.3	R=4.8A/W; QE~46%	4.6×10^{11}	Hoang et al.[31]
InAs/InAs$_{0.45}$Sb$_{0.55}$	10.5	nBn	S=100-400	2,6	77	10	4.4×10^{-4}, 77,-0.09	R=3.5A/W; QE~54%	2.8×10^{11}	Haddadi et al.[32]
InAs/InAs$_{0.48}$Sb$_{0.52}$	10.5	nBn	S=100-400	2	77	10	5.7×10^{-5}, 77. -0.08	R=2.25A/W; QE~40%	1.6×10^{11}	Haddadi et al.[30]
InAs/InAs$_{0.50}$Sb$_{0.50}$	12	nBn	S=100-400	2	77	10	8×10^{-5}, 77. -0.08	R=2.65A/W; QE~43%	4.7×10^{11}	Haddadi et al.[33]
InAs/InAsSb	-	-	d=0.25,1	-	208	5.0	1×10^{-4}, 208, -0.3	R=1.35A/W	2.6×10^{10}	Teledyne [34]
InAs/InAs$_{0.65}$Sb$_{0.35}$	5.5	nBn	d=60…310	3	150	4.6	4×10^{-5}, 150, -2.5			Perez et al.[35]
InAs/InAs$_{0.66}$Sb$_{0.34}$	5	nBn	S=250	2.6	150	5.4	4.5×10^{-5}, 150, -0.2	QE~52%	4.5×10^{11}	Ting et al.[36]
InAs/InAs$_{0.66}$Sb$_{0.34}$	12	pin	S=400	2	77	8.0	9×10^{-4}, 77, -0.02	R=1.26A/W; QE~21%	4.6×10^{11}	Wu et al.[24]

InAs/InAs$_{0.65}$Sb$_{0.35}$	5.15	nBn	d=60…310	3	150	5	1×10^{-3}, 150, -0.5	-	-	Durlin et al. on Si[37]
InAs/InAs$_{0.50}$Sb$_{0.50}$	7.4	pBn	d=100-400	2.1	150	4.4	1.16×10^{-5}, 150, -0.05	R=1.48A/W; QE=47%	7.1×10^{11}	Wu et al.[38]
InAs/InAs$_{0.84}$Sb$_{0.16}$	13.3	nBn	d=50	4	200	5.5	1×10^{-2}, 150, -0.1	R=0.88A/W; QE=25%	1.5×10^{10}	Delli et al. **on Si**[39]
InAs/InAs$_{0.8}$Sb$_{0.2}$	13.5	pn	d=320	1	150	4.5	9.1×10^{-6}	R=0.78A/W; QE=25%	3.4×10^{11}	Wu et al.[40]
InAs/InAs$_{0.6}$Sb$_{0.4}$	5.5	niBn	d=1000	-	295	5.5	1.17, 295, -0.3V	R=2.47A/W; QE=72%	1.93×10^{9}	Kim, Teledyne [41]
InAs/InAs$_{0.482}$Sb$_{0.518}$	5.6	nBn	S=160-500	4.5	150	5.8	3.0×10^{-4}, 150, -0.1	QE~57%	-	Lubyshev, IQE[42]
InAs/InAs$_{0.478}$Sb$_{0.522}$	5.45	nBn	S=160-500	4.5	150	5.7	1.0×10^{-4}, 150, -0.1	QE~59%	-	Lubyshev, IQE **on GaSb (311)A**[42]
InAs/InAs$_{0.52}$Sb$_{0.48}$	5.43	nBn	S=160-500	4.5	150	6.7	8.7×10^{-4}, 150, -0.3	QE~57%		Lubyshev, IQE **on GaSb (211)B**[42]
InAs/AlAsSb/InAs/InAsSb/AlAsSb/InAs	-	p-i-n	S=100-400	1	300	1.8	9.6×10^{-5}, 300, -0.05	R=0.47A/W; QE=37%	6.45×10^{10}	Haddadi et al.[43]

1.5 Second-Order Susceptibility in Type-II Quantum Wells

In addition to type-II superlattices, quantum wells with type-II alignment have also captured the attention of researchers in enhancing optical nonlinearity. Material development for nonlinear optics is a field with long history and great potential since 60s. The second order nonlinear susceptibility $\chi^{(2)}$ is the strongest among optical nonlinearities and is used extensively in frequency up/down conversion, parametric generation[44], and electro-optic modulation[45]. While virtually all materials, crystalline or amorphous, possess third order nonlinear susceptibility $\chi^{(3)}$, only crystalline materials without centro-symmetry have substantial $\chi^{(2)}$. It has been proven that highly asymmetric covalent bonds increase the $\chi^{(2)}$ in compound semiconductor materials such as ZnSe, GaAs, InP, etc.[46] Unfortunately, due to the difficulty of achieving phase-matching (PM), these crystals are not widely used. The existing bulk phase-matchable nonlinear crystals such as $LiNbO_3$ or KTP have $\chi^{(2)}$ values far from theoretical upper bounds, especially in the near-IR (NIR) to UV range[47,48]. Man-made structures such as asymmetrical quantum wells (AQWs) with intersubband (ISB) transitions[49-53] have been proposed as an effective way to achieve high $\chi^{(2)}$ by engineering the asymmetric charge distributions, emulating polar bonds on a larger length scale[52-57]. However, current $\chi^{(2)}$ enhancement achieved in III-V AQWs [58,59] is limited to the mid-IR (MIR) due to small band offsets [56,58,59], and the palette of functional materials with large $\chi^{(2)}$, especially in the NIR to UV range remains sparse and practically unchanged since the 1990s.

The formal definition of the second-order nonlinear optical susceptibility $\chi^{(2)}$ relates the polarization of the medium to the incident electric field vector [59]:

$$P_i(\omega_n + \omega_m) = \varepsilon_0 \sum_{j,k} \sum_{(n,m)} \chi^{(2)}_{ijk}(\omega_n + \omega_m, \omega_n, \omega_m) E_j(\omega_n) E_k(\omega_m) \tag{5}$$

The second-order susceptibility is a third-rank tensor with components i, j, k. The polarization P_i oriented in the $\boldsymbol{r_i}$ direction is thus given by the frequency-dependent $\chi^{(2)}_{ijk}$ tensor element and the product of incident electric fields $E_j(\omega_n)$ and $E_k(\omega_m)$ directed in the $\boldsymbol{r_j}$ and $\boldsymbol{r_k}$ directions. The summation extends over all permutations of input field frequencies ω_n and ω_m with the sum $\omega_n + \omega_m$ held fixed, and over all tensor elements of the incident electric field. There are in general 4 different physical processes related to the second-order nonlinear optical susceptibility $\chi^{(2)}$ [59]:

$$P_i(2\omega_n) = \varepsilon_0 \sum_{j,k} \sum_{n} \chi^{(2)}_{ijk}(2\omega_n, \omega_n, \omega_n) E_j(\omega_n) E_k(\omega_n) = \varepsilon_0 \chi^{(2)} E_n^2 \text{ (SHG)} \tag{6}$$

$$P_i(\omega_n + \omega_m) = \varepsilon_0 \sum_{j,k} \sum_{(n,m)} \chi^{(2)}_{ijk}(\omega_n + \omega_m, \omega_n, \omega_m) E_j(\omega_n) E_k(\omega_m) \tag{7}$$

$$= 2\varepsilon_0 \chi^{(2)} E_1 E_2 \text{ (SFG)}$$

$$P_i(\omega_n - \omega_m) = \varepsilon_0 \sum_{j,k} \sum_{(n,m)} \chi^{(2)}_{ijk}(\omega_n - \omega_m, \omega_n, -\omega_m) E_j(\omega_n) E_k(-\omega_m) \tag{8}$$

$$= 2\varepsilon_0 \chi^{(2)} E_1 E_2^* \text{ (DFG)}$$

$$P_i(0) = \varepsilon_0 \sum_{j,k} \sum_{(n,m)} \chi^{(2)}_{ijk}(0, \omega_n, \omega_m) E_j(\omega_n) E_k(\omega_m) \tag{9}$$

$$= 2\varepsilon_0 \chi^{(2)} (E_1 E_1^* + E_2 E_2^*) \text{ (OR)}$$

Where SHG denotes second-harmonic generation, SFG is sum frequency generation, DFG is difference frequency generation, and OR is optical rectification.

The optical response of the medium for DFG can be maximized by carefully engineering the AQW structure to make use of resonance. “Resonance” denotes the

condition where the electric field frequencies ω_n and/or ω_m approach a real transition frequency in the AQW structure, e.g. intersubband transitions or interband transitions. Transitions can be further classified as (i) singly resonant where one field frequency ω_n is resonant and the other component is non-resonant, and (ii) doubly resonant where both ω_n and ω_m are resonant with transition frequencies in the AQW. [59]

The simplest application is non-resonant difference frequency generation where both input frequencies ω_1 and ω_2 are much smaller than the interband transition frequencies, which are on the order of ~1 eV. It is important to note that the input field frequencies may still approach or exceed resonance with the intersubband transition frequencies, which are on the order of ~10-100 meV in typical type-II AQWs. The $\chi^{(2)}$ tensor elements are given as $\chi_{ijk}^{(2)}(\omega_1 - \omega_2, \omega_1, -\omega_2)$ with $\omega_1, \omega_2 \ll \omega_0$, where ω_0 is the smallest interband (or intersubband) transition frequency. Off-resonant optical rectification is simply the case where $\omega_1 = \omega_2$ and $\omega_1, \omega_2 \ll \omega_0$. Off-resonant DFG is illustrated in Fig. 7 for a typical type-II AQW band structure. [59]

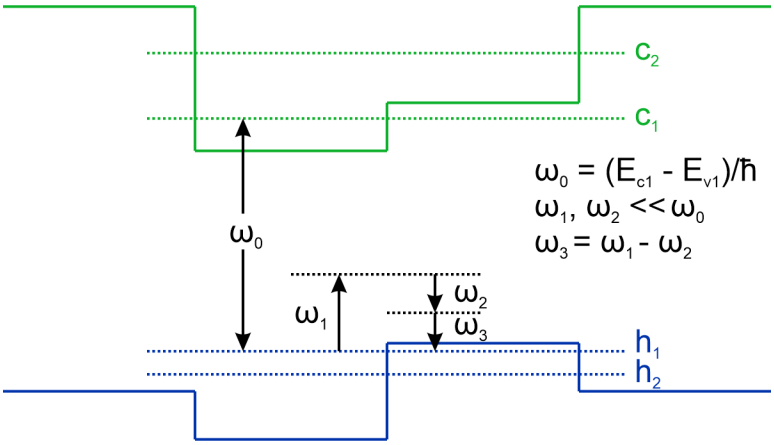

FIG. 7. Schematic diagram of off-resonant difference frequency generation. The electric field frequencies ω_1 and ω_2 are much smaller than the interband resonant frequency ω_0.

Singly-resonant difference frequency generation makes use of the large increase in $\chi^{(2)}$ in interband type-II AQWs as the field frequency approaches the interband resonance, typically on the order of ~1 eV. Only one field component approaches resonance; the other field components are off-resonant from all other transition frequencies (both interband and intersubband).[58] It is convenient to describe the input frequencies in terms of the detuning $\delta\omega$ from the interband resonance frequency ω_0:

$$\omega_0 = \omega_1 - \omega_2 + \delta\omega \tag{10}$$

Where the negative sign in front of ω_2 denotes difference frequency generation. In the limit as $\delta\omega \to 0$ full resonance is achieved; however, this results in large interband absorption and high loss. Typical operation therefore utilizes small detuning $\delta\omega$ of ~10-100 meV such that absorption losses are minimal, but the magnitude of $\chi^{(2)}$ is enhanced. Singly-resonant optical rectification is the special case where $\omega_1 = \omega_2$ and $\omega_1, \omega_2 \cong \omega_0$. Off-resonant DFG is illustrated in Fig. 8 for a typical type-II AQW band structure.

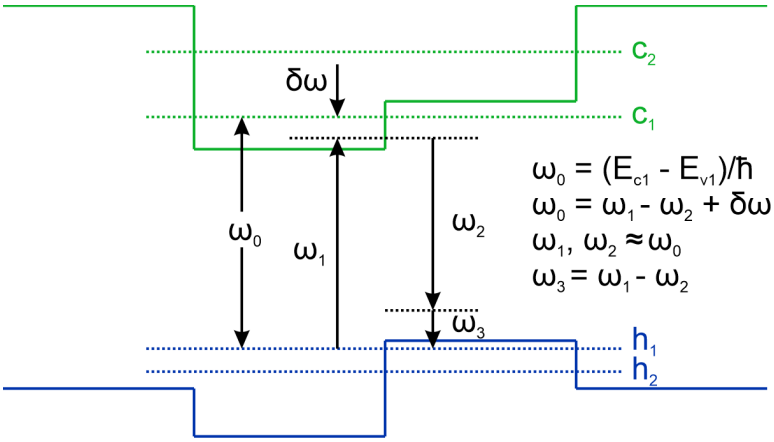

FIG. 8. Schematic diagram of singly-resonant difference frequency generation. The electric field frequencies ω_1 and ω_2 are detuned from the interband resonant frequency ω_0 by an amount $\delta\omega$.

Doubly-resonant difference frequency generation makes use of the large increase in $\chi^{(2)}$ in interband type-II AQWs as one field frequency approaches the interband resonance, typically on the order of ~1 eV, and the second field frequency approaches the intersubband resonance, typically on the order of ~10-100 meV. The double resonances greatly increase the maximum achievable $\chi^{(2)}$ and are suitable for DFG applications with a pump laser wavelength on the order of the interband transition resonance $\omega_{0,IB}$ and THz output wavelengths on the order of the intersubband transition resonance $\omega_{0,ISB}$. Define the IB and ISB detuning frequencies as[59]:

$$\omega_{0,IB} = \omega_1 + \delta\omega_1 \tag{11}$$

$$\omega_{0,ISB} = \omega_2 + \delta\omega_2 \tag{12}$$

The difference frequency $\omega_3 = \omega_1 - \omega_2$ is known as the "idler" frequency and is a by-product of the THz (IR) difference frequency generation. By carefully adjusting the AQW potential profile, the IB and ISB resonances can be tuned to align with the desired pump laser and THz (IR) frequencies ω_1 and ω_2. Doubly-resonant DFG is illustrated in Fig. 9

for a typical type-II AQW band structure, where the THz (IR) intersubband resonance is placed in the conduction band.

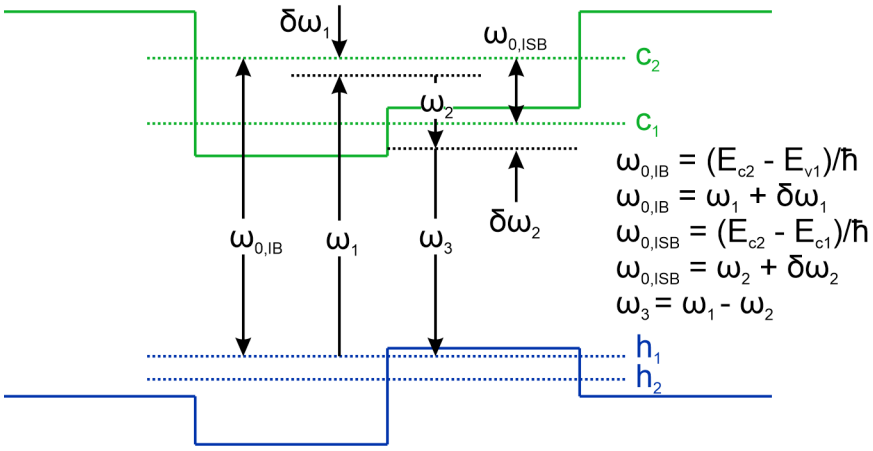

FIG. 9. Schematic diagram of doubly-resonant difference frequency generation. The electric field frequency ω_1 is detuned from the interband resonant frequency $\omega_{0,IB}$ by an amount $\delta\omega_1$, and the frequency ω_2 is detuned from the intersubband resonant frequency $\omega_{0,ISB}$ by an amount $\delta\omega_2$.

1.6 CdSe and its Application to Solar Cells

A typical thin-film solar cell consists of a polycrystalline II-VI alloy (such as CdSe, MgCdTe, or ZnCdTe) as the top cell in a tandem structure with a crystalline Si bottom cell. This design has the potential to achieve power conversion efficiencies exceeding 30% at concentrations below 50 suns.[60] CdSe, possessing the wurtzite (WZ) crystal structure, has a bandgap energy of 1.71~1.74 eV at room temperature,[61-63] making it an excellent choice for the top cell, as the ideal bandgap for the upper II-VI cell in combination with Si is 1.73 eV. The theoretical power conversion efficiency of CdSe/Si tandem solar cells can reach up to 40%,[60] and it still exceeds 30% even with minority carrier lifetimes in the upper CdSe cell as short as 1 ns, a readily achievable characteristic even in polycrystalline thin-film II-VI materials.[64] For effective absorption of sunlight, high-quality CdSe films up to 1 μm in thickness are desired, given that the absorption coefficient of WZ CdSe at 1.72 eV is 4.19×10^4 cm^{-1},[65] resulting in an absorption length of 239 nm.

Previous research on CdSe for thin-film solar-cell applications primarily focused on non-epitaxial growth methods, including closed-space sublimation, thermal evaporation, and electrodeposition.[66-68] Invariably, these methods resulted in polycrystalline CdSe material with short carrier lifetimes, low mobility, and low open-circuit voltage (V_{OC}). Furthermore, achieving p-type doping in polycrystalline CdSe proved to be challenging. In one study by Plant PV[67], CdSe thin films were grown on sapphire wafers, while ZnTe was grown on Si wafers using closed-space sublimation, and successful p-type doping ($\geq10^{16}$ cm^{-3}) with arsenic was achieved. Bagheri[66] explored CdSe thin films grown via thermal evaporation. Modest enhancements in CdSe grain size were obtained through $CdCl_2$ and Se flux treatment, along with thermal annealing. This led to the demonstration of PN

junction solar cells with V_{OC} = 0.8 V and short-circuit current density J_{SC} = 8 mA/cm^2. Shaikh *et al.*[68] investigated electrodeposition to fabricate n-CdSe/p-Cu_2Se heterojunction solar cells. However, the photovoltaic performance was limited, resulting in poor V_{OC} = 0.35 V and J_{SC} = 0.4 mA/cm^2. Due to the poor quality of the material, the successful development of a practical solar cell device based on monocrystalline CdSe has remained elusive.

The ZB InAs(111) crystal plane with an in-plane lattice constant of 4.28 Å is highly suitable as a substrate for the epitaxial growth of monocrystalline wurtzite CdSe, which has a lattice constant a = 4.30 Å, making InAs an attractive choice due to its small lattice mismatch of -0.35% with the WZ phase.[69]

1.6 Organization of the Dissertation

The first part of this dissertation reports on the quantum structures designed with type-II band alignment for applications in infrared photodetection and optical nonlinearity. The operation principle and analytical simulation of quantum efficiency cross-talk, along with the detailed MBE growth, material characterization and device fabrication of optically-addressed multiband photodetectors are discussed in the first half of chapter 2. The comprehensive derivations of second-order susceptibility in type-II quantum-well structures, the use of asymmetric quantum wells with type-II band alignment to increase $\chi^{(2)}$, the theoretical framework for envelope wavefunction engineering of type-II asymmetric quantum well designs, and comparison of the type-II structures with type-II structures to quantify the enhancement in $\chi^{(2)}$ resulted from the differing band alignments are discussed in the second half of chapter 2, where the theoretical derivation of $\chi^{(2)}$ is carried out by Dr. Stephen T. Schaefer. Chapter 3 presents the epitaxial growth, structural and optical properties of CdSe thin films grown on lattice-matched InAs(100) and (111)B-oriented substrates and the mixing of the two phases, WZ or ZB. The TEM and FFT experimental results are carried out by Professor Martha R. McCarthey and Professor David. J Smiths at ASU, and DFT results are acquired and calculated by Professor Andrew V.G. Chizmeshya. Finally, the conclusion and outlook of the present work are included in chapter 4.

CHAPTER 2

TYPE-II BAND ALIGNMENT QUANTUM STRUCTURES FOR INFARED PHOTODETECTION AND OPTICAL NONLINEARITY APPLICATIONS

2.1 Basics of Molecular Beam Epitaxy

Molecular beam epitaxy (MBE) facilitates the deposition of thin films with exceptionally high crystalline quality, primarily due to its utilization of an ultra-high vacuum (UHV) chamber with pressures that are maintained below 10^{-9} torr. Achieving UHV involves the removal of gases and particles from the chamber. FIG. 10 depicts[4] a schematic diagram of an MBE chamber. Inside the chamber, source materials are carefully loaded into individual pyrolytic boron nitride (PBN) or graphite crucibles which are located within the installed effusion cells.

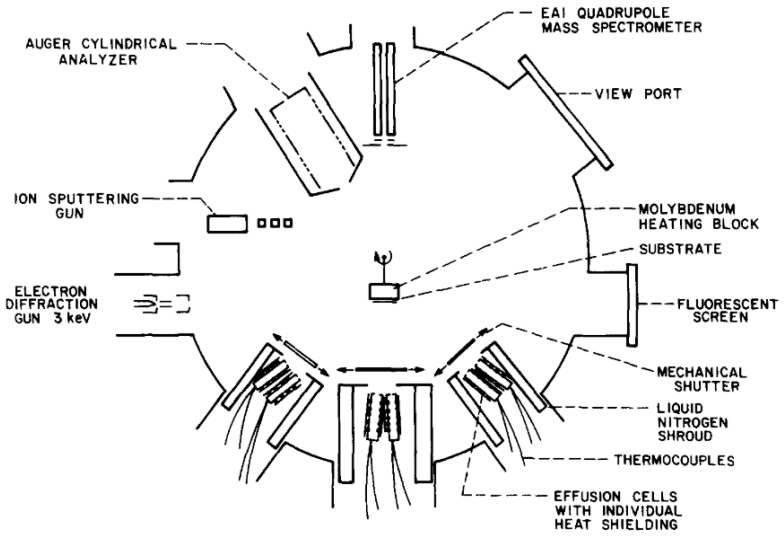

FIG. 10. Schematic cross-section view of a MBE chamber[4]

At low background pressures, molecules exhibit an extremely long mean free path, signifying that they can traverse extensive distances in a linear direction without

encountering collisions or interactions with other particles. The mean free path is defined as following:

$$\lambda = \frac{RT}{\sqrt{2}\pi d^2 N_A P}, \tag{13}$$

where R is the gas constant, T is the temperature, d is the diameter of the particle, N_A is Avogadro's number, and P is the pressure. According to the equation (13), in a standard MBE chamber operating at pressures around at 10^{-10} torr, the mean free path for a molecule in the chamber varies from 1 km to 10^5 km, depending on the diameter of molecule. This suggests that the molecular beam of source material, vaporized through heating within the effusion cell, can directly traverse from the crucible to the substrate and subsequently adhere to the substrate's surface, contributing to the growth process. Furthermore, to mitigate the presence of impurities and undesirable particles in both the source material and the chamber, it is strongly recommended to employ source materials with a purity level of 5N (99.999%) or even higher.

FIG. 11 provides a schematic diagram of the dual-chamber MBE system located within the ASU MBE Optoelectronics Group. The III-V chamber comprises effusion cells for aluminum (Al), gallium (Ga), and indium (In), as well as valved cells for phosphorus (P), arsenic (As), and antimony (Sb). Specifically, the cells for P, As, and Sb are equipped with cracking zones designed to generate group-V monomers and dimers. The tri-dopant cell, which incorporates silicon (Si), tellurium (Te), and beryllium (Be) dopants, alongside the recently integrated gallium telluride (GaTe) dopant cell, endows the system with the extra doping capability. Notably, this setup facilitates seamless transitions between n- and p-dopants without the need for growth interruption. The II-VI chamber comprises effusion

cells for Be, magnesium (Mg), cadmium (Cd), and zinc (Zn), in addition to valved cells for selenium (Se) and Te. These two chambers are connected via a preparation chamber, which enables the transfer of under UHV conditions. The temperature of the substrate heater is both measured and controlled through the utilization of a thermocouple, situated on the rear side of the substrate holder, in conjunction with a closed-loop Eurotherm controller. Meanwhile, the temperature of the sample surface is continuously monitored using a pyrometer. The temperature of each cell is also measured and controlled by thermocouple and Eurotherm. Additionally, shutters positioned in front of all cells switch on or off the beam flux with precise time control. The intensity of the flux (in unit of nA) is measured through a beam flux monitoring (BFM) ion gauge. Throughout the growth process, the substrate holder maintains continuous rotation to mitigate any nonuniformities. In-situ reflective high energy electron diffraction (RHEED) is used to monitor the sample surface by confirming surface reconstruction during the growth.

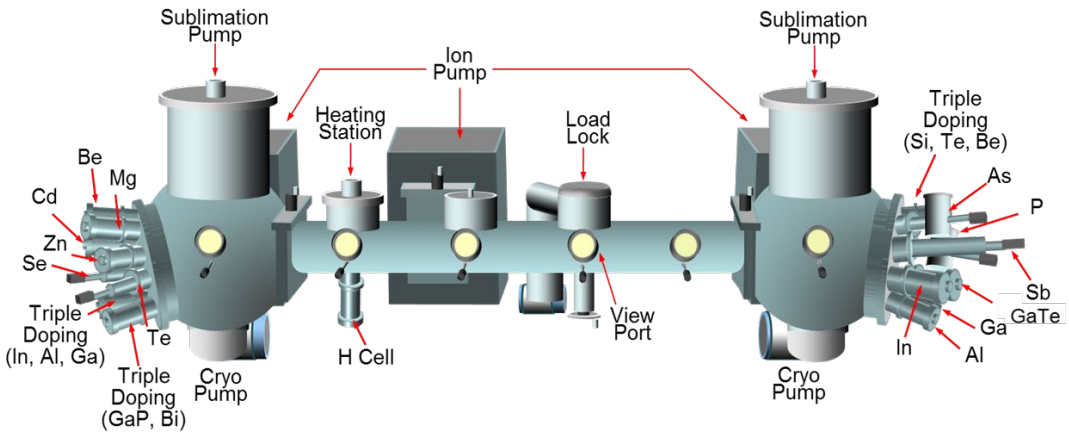

FIG. 11. Schematic drawing of dual-chamber MBE system. The III-V and II-VI chambers are connected by a preparation chamber, allowing samples to be transferred under an ultra-high vacuum.

All of the samples demonstrated in this dissertation were fabricated using this dual-chamber MBE system at ASU. In the case of the II-VI samples covered in Chapter 4, the process involved the removal of oxide layers from the InAs substrate and the initial growth of an InAs buffer are completed within the III-V chamber. Subsequently, these samples were transferred into the II-VI chamber to finalize the growth of II-VI materials.

2.2 Operation Principle of Optically-Addressed Mutiband Photodetectors

Multiband or multiband discrete photodetectors and focal plane arrays (FPAs) have been developed for a wide range of commercial and defense applications. These applications include environmental resource surveying, chemical detection, target identification, and have even been proposed for use in eye-safe imaging systems for autonomous vehicles. [70-73] Two typical architectures of dual-band detectors are: i) three-terminal structures consisting of two photodiodes,[74] and ii) two-terminal structures consisting of two back-to-back photodiodes with a polarity-switchable electrical bias [74,75]. These two architectures cannot be extended to more than two bands unless three or more terminals are used [76-78]. This requires additional terminals for each pixel, greatly complicating the FPA layout and device processing, decreasing the fill factor, and increasing the ROIC complexity. Reducing the number of terminals from three to two is therefore highly desirable and allows the multiband detector to be integrated with off-the-shelf single-band ROICs.[77] A novel approach has been demonstrated in 2010: monolithically-integrated optically-addressed three-band two-terminal photodetectors to cover the visible and near IR range.[79,80] Several dual-band photodetectors based on this novel approach using PIN diodes, nBn, and QWIP structures have also been successfully demonstrated to cover the MWIR and LWIR bands [80,81].

The operating principle of this novel optical addressing design is to use different optical biases to a stack of photodiodes (PDs) with two-terminals to select the target band for multiband detection (Fig. 12 Left). Under external electrical bias, the total dark current going through such a PD stack is dictated by the PD with the smallest saturation current. When a set of LEDs with different wavelengths corresponding to each individual PD are

used to optically bias or address all the photodiodes except the detecting PD, the detecting PD will be the current-limiting device and the entire stack then operates as one single-band detector with a spectral response determined by the detecting PD.

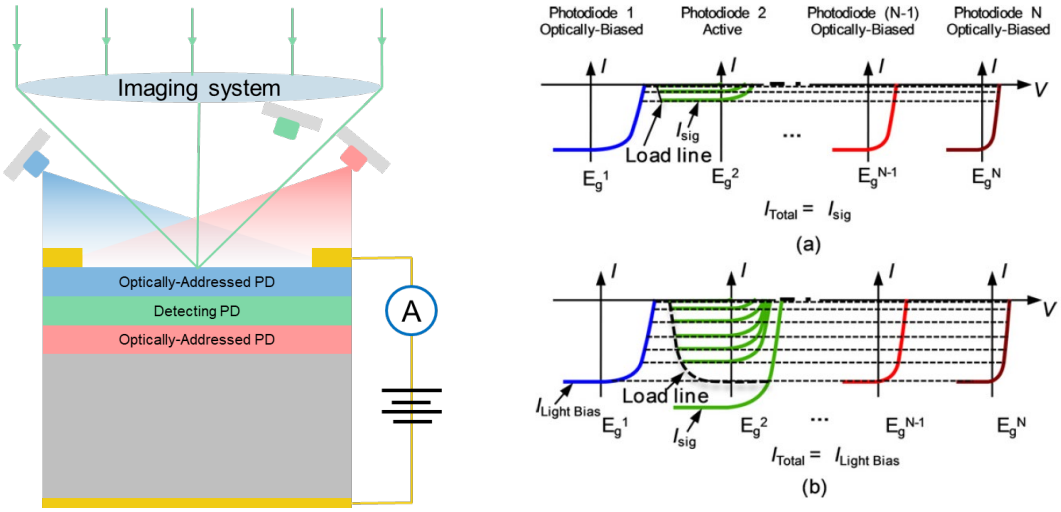

FIG. 12. Left : Schematic of the optically-addressed, two-terminal, multiband photodetector, a InGaP/InGaAs/Ge triple-junction solar cell. Right: Schematic illustration of the ideal I–V curves of the individual photodiodes and the load line for the active detector for two input signal intensities: (a) the signal intensity is less than the optical bias flux and (b) the signal intensity is greater than the optical bias flux. The optical bias photon flux is equal for all inactive photodiodes[79].

Fig. 12 Right shows the ideal I–V curves of the individual photodiodes and the load line for the active detector for two input signal intensities resulting in: (a) the photogenerated current from the signal being less than the photogenerated current due to the optical bias and (b) the photogenerated current from the signal being greater than the photogenerated current due to the optical bias. The optical bias condition is such that the photon flux is equal for all the inactive photodiodes. The optically-biased diodes operate in the photovoltaic mode with their forward voltages determined by the operating current of the entire device[79], which in this case is due to the signal, I_{sig}. The optical bias results in a reverse voltage bias on the active photodiode, causing it to operate in the

photoconductive mode, as shown by the intersection of the active photodiode's I–V curve and the load line in Fig. 11. When the input signal is not w8ithin the active photodiode's spectral response range, the total device current is very small (the dark current of the active photodiode). Thus, the device is a single-band detector with the spectral response of the active photodiode only. As long as the photogenerated current due to the signal is smaller than the photogenerated currents from the optically-biased photodiodes, this single-band detection condition is maintained. But when the current generated from the input signal becomes greater than the current due to the light bias, the operating points of the individual photodiodes change. The device current is no longer due to the signal but to the optical bias, and the single-band operating principles just described are not applicable.

In principle, this multiband detector structure is suitable for any range of the spectrum from UV to infrared and for any number of bands. Practically, the bias LEDs can be mounted on the cold-shield sidewalls between the cold stop aperture and the FPA without affecting the field of view and the cold-stop efficiency. This configuration also allows the LEDs to operate at cryogenic temperatures, which increases their efficiency. Fiber optics or liquid light guides can also be used to bring the LED light to the FPA. A control algorithm can cycle through the various combinations of biasing LEDs to address the different bands and enable multiband detection. This sequential sampling method, also used for the current dual-band back-to-back diode FPA, leads to a tradeoff between frame rate, integration time, and the number of bands for the optically-addressed two-terminal multiband detectors. In comparison, the dual-band three-terminal detectors can sample each band simultaneously, but they suffer from a lower fill factor due to the extra contact. This requires a longer integration time to reach a desired signal-to-noise ratio, limiting the

maximum frame rate. Additionally, the extra contact increases device fabrication and packaging complexity. The integration of a multiband detector and the optical biasing scheme allows the number of detecting bands to increase without raising the number of contacts above two per pixel. FIG. 13 shows the device structure design of an optically-addressed monolithically-integrated tri-band photodetectors using GaSb and $InAs/InAs_xSb_{1-x}$ superlattice materials for SWIR/MWIR/LWIR detection ranges. The proposed configuration comprises three individual p-i-n photodiodes. Each photodiode features GaSb and T2SLs absorbers, which are individually enclosed within layers of AlGaAsSb that are lattice-matched to the GaSb substrate. The cutoff wavelengths for SWIR GaSb, MWIR T2SL and LWIR T2SL absorbers are 1.7 μm, 4.9 μm and 12.1 μm, respectively. The Sb composition (x) in $InAs_{1-x}Sb_x$ remains constant throughout the growths of T2SLs to ensure compositional consistency and enhance precision in controlling the ternary compound's composition.[82,83]

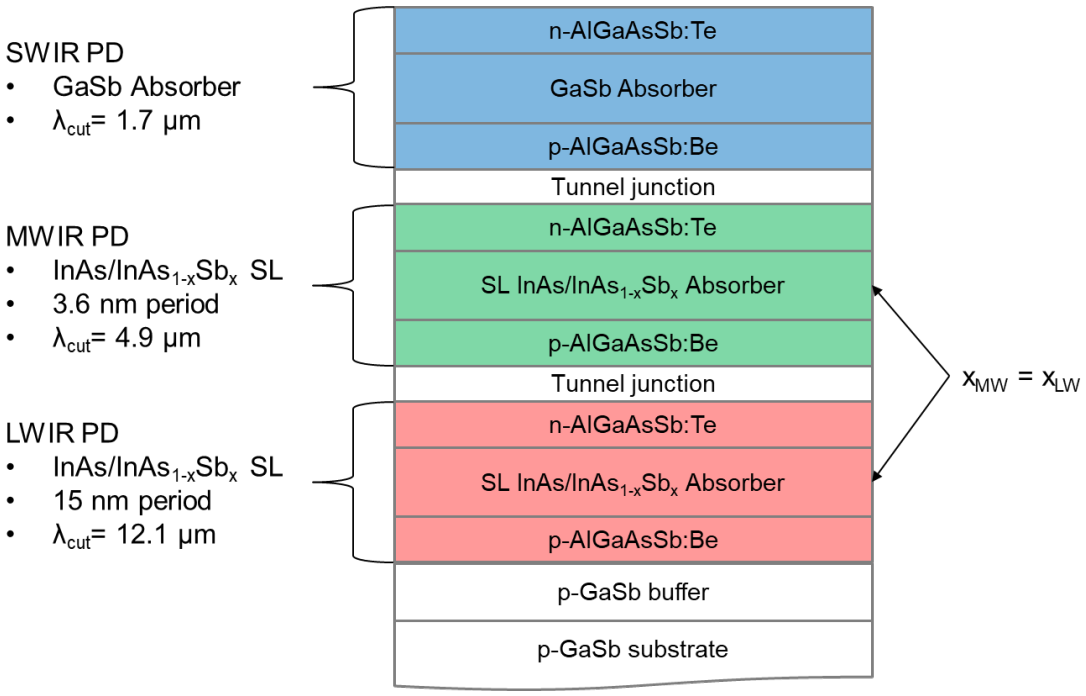

FIG. 13. Device structure of a device structure design of an optically-addressed monolithically-integrated tri-band photodetectors using GaSb and InAs/$InAs_xSb_{1-x}$ superlattice materials. [82,83]

2.3 An Analytical Model and Simulation of Crosstalk in Quantum Efficiency

FIG. 14 shows the responsivity of the previously studied three photodiodes, which clearly confirms that optical biasing can address one photodiode at a time in a multiband detector with only two electrical terminals.[79,81] When the InGaAs and Ge photodiodes are optically biased, the entire detector response is that of the InGaP photodiode only, with zero response above 650 nm. The InGaAs photodiode shows a response from 650 to 900 nm, while the Ge photodiode responds at greater than 900 nm. The crosstalk between the InGaP and InGaAs photodiodes and between the InGaAs and Ge photodiodes is a result of (i) luminescence coupling, (ii) photon flux leakage through the InGaP and InGaAs photodiodes, as they may not be optically thick enough. In both cases, the crosstalk responsivity is less than ten percent of the responsivity in the photodiode's intended response range, and this can be further reduced by optimizing the absorber thickness designs.

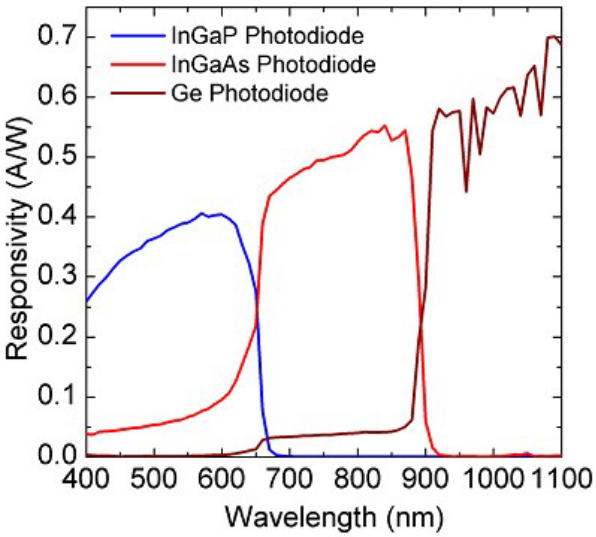

FIG. 14. Measured spectral responsivity demonstrates detection band switching. The responsivity was measured with matching photon flux on the inactive photodiodes.[79,81]

An analytical model has been developed for the simulation of luminescence coupling and light leakage effects in optically-addressed tri-band photodetectors. GaSb, MWIR InAs/InAsSb T2SL and LWIR InAs/InAsSb T2SL have been selected for the absorber materials for SWIR, MWIR and LWIR, respectively. The experimental values of absorption coefficients and external quantum efficiency of corresponding materials can be found in literature. [36,84-88] The formulas of external quantum efficiency corresponding to SWIR detection mode on, MWIR detection mode on and LWIR detection mode on are listed as Eq. 14 (a), (b) and (c) below: [82,83]

(a) SWIR Active, MWIR+LWIR LEDs on

$$\mathrm{EQE}(\lambda) = \eta_{\mathrm{QE1}}(\lambda)\left(1 - e^{-\alpha_1(\lambda)d_1}\right) \tag{14a}$$

(b) MWIR Active, SWIR+LWIR LEDs on

$$\begin{aligned}\mathrm{EQE}(\lambda) = {} & \eta_{\mathrm{PL1}}(\lambda)\eta_{\mathrm{QE2}}(\lambda_{\mathrm{PL1}})\left(1 - e^{-\alpha_1(\lambda)d_1}\right)\left(1 - e^{-\alpha_2(\lambda_{\mathrm{PL1}})d_2}\right) \\ & + \eta_{\mathrm{QE2}}(\lambda)e^{-\alpha_1(\lambda)d_1}\left(1 - e^{-\alpha_2(\lambda)d_2}\right)\end{aligned} \tag{14b}$$

(c) LWIR Active, SWIR+MWIR LEDs on

$$\begin{aligned}\mathrm{EQE}(\lambda) = {} & \eta_{\mathrm{PL1}}(\lambda)\eta_{\mathrm{PL2}}(\lambda_{\mathrm{PL1}})\eta_{\mathrm{QE3}}(\lambda_{\mathrm{PL2}})\left(1 - e^{-\alpha_1(\lambda)d_1}\right)\left(1 - \right. \\ & \left. e^{-\alpha_2(\lambda_{\mathrm{PL1}})d_2}\right)\left(1 - e^{-\alpha_3(\lambda_{\mathrm{PL2}})d_3}\right) + \eta_{\mathrm{PL2}}(\lambda)\eta_{\mathrm{QE3}}(\lambda_{\mathrm{PL2}})e^{-\alpha_1(\lambda)d_1}(1 - \\ & e^{-\alpha_2(\lambda)d_2})(1 - e^{-\alpha_3(\lambda_{\mathrm{PL2}})d_3}) + \eta_{\mathrm{QE3}}(\lambda)e^{-\alpha_1(\lambda)d_1}e^{-\alpha_2(\lambda)d_2}(1 - e^{-\alpha_3(\lambda)d_3})\end{aligned} \tag{14c}$$

λ is the wavelength of input signal, η_{QE1}, η_{QE2} and η_{QE3} are the external quantum efficiencies, α_1, α_2 and α_3 are the absorption coefficients, and d_1, d_2 and d_3 are the layer thicknesses of GaSb, MWIR T2SL and LWIR T2SL, respectively. Besides these values, photoluminescence quantum efficiencies η_{PL} are also defined and are strongly dependent on the materials and the reversed bias voltage applied to the detectors. With an increased reverse bias voltage, a lower photoluminescence quantum efficiency η_{PL} yield, as it promotes the more effective separation of carriers (electrons and holes) rather than their recombination..

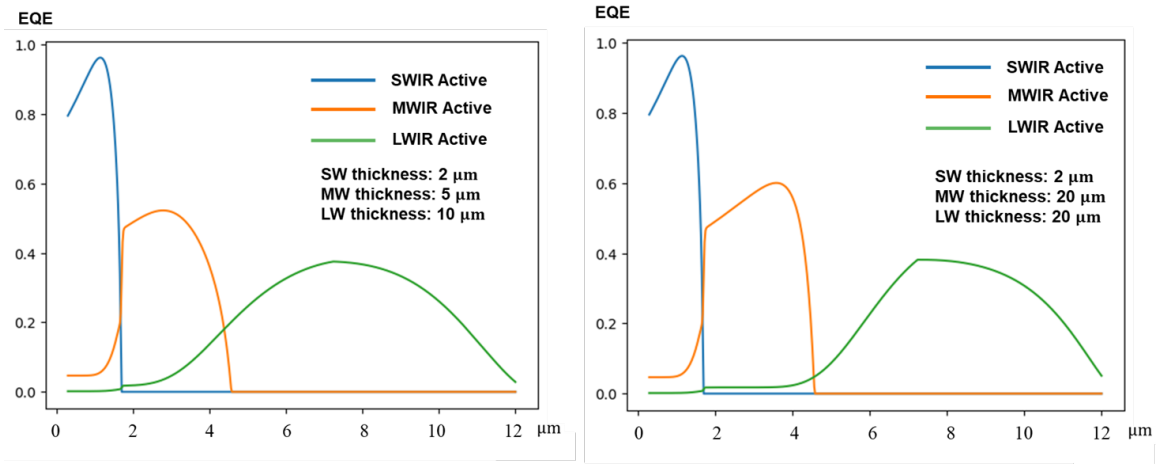

FIG. 15. Expected device EQE modeling with bias light illumination with different layer thicknesses for the absorbers. [82,83]

As illustrated in FIG. 15, the blue, orange, and green curves correspond to the anticipated EQE of the active SWIR mode with MWIR and LWIR LEDs activated, the active MWIR mode with SWIR and LWIR bias LEDs activated, and the active LWIR mode with SWIR and MWIR bias LEDs activated, respectively. The simulation process is simplified by the parametrization of the material's absorption coefficient and EQE based on reported experimental results. The plots reveal that crosstalk arises from the incomplete

absorption of optical bias and signals. Additionally, luminescence coupling introduces artifacts and background noise in the EQE plot[79,81]. Increasing absorber thickness and reducing luminescence efficiency reduces the crosstalk. As shown in FIG.14, increases in both thickness of the SWIR and MWIR absorbers from 5μm to 20μm and from 10μm to 20μm respectively, reduce the crosstalk significantly.

2.4 Molecular Beam Epitaxy of InAs/$InAs_{1-x}Sb_x$ Type-II Superlattices

InAs possesses a slightly smaller lattice constant in comparison to GaSb. Conversely, $InAs_{1-x}Sb_x$ with x > 0.09 exhibits a larger lattice constant than GaSb. Consequently, when these two materials are grown on a GaSb substrate, InAs experiences tensile strain, whereas InAs/$InAs_{1-x}Sb_x$ is subjected to compressive strain. When either InAs or $InAs_{1-x}Sb_x$ is grown on a GaSb substrate, the presence of strain occurs. If the layer thickness becomes excessively large, the layer will eventually relax, leading to the formation of a significant number of misfit dislocations. These dislocations can ultimately compromise the crystalline quality of the epitaxial thin film. Matthews and Blakeslee developed a method to calculate the critical thickness of the interface structure in multilayers. This critical thickness represents the point at which a layer can be grown in a fully-strained state. Their calculation is based on considering two key forces[89]: 1. The force resulting from the misfit strain between the layer and the substrate. 2. The tension in the dislocation line. By evaluating these forces, their work provides valuable insights into understanding when and how thin films can be grown while maintaining a fully-strained condition, which is crucial for optimizing the quality of epitaxial thin films. The expression of the critical thickness for a ZB (100) structure is shown as Eq. 15[90]:

$$h_c = \frac{a_S\left(1-\frac{\nu}{4}\right)\left[\ln\left(\frac{\sqrt{2}h_c}{a_S}\right)+1\right]}{\sqrt{2}\pi|\varepsilon|(1+\nu)} \tag{15a}$$

$$\nu = \frac{C_{12}}{C_{11}+C_{12}} \tag{15b}$$

$$\varepsilon = \frac{a_S - a_L}{a_L}, \tag{15c}$$

In this equation h_c represents the critical thickness, a_S is the lattice constant of the substrate, a_L is the lattice constant of the epilayer, ν is the Poisson's ratio, C_{11} and C_{12} are the elastic constants of the epilayer, and ε is the strain of the epilayer. The critical thickness limits the maximum thickness which can be grown on a substrate without generating misfit dislocations. When two or more layers with different types of strain, either compressive or tensile, are grown alternately on a substrate, it becomes feasible to achieve a balance in the overall in-plane strain.[90] When there is an absence of in-plane shear force to induce misfit dislocations, the in-plane stress is maintained at zero. This implies that the alternative multi-layers can theoretically be grown to an infinite thickness on the substrate without the need to consider the accumulation of in-plane stress-related issues. This provides an approach of the strain-balancing strategy that one can achieve an average in-plane stress of zero within the alternating combination of tensile and compressively strained layers.[88] There are three methods for realizing strain-balance condition, including average lattice method, thickness weighted method, and zero-stress method, proposed by Ekins-Daukes *et al.*.[90] The expressions of these three methods are shown as Eq. 16, Eq. 17 and Eq. 18, respectively[90]:

$$a_S = \frac{t_1 a_1 + t_2 a_2}{t_1 + t_2} \tag{16}$$

$$a_S = \frac{(A_1 t_1 + A_2 t_2) a_1 a_2}{A_1 t_1 a_2 + A_2 t_2 a_1}, \tag{17}$$

where $A = C_{11} + C_{12} - 2C_{12}^2/C_{11}$.

$$a_S = \frac{A_1 t_1 a_1 a_2^2 + A_2 t_2 a_2 a_1^2}{A_1 t_1 a_2^2 + A_2 t_2 a_1^2}. \tag{18}$$

In the average lattice method, the approach essentially involves calculating the average lattice constant of the two layers to match that of the substrate. This method assumes that both layers possess identical elastic properties. The thickness-weighted method proposes that the strain-balance condition is achieved when the product of strain and thickness is equal for both layers. The approach of the zero-stress method calculates the strain-balance condition from classical elasticity theory and considers the lowest energy state of the tensile or compressively strained layers, where no average stress is present. In this dissertation, the thickness-weighted method is adopted for the calculation of the strain-balance condition for all the T2SLs reported.

$InAs/InAs_{1-x}Sb_x$ superlattice samples with strain-balanced design were grown by MBE at temperature of 410℃ after the GaSb buffer layer growth at temperature of 500℃ on GaSb(100) substrates. The layer structure of the calibration samples consisted of a 1 μm superlattice of alternating InAs and $InAs_{1-x}Sb_x$ layers sandwiched between two 10-nm-thick AlSb barrier layers which provided better carrier confinement and reduced surface recombination. A 20-nm-thick GaSb cap layer was grown on top of AlSb barrier to prevent the rapid oxidation of Al when exposed to the atmosphere. An advantage of growing $InAs/InAs_{1-x}Sb_x$ Type-II T2SLs is the simplicity with which alternating abrupt layers can be achieved by maintaining fixed As flux and modulating one Sb shutter without any intermixing at the interfaces. The schematic cross-section of the superlattice calibration sample is shown in FIG. 16[19]. The growth rate of InAs was kept at 15 nm/min with an As/In flux ratio of 3 while the Sb/In flux ratio ranged from 1.5 to 2 for Sb compositions in $InAs_{1-x}Sb_x$ alloy, x ranging from 0.3 to 0.6 for various samples. The layer thickness of InAs

and $InAs_{1-x}Sb_x$ is calculated based on the thickness-weighted method of strain-balance condition as described in Eq.17.

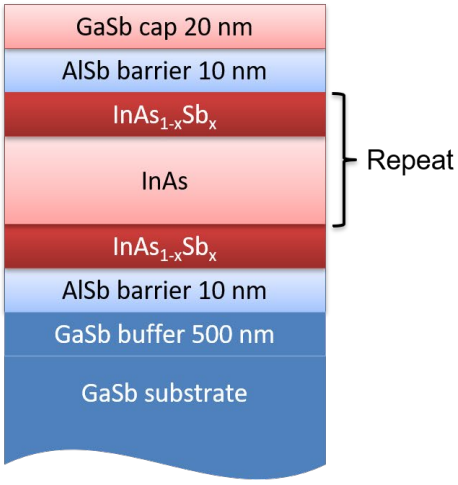

FIG. 16. The cross-section of InAs/$InAs_{1-x}Sb_x$ T2SL samples with AlSb barrier layers and a 20-nm-thick GaSb capping layer[19].

The cross-section structure of a dual-band structure covering SWIR and MWIR grown by MBE is shown in FIG. 17. The sample structure comprises a 5-μm-thick mid-wavelength superlattice (MWSL) region and a separate 2-μm-thick GaSb SWIR region. These regions are individually sandwiched between $Al_{0.5}Ga_{0.5}As_{0.04}Sb_{0.96}$ barrier layers and are grown on top of a 500-nm-thick GaSb buffer layer. The MWSLs region comprises unintentionally doped n-type 4.3 nm/1 nm InAs/$InAs_{0.68}Sb_{0.32}$ T2SLs. The As/In flux ratio was kept constant at 3 during the growth while the Sb/In ratio were 1.5 for the growth of MWSL and GaSb, and the growth rates of InAs and GaSb were fixed at 15 nm/min at a growth temperature of 410 °C. GaTe and Be cells were used for n-type doping and p-type doping, respectively. The entire structure was grown at the temperature of 410 °C, which is noteworthy as it marked the first attempt to grow GaSb at a relatively lower temperature, as opposed to the conventional 500 °C. [19,26]

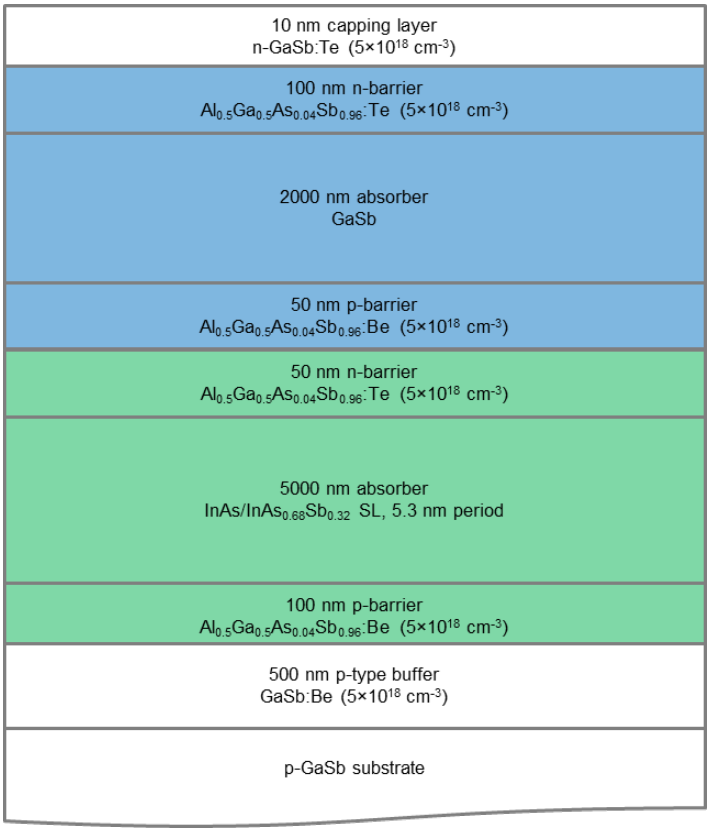

FIG. 17. The cross-section structure of a dual-band structure covering SWIR and MWIR grown by MBE, consisting of a 5-μm-thick MWSL region and a 2-μm-thick GaSb SWIR region. [82,83]

2.5 Characterization of $InAs/InAs_{1-x}Sb_x$ Type-II Superlattices

The structural properties of the T2SL samples were characterized by using PANalytical X'Pert Pro MRD High Resolution X-ray Diffraction (HR XRD) with ω-2θ scans along the (004) plane. FIG. 16 shows an ω-2θ XRD of (004)-plane of the dual-band structure, and the black and red lines illustrate the measured and simulated curves, respectively. The results are analyzed with X'Pert Epitaxy software. The intense satellite peaks with narrow linewidth and the Pendellösung fringes indicate high degree of crystalline quality, abrupt interface, and uniform superlattice period. Moreover, the zeroth-order peak of the MWSL is well-aligned with the GaSb substrate peak. This alignment suggests that the T2SL is strain-balanced to GaSb, which is a crucial requirement for growing thick layers without the generation of misfit dislocations. The average superlattice period thickness can be obtained by the spacings between multiple adjacent satellite peaks. The period thickness, as well as the thickness of InAs and $InAs/InAs_{1-x}Sb_x$ layers, are not precisely known parameters. They are typically estimated based on the growth rates of InAs and $InAs/InAs_{1-x}Sb_x$ and the duration of shutter opening during the growth. Nevertheless, precise values for the thicknesses of InAs and $InAs/InAs_{1-x}Sb_x$ layers are determined after the average period thickness is confirmed while also factoring in the growth rate and the duration of the Sb shutter opening. After all, the only parameter that requires fitting in the simulation software is the Sb composition. The extracted parameters, shown in Table 2, are that of 4-nm-thick InAs and 1.3-nm-thick $InAs_{1-x}Sb_x$ where x=0.325. Here, an abrupt interface and zero unintentional Sb inter-diffusion into the InAs layers are assumed. The simulation curve plotted in FIG.18 matches the measurement curve, and the

$Ga_{0.5}Al_{0.5}As_{0.10}Sb_{0.90}$ barrier peak is shown and matched, suggesting the accuracy of the fitted thickness and composition.

Layer	Measurement (XRD)			Design		
	InAs (nm)	$InAs_{1-x}Sb_x$ (nm)	x	InAs (nm)	$InAs_{1-x}Sb_x$ (nm)	x
MWSL	4	1.3	0.32	4	1.3	0.325

Table 2. The extracted parameters from the best fit of (004) XRD, indicating the consistency between the design and measurement[82,83].

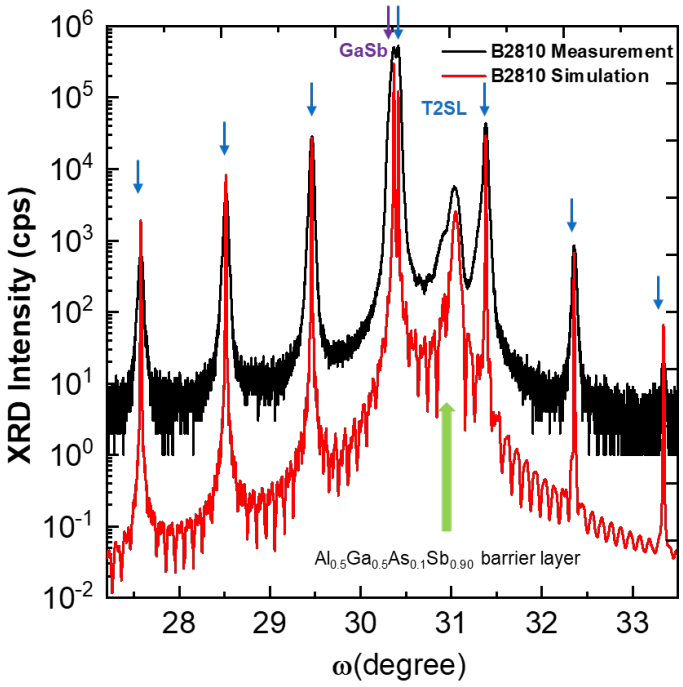

FIG. 18. $\omega - 2\theta$ XRD of the dual-band structure. Black and red lines illustrate the measured and simulated curves, respectively. The peaks for GaSb, MWSLs and $Ga_{0.5}Al_{0.5}As_{0.10}Sb_{0.90}$ barrier are as indicated by different arrows[82,83].

The optical properties of the T2SLs were characterized by the steady-state photoluminescence (SSPL) measurements conducted at 12 K and 77K. A 785 nm laser diode with 6 W/cm² pumping density was modulated at 50 kHz to excite the samples. The

measurements were carried out using a double-modulation ThermoFisher iS50R Fourier transform infrared (FTIR) spectrometer equipped with liquid-nitrogen-cooled InSb and HgCdTe detectors. To achieve a temperature of 12 K, the samples were placed within a closed-cycle cryogenic system. FIG. 19 provides an overview of the schematic FTIR system. The effective transition energy at low temperatures was determined by the peak position of photoluminescence (PL) in units of meV or micrometers. The normalized PL spectra of the T2SL calibration samples are depicted in FIG. 20 as a function of wavelength. It's worth noting that this measurement was conducted in the atmosphere, which introduced a discontinuity in the PL spectra around 290 meV due to CO_2 absorption. However, this discontinuity can be eliminated by normalizing the data using the calibration curve of the detector. The photoluminescence measurements show that the cutoff wavelengths of InAs/InAsSb T2SL calibration samples ranging from 3.8 to 12 μm, and that T2SLs have the capability for bandgap engineering, as reflected in the manipulation of the bandgap (PL peak energy $-\frac{1}{2}k_BT$) through adjustments in layer thickness and Sb composition. All T2SL calibration samples demonstrate strong PL intensity and high signal-to noise ratio, besides sample B2755 whose PL peak is at 6.3 μm. The low PL intensity and high noise may be attributed to the strong H_2O absorption in the atmosphere.

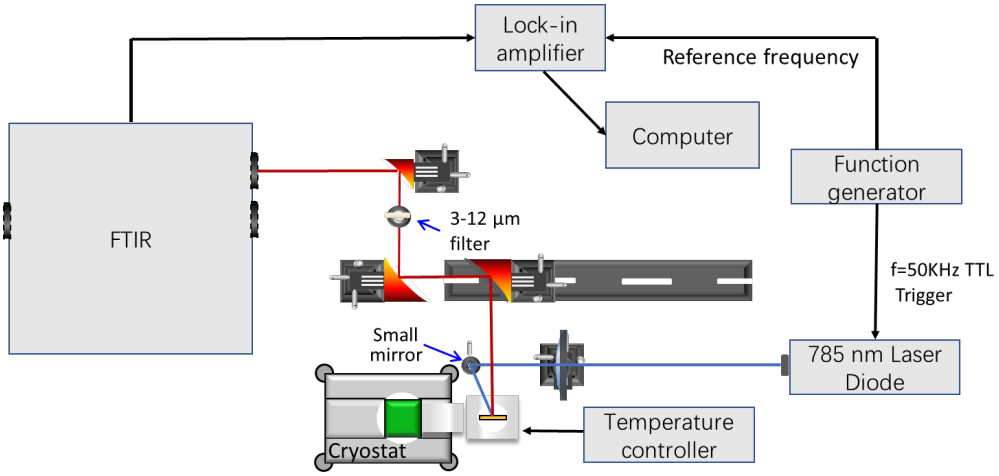

FIG. 19. A schematic diagram of ThermoFisher iS50R Fourier transform infrared (FTIR) spectrometer. This system can be used for steady-state photoluminescence with wavelength range from 1.5 to 12µm and time-resolved photoluminescence with resolution 50ns.

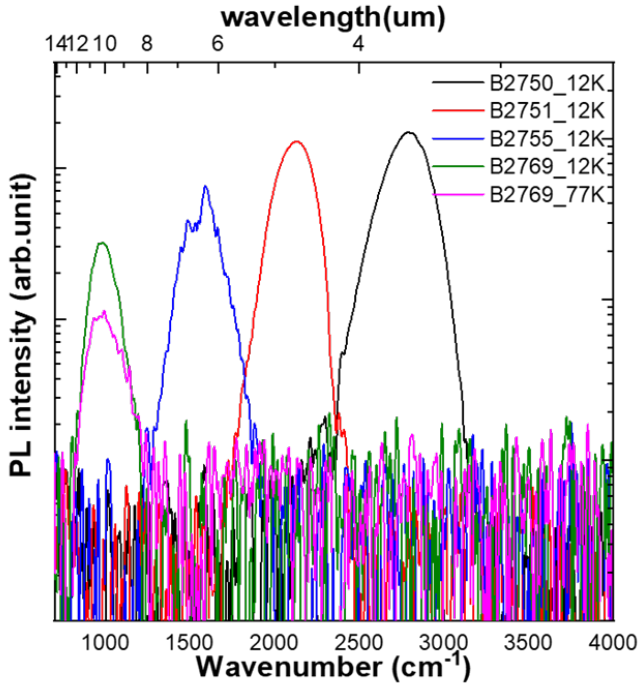

FIG. 20. Normalized 12 K PL spectra from InAs/$InAs_{1-x}Sb_x$ T2SLs calibration samples. The discontinuity at 290 meV is the result of CO2 absorption.

Additionally, Secondary Ion Mass Spectrometry (SIMS) has been applied to the dopant calibration samples which ensured the dopant levels in designed p- and n-barrier layers. SIMS detects very low concentrations of dopants and impurities. The technique provides elemental depth profiles over a wide depth range from a few angstroms (Å) to tens of micrometers (μm). Shown in Fig 21, Te and Be doping levels can reach 10^{21} and 10^{19} atom/cm^{-3} in GaSb respectively, and the T2SL layers can be either p-doped or n-doped up to the level of 10^{19} atom/cm^{-3}. The oscillation of Te dopants in T2SL is caused by the alternating changes in group-V fluxes.

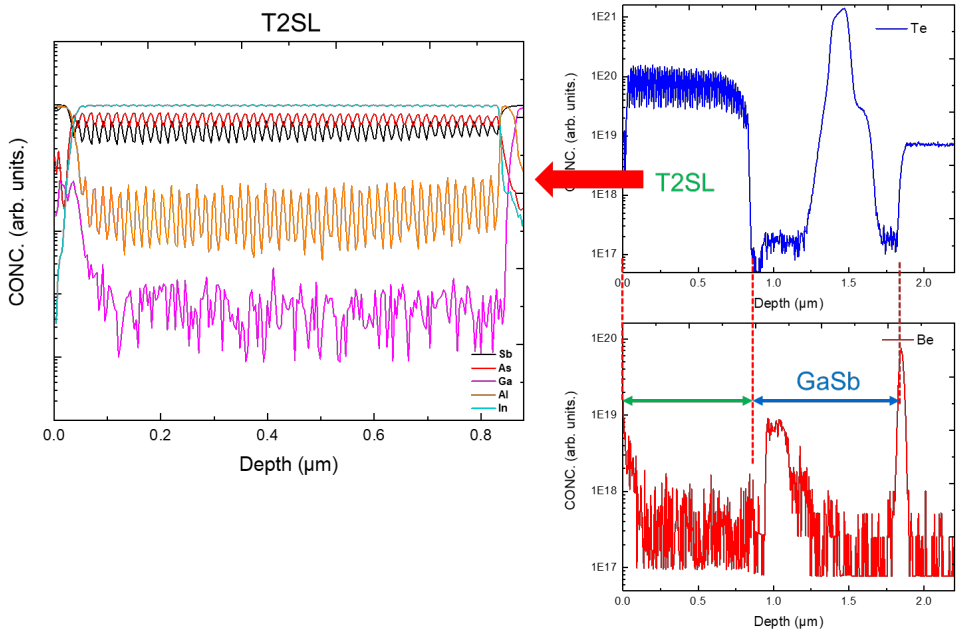

FIG. 21. SIMS measurement of the InAs/InAs$_{1-x}$Sb$_x$ T2SL and GaSb calibration sample[82,83]

The time-resolved photoluminescence measurement (TRPL) can be done by the "Design II" schematically illustrated in FIG. 22. The system is based around a Vigo System 3.0 – 6.9 μm HgCdTe four-stage thermoelectrically cooled photodetector interfacing

directly with an Acqiris U5310A PCIe high-speed ADC card with sampling rate of 5 GHz. The sample is excited by a Bright Solutions Wedge XF 1064 nm pulsed laser with a typical pulse width of 490 ps and 10 kHz repetition rate. This system enables direct analog-to-digital conversion of the time-varying photoluminescence signal with resolution of 200 ps. A PC running the Acqiris MD3 SFP software interfaces with the ADC card, providing real-time voltage vs time traces for TRPL experiments. The MWIR time-resolved photoluminescence system's performance is characterized by its impulse response. The procedure is illustrated graphically in Fig. 23 and consists of two separate measurements: (i) measurement of scattered 1064 nm laser radiation from the cryostat/cold finger surface, and (ii) measurement of baseline noise with the laser beam blocked. The scattered radiation from the pulsed laser acts as a $\delta(t)$ function permitting accurate measurement of the system's time-domain impulse response.

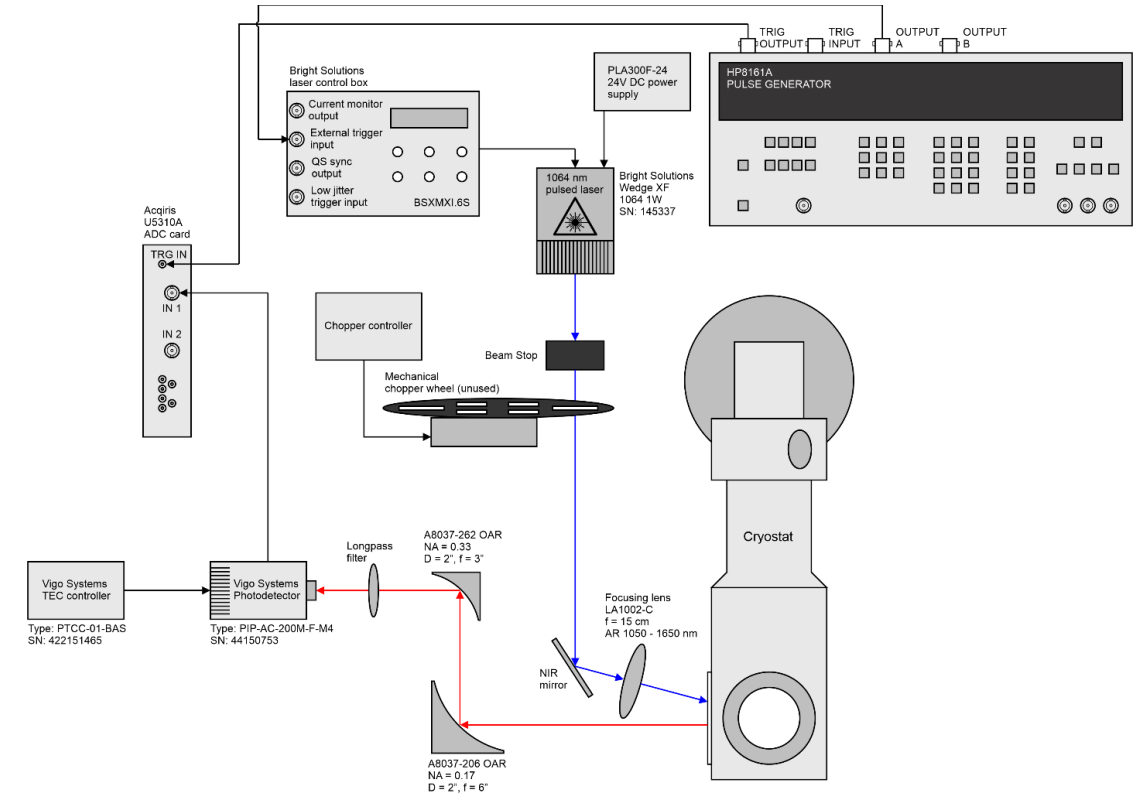

FIG. 22. MWIR TRPL system utilizing an integrated high-speed analog-to-digital conversion card and 3.0–6.9 μm HgCdTe four-stage TE cooled photodetector.

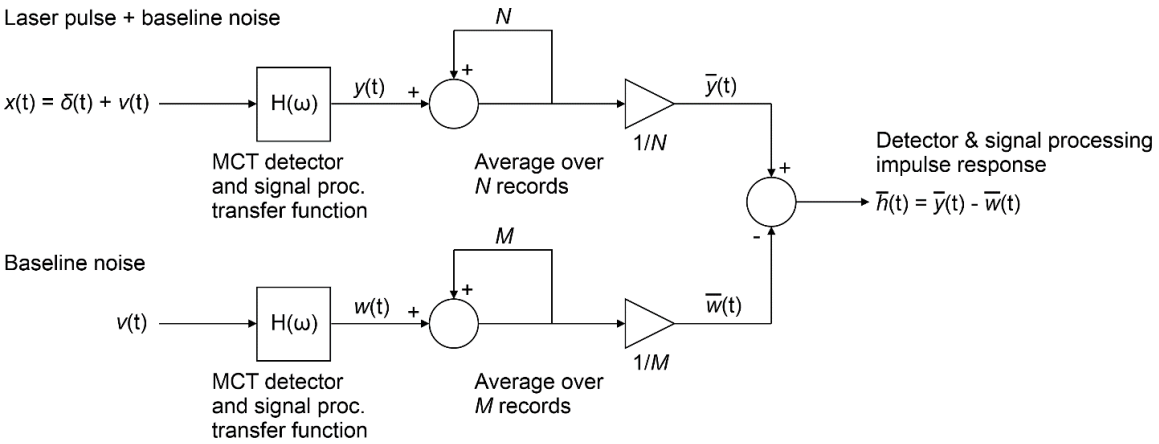

FIG. 23. Schematic of MWIR TRPL system impulse response measurement. Two sets of measurements are collected: (i) using scattered pulsed laser radiation to excite the detector as a $\delta(t)$ function (top) and (ii) with the laser beam blocked to measure background noise only (bottom).

The MWIR TRPL system was validated by measuring a series of benchmark samples consisting of (i) 1 μm thick epitaxial InAs on InAs confined by 10 nm thick AlSb barriers, sample B2380, (ii) a InAs/InAsSb type-II superlattice grown on GaSb, IQE 2503037, and (iii) a 550 nm thick InAs/InAs0.76Sb0.24 type II superlattice grown on GaSb, B2589. The measured time-domain and frequency-domain PL signals are shown in Fig. 24 and Fig. 25, respectively. The strongly emitting InAs sample B2380 saturated the ADC card input, resulting in a flat-topped time trace with a corresponding anomalous high-frequency feature; this saturation does not affect the PL decay away from the ADC card input limit. The InAs sample B2380 and InAs/InAsSb T2SL sample IQE 2503037 exhibit multiple exponential PL decays, indicating the carrier lifetime is excitation density dependent. A single exponential PL decay is fitted to the regions indicated by solid lines and arrows, and the resulting PL decay lifetime is indicated directly on Fig. 13. The fitted PL decay times are 17.9 ns for InAs sample B2380, 291.2 ns for InAs/InAsSb T2SL sample IQE 2503037, and 13.0 ns for InAs/InAsSb T2SL sample B2589. The 291.2 ns lifetime for sample IQE 2503037 compares favorably to prior measurements of the sample using the double-modulated analog system with a liquid nitrogen cooled detector which indicated a lifetime of 418 ns. This experiment validates that the MWIR time-resolved photoluminescence system using direct analog-to-digital conversion can accurately measure lifetimes as short as 6 ns in the spectral range of 3.0 – 6.9 μm.

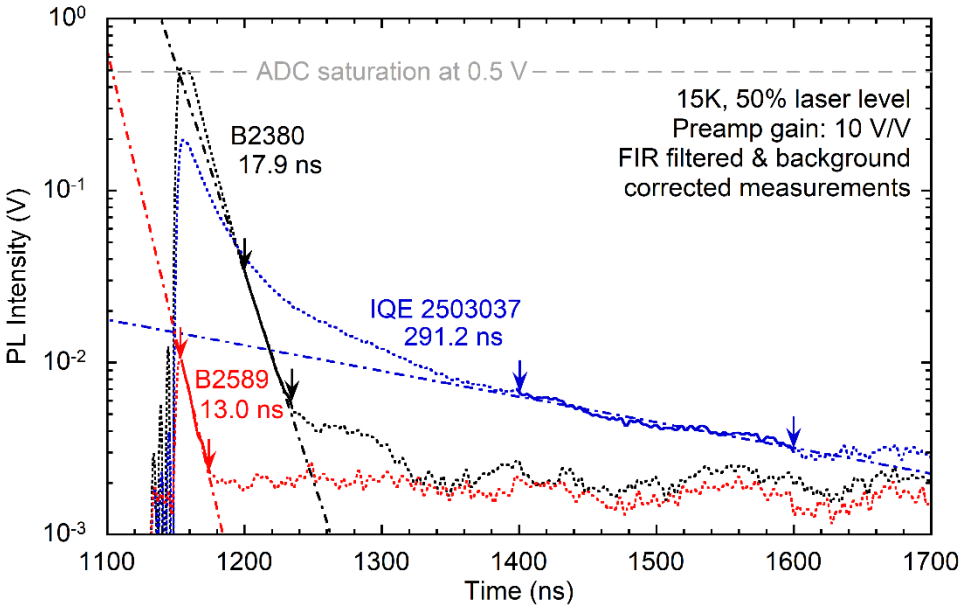

FIG. 24. PL signal voltage vs time for 1 μm thick InAs sample B2380 (black), InAs/InAsSb T2SL sample IQE 2503037 (blue), and InAs/InAsSb T2SL sample B2589 (red). Solid lines and arrows indicate fitting regions for single exponential PL decay model (dash-dotted lines); the dotted lines indicate regions that are not fitted. Single exponential PL decay lifetimes are shown directly.

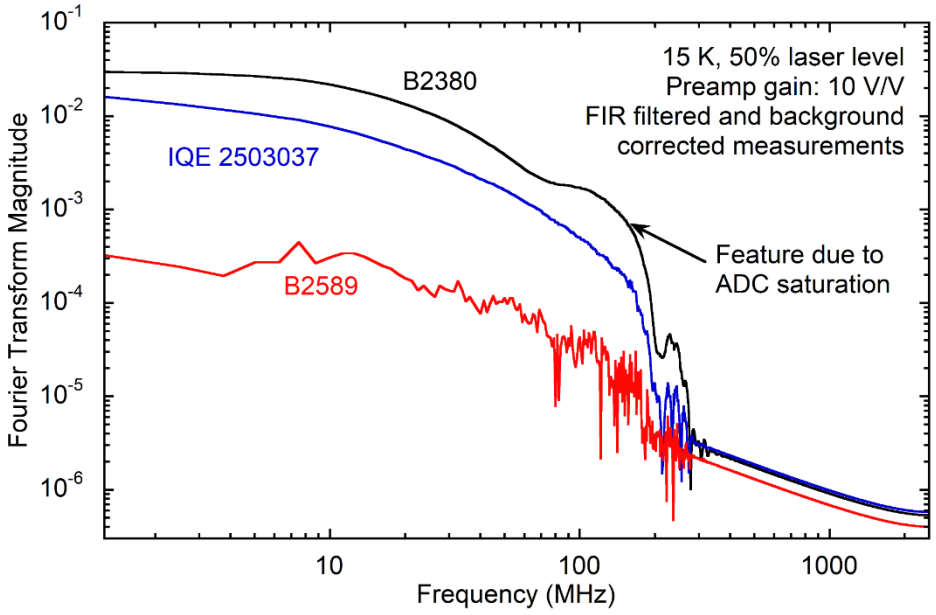

FIG. 25. PL signal magnitude as a function of frequency obtained by fast Fourier transform (FFT) of the time-domain signals in Fig. 24. Samples are 1 μm thick InAs sample B2380 (black), InAs/InAsSb T2SL sample IQE 2503037 (blue), and InAs/InAsSb T2SL sample B2589 (red). An anomalous feature near ~100 MHz is observed for the strongly emitting InAs sample due to saturation of the ADC card input.

2.6 Device Fabrication of Optically-Addressed Multiband Photodetectors

After the MBE growth and material characterizations, the photodetector samples were sent to ASU NanoFab for device processing. The processing included n-mesa etching, dielectric deposition, top contact deposition, mesa etching, bottom contact deposition, and annealing. FIG. 26 shows the layout pattern for the photomask of the photodetector device process on a 2-inch wafer using MLA 150.

Positive photoresist was used for all deposition steps and etching steps. Lift-off technique was used for top contact deposition and dielectric deposition. Therefore, the shaded area shows exposure region for deposition steps, while the clear area shows exposure region for etching steps. Ge (20 nm) / Ni (20 nm) / Au (300 nm) and Ti (50 nm) / Pt (50 nm) / Au (200 nm) were used as top contact and bottom contact, respectively. The top contact defined the size of the apertures, and the diameter of the apertures was designed to be 200, 500 or 1000 μm. A contact pad with diameter of 200 μm was designed for wire bonding in each device. Bottom contact was deposited onto the entire back side of the samples and no photolithography is required. Rapid thermal annealing (RTA) at 260 ° C for 1 minute in N_2 flow was used to form an Ohmic contact. Sputtered SiO_2 of 100 nm was used as dielectric. Wet etching was done with a mixture of acid and hydrogen peroxide. $HF:H_2O_2:H_2O$ with a volume ratio of 1:1:100 was used to etch the AlGaAsSb barrier layers and the GaSb absorber layers. $H_3PO_4:H_2O_2:H_2O$ with a volume ratio of 1:1:10 to etch the InAs/InAsSb T2SL layers. The phosphoric acid etchant exhibited relatively low etching rate of the AlGaAsSb barrier layers and the GaSb absorber layers, which can reduce the

undesired lateral etching of the AlGaAsSb barrier layers and the GaSb absorber layers. No surface passivation or anti-reflection coating was applied.

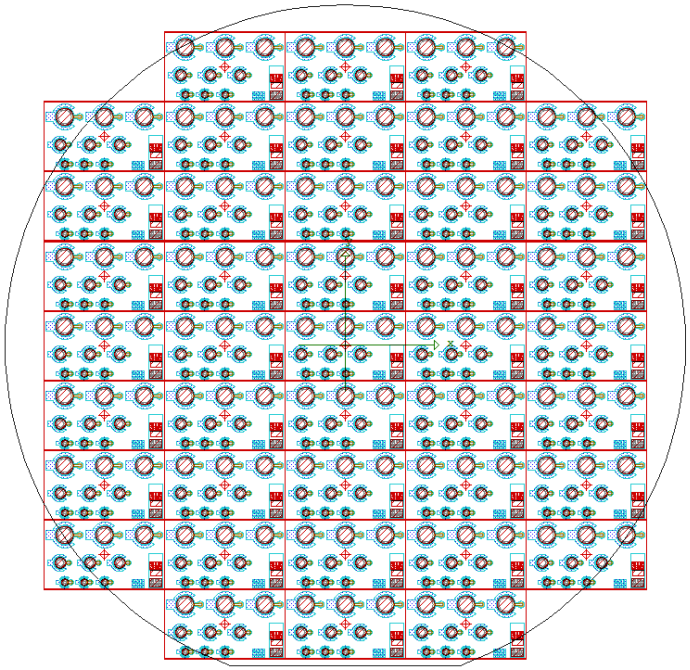

FIG. 26. MAL 150 layout pattern for the photomask of the photodetector device process on a 2-inch wafer.

2.7 Calculation of $\chi^{(2)}$ in Type-II Asymmetric Quantum Wells

Intersubband (ISB) $\chi^{(2)}$ nonlinearities require high doping,[53,55] are prone to large absorption near resonance,[45,56] and only engender one component of $\chi^{(2)}$ tensor, $\chi^{(2)}_{zzz} = d_{33}$.[44,90] For this reason, as early as 1987 it was proposed to extend the concept of envelope function engineering to the interband (IB) transition in AQWs.[56,90] The interband nonlinearity expands operational frequency range all the way to the bandgap energy, however, understanding the design and optimization of the $\chi^{(2)}$ requires extra effort because of the cancellation effects, as virtual transitions by electrons or holes tend to cancel each other.[44,90] Therefore, simply having asymmetrical envelope wavefunctions is not sufficient for large $\chi^{(2)}$.[91] If the valence band edge potential profile is the mirror image of the conduction band, then the nonlinear polarizabilities of virtual holes and electrons nearly cancel each other because the distance between the centers of charge of the lowest CB and highest VB subbands $\Delta z_{11} = (\int|\Psi_c|^2 - \int|\Psi_v|^2)zdz$ (interband charge shift) is very small. Therefore, using type-I asymmetric stepped QWs[89] (T1 ASQW) or asymmetric coupled quantum wells[53,90] (ACQW) previously studied for ISB $\chi^{(2)}$ does not result in large interband $\chi^{(2)}$. A schematic of T1 and T2 AQWs made of a modal materials system is shown in FIG. 27. The T1 and T2 band offsets shown in the schematic are set arbitrarily for simplicity without losing any generality. In theory, these band offsets can be realized using proper material choice and alloy compositions such as group III-V, II-VI, or IV-IV material systems. The two well regions in the T2 AQW form (i) an electron well with thickness l_1 and (ii) a hole well with thickness l_2. Although the material contains multiple QW's the barriers separating individual QW's are thick enough (>200nm) to suppress interwell coupling that greatly simplifies calculations by allowing to consider individual

QW's with semi-infinitely thick barriers. The conduction and valence band edges $E_{c1}, E_{c2}, E_{v1}, E_{v2}$ and E_{cb}, E_{vb} are defined for the electron well (well 1), hole well (well 2) and barriers, correspondingly. For simplicity, consider only unstrained (i.e. lattice-matched) well and barrier layers such that the heavy and light hole band edges are degenerate at the Γ point. Holding all the band offsets between the barriers and well layers constant, there are a total of six independent parameters specifying the AQW potential profile: well widths l_1 and l_2 for well 1 and well 2, and conduction and valence band edge offset $\Delta E_{c2,c1}$, $\Delta E_{v2,v1}, \Delta E_{c1,cb}$ and $\Delta E_{v1,vb}$ between the two wells and the barriers. The electron and hole wells in the T2 AQW may have either type-I or type-II alignment to the barriers, however the key property of the T2 AQW is the type-II alignment between the well layers which breaks the symmetry between conduction and valence band edges and results in spatial separation of the electron (e_1) and heavy-hole/light-hole (hh_1/lh_1) envelope wavefunction peaks. Schematically, this is shown by the charge shift $\Delta z_{11} = \left(\int |\Psi_{c,1}|^2 - \int |\Psi_{v,1}|^2\right) z dz$, which is small for the T1 ASQW, but much greater in the T2 AQW.[92]

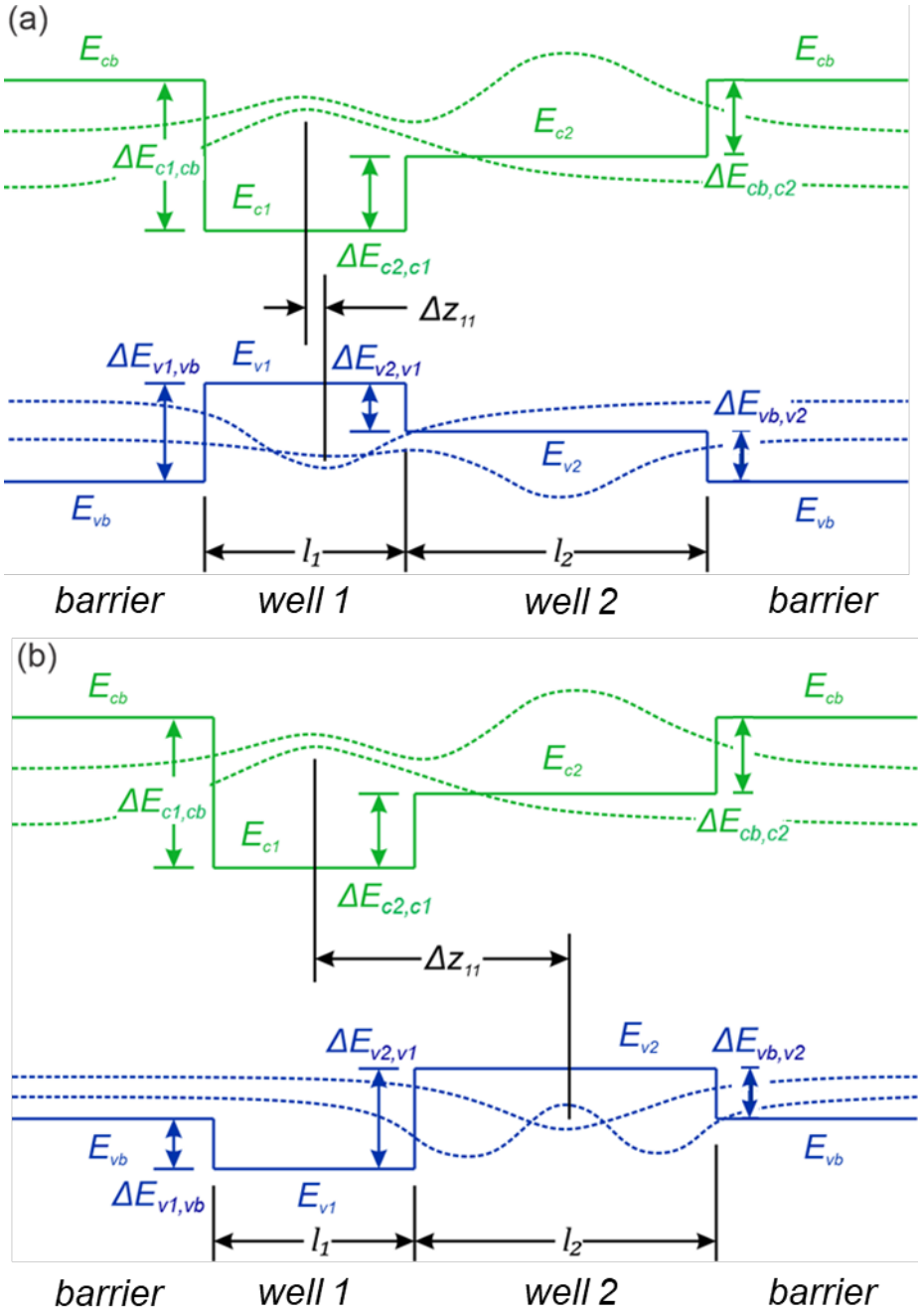

FIG. 27. (a) Type-I asymmetric quantum well (T2 AQW) and (b) type-II asymmetric quantum well (T2 AQW) schematic structure. Conduction (valence) band offsets shown as green (blue) lines. Electron well is denoted by layer 1 with width l_1 and hole well is denoted by layer 2 with width l_2. The band offsets of both barriers are identical, with semi-infinite thickness. [92]

The envelope wavefunctions for the quantum-confined electrons and holes are denoted as $\psi_{b_i,g}(z)$ with band index i = 1, 2, 3 for heavy holes (hh), electrons (e) and light holes (lh) respectively, and the subband index g = 1, 2, 3… The envelope wavefunctions in the AQW are determined by solving the one-dimensional time-independent Schrödinger equation using the finite difference method.[91] MATLAB R2020b is used to calculate the eigenfunctions and eigenenergies of the diagonal Hamiltonian matrix.

The interband $\chi^{(2)}$ is determined by the electric dipole moments $\boldsymbol{\mu}_{12,gm}$ for each possible transition doublet between bands b_1, b_2 and subbands g, m in the quantum well structure, respectively. The electric dipole transition moment $\boldsymbol{\mu}_{12,gm}$ between wavefunctions $\Psi_{b_1,g}$ and $\Psi_{b_2,m}$ is given by[59]

$$\boldsymbol{\mu}_{12,gm} = \langle \Psi_{b_1,g} | q\boldsymbol{r} | \Psi_{b_2,m} \rangle = q \int \Psi^*_{b_1,g} \boldsymbol{r} \Psi_{b_2,m} d^3\boldsymbol{r}. \tag{19}$$

The electronic wavefunction Ψ_g corresponding to band b_1 and subband g in a quantum well is described by[90]

$$\Psi_{b_1,g}(\boldsymbol{k},\boldsymbol{r}) = \psi_{b_1,g}(z)\, u_{b_1,g}(\boldsymbol{k},\boldsymbol{r}) e^{i\boldsymbol{k}_t \cdot \boldsymbol{r}_t}, \tag{20}$$

where $\psi_{b_1,g}(z)$ is the envelope function, which is determined by the quantum well potential profile, and $u_{b_1,g}(\boldsymbol{k},\boldsymbol{r})$ is the Bloch function, which is determined by the periodic potential of the crystal lattice. Combining Eq. (1) and (2) yields the dipole transition moment $\mu^i_{12,gm}$ in the direction $\hat{\boldsymbol{r}}_i$, where $i = x, y \; and \; z$ for all three spatial directions, for transitions from band b_1, subband g onto band b_2, subband m[90]:

$$\begin{aligned} \mu^i_{12,gm} &= \langle \Psi_{b_1,g}(z)\, u_{b_1,g}(\boldsymbol{k},\boldsymbol{r}) | q r_i | \psi_{2,m}(z)\, u_{b_2,m}(\boldsymbol{k},\boldsymbol{r}) \rangle \\ &= q \int \psi^*_{b_1,g}(z)\, u^*_{b_1,g}(\boldsymbol{k},\boldsymbol{r}) r_i \psi_{2,m}(z)\, u_{b_2,m}(\boldsymbol{k},\boldsymbol{r}) d^3\boldsymbol{r}. \end{aligned} \tag{21}$$

Consider only small values of the wavevector $\boldsymbol{k}$ near the Γ point corresponding to states which extend over many unit cells. Then the Bloch functions $u_{b_1,g}(\boldsymbol{k},\boldsymbol{r})$ are approximately constant[44] in the QW growth direction z, which has length on the order of ~10 nm. Further, assume parabolic band dispersion near the Γ point (effective mass approximation) with isotropic in-plane Bloch functions.[44,93] The effect of band nonparabolicity has been shown to be negligible in III-V semiconductors up to several kT above the Γ point.[55,93] The wavefunctions can be written in terms of in-plane wavevector $\boldsymbol{k}_t$ and in-plane position $\boldsymbol{r}_t$, and the out-of-plane wavevector k_z and position z, with $\boldsymbol{k} = k_z\hat{\boldsymbol{z}} + k_t\hat{\boldsymbol{r}_t}$ and $\boldsymbol{r} = z\hat{\boldsymbol{z}} + r_t\hat{\boldsymbol{r}_t}$. Separation of variables in the expression for the electric dipole moment yields

$$\mu^i_{12,gm} \approx q \int \psi^*_{b_1,g}(z)\, \psi_{2,m}(z) r_i\, u^*_{b_1,g}(k_t, r_t) u_{b_2,m}(k_t, r_t) dz d^2 r_t. \tag{22}$$

The QW is symmetric in the x-y plane. The directions x and y are equivalent,[56] and the in-plane electric interband dipole moments $\mu^x_{12,gm}$ and $\mu^y_{12,gm}$ In general, calculation of the interband matrix elements requires knowledge of the Bloch wavefunctions $u_{b_1,g}(\boldsymbol{k},\boldsymbol{r})$. A full-band simulation is required to determine the Bloch wavefunctions exactly. However, the dipole matrix element squared can be calculated in the parabolic band approximation from the momentum matrix element squared, $\left|\hat{\boldsymbol{x}} \cdot \boldsymbol{p}_{12,gm}\right|^2$[90,91],

$$\mu^x_{12,gm} = \mu^y_{12,gm} = \langle \psi_{b_1,g} | \psi_{b_2,m} \rangle \langle u_{b_1,g} | x | u_{b_2,m} \rangle. \tag{23a}$$

$$\begin{aligned} \left|\hat{\boldsymbol{x}} \cdot \boldsymbol{p}_{12,gm}\right|^2 &= m_0^2 \omega^2_{12,gm} \left|\hat{\boldsymbol{x}} \cdot \boldsymbol{\mu}_{12,gm}\right|^2 = m_0^2 \omega^2_{12,gm} \left|\mu^x_{12,gm}\right|^2 \\ &= m_0^2 \omega^2_{12,gm} \langle u_{b_1,g} | x | u_{b_2,m} \rangle \langle u_{b_2,m} | x | u_{b_1,g} \rangle \end{aligned} \tag{23a}$$

The Bloch functions constitute an orthonormal set[24] such that $\langle u_{b_1,g}|u_{b_2,m}\rangle = \delta_{b_1,b_2}$. Therefore, all electric dipole transition moments $\mu^z_{12,gm}$ in the z direction will be zero except for intersubband transitions with $b_1 = b_2$: [90,91]

$$\mu^z_{12,gm} = q\langle\psi_{b_1,g}|z|\psi_{b_2,m}\rangle\delta_{b_1,b_2}. \tag{24a}$$

$$\begin{aligned}\left|\hat{\boldsymbol{z}}\cdot\boldsymbol{p}_{12,gm}\right|^2 &= m_0^2\omega^2_{12,gm}\left|\hat{\boldsymbol{z}}\cdot\boldsymbol{\mu}_{12,gm}\right|^2 = m_0^2\omega^2_{12,gm}\left|\mu^z_{12,gm}\right|^2 \\ &= m_0^2\omega^2_{12,gm}\langle\psi_{b_1,g}\,|z|\psi_{b_2,g}\rangle\langle\psi_{b_2,g}\,|z|\psi_{b_1,g}\rangle\delta^2_{b_1,b_2}\end{aligned} \tag{24b}$$

The interband dipole transition moments depend on the envelope wavefunction overlaps and the interband dipole matrix element $q\langle u_{b_1,g}|x|u_{b_2,m}\rangle$. In general, calculation of the interband matrix elements requires knowledge of the Bloch wavefunctions $u_{b_1,g}(\boldsymbol{k},\boldsymbol{r})$. A full-band simulation is required to determine the Bloch wavefunctions exactly. However, the dipole matrix element squared can be calculated in the parabolic band approximation from the momentum matrix element squared, $\left|\hat{\boldsymbol{x}}\cdot\boldsymbol{p}_{12,gm}\right|^2$, according to[90,91]

$$\begin{aligned}\left|\hat{\boldsymbol{x}}\cdot\boldsymbol{p}_{12,gm}\right|^2 &= m_0^2\omega^2_{12,gm}\left|\hat{\boldsymbol{x}}\cdot\boldsymbol{\mu}_{12,gm}\right|^2 = m_0^2\omega^2_{12,gm}\left|\mu^x_{12,gm}\right|^2 \\ &= m_0^2\omega^2_{12,gm}\langle u_{b_1,g}|x|u_{b_2,m}\rangle\langle u_{b_2,m}|x|u_{b_1,g}\rangle\end{aligned} \tag{25a}$$

$$\begin{aligned}\left|\hat{\boldsymbol{z}}\cdot\boldsymbol{p}_{12,gm}\right|^2 &= m_0^2\omega^2_{12,gm}\left|\hat{\boldsymbol{z}}\cdot\boldsymbol{\mu}_{12,gm}\right|^2 = m_0^2\omega^2_{12,gm}\left|\mu^z_{12,gm}\right|^2 \\ &= m_0^2\omega^2_{12,gm}\langle\psi_{b_1,g}\,|z|\psi_{b_2,g}\rangle\langle\psi_{b_2,g}\,|z|\psi_{b_1,g}\rangle\delta^2_{b_1,b_2}\end{aligned} \tag{25b}$$

where $\omega_{12,gm}^2 = \left(E_{b_1,g}(k_t) - E_{b_2,m}(k_t)\right)/\hbar$ is the angular frequency for interband transitions, and $E_{b_1,g}(k_t)$ is the energy of the quantum-confined state in band b_1, subband g, which depends on the in-plane wavevector k_t according to the effective mass approximation.[93] In general, for type-II AQW structures the interband matrix elements will depend on the growth direction z for different layer materials. Therefore, its expectation value is calculated by weighting by the envelope wavefunctions:[93]

$$\langle|\hat{\boldsymbol{x}}\cdot\boldsymbol{p}_{12,gm}|^2\rangle = \left\langle\psi_{b_1,g}\middle||\hat{\boldsymbol{x}}\cdot\boldsymbol{p}_{12,gm}|^2\middle|\psi_{b_2,m}\right\rangle = \int \psi_{b_1,g}^*(z)|\hat{\boldsymbol{x}}\cdot\boldsymbol{p}_{12,gm}|^2\psi_{b_2,m}(z)\,dz. \tag{26}$$

Eq. 26 directs us to calculate the triple product of electric dipole moments including the product of dipole matrix elements between two transition doublets, e.g. $\langle u_{b_1,g}|x|u_{b_2,m}\rangle\langle u_{b_2,m}|x|u_{b_1,n}\rangle$. If the effective bandgap corresponding to the interband separation ω_{12} is much larger than the subband splitting in each band, we can write $\omega_{12,gm} \approx \omega_{12,nm}$ for the subbands. The product of dipole matrix elements for two transition doublets $\langle u_{b_1,g}|x|u_{b_2,m}\rangle\langle u_{b_2,m}|x|u_{b_1,n}\rangle$ can then be approximated as the geometric mean of the expectation value of the two momentum matrix elements $\langle|\hat{\boldsymbol{x}}\cdot\boldsymbol{p}_{12,gm}|^2\rangle$ and $\langle|\hat{\boldsymbol{x}}\cdot\boldsymbol{p}_{12,nm}|^2\rangle$, with

$$m_0^2\omega_{12,gm}\omega_{12,gn}\langle u_{b_1,g}|x|u_{b_2,m}\rangle\langle u_{b_2,m}|x|u_{b_1,n}\rangle \approx \sqrt{\langle|\hat{\boldsymbol{x}}\cdot\boldsymbol{p}_{12,gm}|^2\rangle}\sqrt{\langle|\hat{\boldsymbol{x}}\cdot\boldsymbol{p}_{12,nm}|^2\rangle}. \tag{27}$$

The bulk momentum matrix element is given by[93]

$$M_b^2(z) = \frac{m_0}{6}E_p(z), \tag{28}$$

where $E_p(z)$ is Kane's potential, which varies slightly with material type. Typical values for III-V materials are ~25 eV.[93] The x polarized (TE polarization) momentum matrix elements are given by[93]

$$\left|\hat{\boldsymbol{x}} \cdot \boldsymbol{p}_{12,gm}\right|^2(z) = \begin{cases} \frac{3}{4}\left(1+\cos^2\theta_{nm}(z)\right)M_b^2(z), c \to hh & \text{(29a)} \\ \left(\frac{5}{4}-\frac{3}{4}\cos^2\theta_{nm}(z)\right)M_b^2(z), c \to lh & \text{(29b)} \end{cases}$$

$$\left|\hat{\boldsymbol{z}} \cdot \boldsymbol{p}_{12,gm}\right|^2(z) = \begin{cases} \frac{3}{2}\, sin^2\theta_{nm}(z)\, M_b^2(z), c \to hh & \text{(29c)} \\ \frac{1}{2}\left(1+3\cos^2\theta_{nm}(z)\right)M_b^2(z), c \to lh & \text{(29d)} \end{cases}$$

where the momentum matrix element value differs depending on whether the transition $b_1 \to b_2$ is between conduction and heavy hole bands, or between conduction and light hole bands. The geometric factor $\cos^2\theta_{nm}(z)$ is a function of wavevector and effective mass, with

$$\cos^2\theta_{nm}(z) = \frac{E_{en}(z) + |E_{hm}(z)|}{E_{en}(z) + |E_{hm}(z)| + \frac{(\hbar k_t)^2}{2m_r^*(z)}} \tag{30}$$

$$E_{en}(z) = \frac{(\hbar k_{zn})^2}{2m_e^*(z)} \tag{31}$$

$$E_{hm}(z) = -\frac{(\hbar k_{zm})^2}{2m_h^*(z)}, \tag{32}$$

$$\frac{1}{m_r^*(z)} = \frac{1}{m_e^*(z)} + \frac{1}{m_h^*(z)}, \tag{33}$$

where $m_e^*(z)$, $m_h^*(z)$, and $m_r^*(z)$ are the electron, hole, and reduced effective masses (in kg) respectively. k_{zn} is the quantized out-of-plane wavevector corresponding to the n-th bound state in the QW, with

$$k_{zn} = \sqrt{2m_{en}^*\left(E_{c,n} - E_c\right)}/\hbar, \tag{34a}$$

$$k_{zm} = \sqrt{2m_{hm}^*\left(E_v - E_{h,m}\right)}/\hbar, \tag{34b}$$

where E_c and E_v denote the bulk band edges in the electron and hole wells, respectively.

The triple products of the electric dipole moments for the $\chi_{xxz}^{(2)}$, $\chi_{xzx}^{(2)}$, $\chi_{zxz}^{(2)}$, and $\chi_{zzz}^{(2)}$ tensors are written explicitly as[57,91,92]

$$\begin{aligned}
&\mu_{12,gm}^x \mu_{23,mn}^x \mu_{31,ng}^z \\
&= q^3 \langle \psi_{b_1,g} | \psi_{b_2,m} \rangle \langle \psi_{b_2,m} | \psi_{b_3,n} \rangle \langle \psi_{b_3,n} | z | \psi_{b_1,g} \rangle \langle u_{b_1,g} | x | u_{b_2,m} \rangle \langle u_{b_2,m} | x | u_{b_3,n} \rangle \delta_{b_3,b_1} \\
&\approx q^3 \langle \psi_{b_1,g} | \psi_{b_2,m} \rangle \langle \psi_{b_2,m} | \psi_{b_1,n} \rangle \langle \psi_{b_1,n} | z | \psi_{b_1,g} \rangle \frac{\sqrt{\langle |\hat{\boldsymbol{x}} \cdot \boldsymbol{p}_{12,gm}|^2 \rangle} \sqrt{\langle |\hat{\boldsymbol{x}} \cdot \boldsymbol{p}_{12,nm}|^2 \rangle}}{m_0^2 \omega_{12,gm} \omega_{12,nm}},
\end{aligned} \tag{35}$$

$$\begin{aligned}
&\mu_{12,gm}^x \mu_{23,mn}^z \mu_{31,ng}^x \\
&= q^3 \langle \psi_{b_1,g} | \psi_{b_2,m} \rangle \langle \psi_{b_2,m} | z | \psi_{b_3,n} \rangle \langle \psi_{b_3,n} | \psi_{b_1,g} \rangle \langle u_{b_1,g} | x | u_{b_2,m} \rangle \langle u_{b_3,n} | x | u_{b_1,g} \rangle \delta_{b_2,b_3} \\
&\approx q^3 \langle \psi_{b_1,g} | \psi_{b_2,m} \rangle \langle \psi_{b_2,m} | z | \psi_{b_2,n} \rangle \langle \psi_{b_2,n} | \psi_{b_1,g} \rangle \frac{\sqrt{\langle |\hat{\boldsymbol{x}} \cdot \boldsymbol{p}_{12,gm}|^2 \rangle} \sqrt{\langle |\hat{\boldsymbol{x}} \cdot \boldsymbol{p}_{21,ng}|^2 \rangle}}{m_0^2 \omega_{12,gm} \omega_{21,ng}},
\end{aligned} \tag{36}$$

$$\begin{aligned}
&\mu_{12,gm}^z \mu_{23,mn}^x \mu_{31,ng}^x \\
&= q^3 \langle \psi_{b_1,g} | z | \psi_{b_2,m} \rangle \langle \psi_{b_2,m} | \psi_{b_3,n} \rangle \langle \psi_{b_3,n} | \psi_{b_1,g} \rangle \langle u_{b_2,m} | x | u_{b_3,n} \rangle \langle u_{b_3,n} | x | u_{b_1,g} \rangle \delta_{b_1,b_2} \\
&\approx q^3 \langle \psi_{b_1,g} | z | \psi_{b_1,m} \rangle \langle \psi_{b_1,m} | \psi_{b_3,n} \rangle \langle \psi_{b_3,n} | \psi_{b_1,g} \rangle \frac{\sqrt{\langle |\hat{\boldsymbol{x}} \cdot \boldsymbol{p}_{13,mn}|^2 \rangle} \sqrt{\langle |\hat{\boldsymbol{x}} \cdot \boldsymbol{p}_{31,ng}|^2 \rangle}}{m_0^2 \omega_{13,mn} \omega_{31,ng}},
\end{aligned} \tag{37}$$

$$\mu^z_{12,gm}\mu^z_{23,mn}\mu^z_{31,ng} = q^3\langle\psi_{b_1,g}|z|\psi_{b_1,m}\rangle\langle\psi_{b_1,m}|z|\psi_{b_1,n}\rangle\langle\psi_{b_1,n}|z|\psi_{b_1,g}\rangle\delta_{b_1,b_2,b_3} \quad (38)$$

where Eq. 35, Eq. 36 and Eq. 37 provides the interband dipole matrix elements in terms of the readily-calculable momentum matrix elements, which depend only on the bulk material parameters: band offsets, effective masses, and Kane's potential.

The simplification that the Bloch functions for subbands g and n within the same band are identical: $u_{b_1,g} \approx u_{b_1,n}$ for all g, n h has been introduced here. The effect of band mixing is negligible, which is on the scale of $(\Delta E/E_g)^2$ where ΔE is the Intersubband splitting. As a result, the electric dipole moment $\mu^x_{12,gm}$ in Eq. 35 is non-zero only for $b_1 \neq b_2$ (interband transitions), while the electric dipole moment $\mu^z_{12,gm}$ in Eq. 37 is non-zero only for $b_1 = b_2$ (intersubband transitions).

The second order nonlinear susceptibility tensor element $\chi^{(2)}_{ijk}$ of the quantum well is given as[91]

$$\chi^{(2)}_{ijk}(\omega_1 + \omega_2, \omega_1, \omega_2) \quad (39)$$

$$= \frac{N_z}{2\varepsilon_0\hbar^2L^2}\mathcal{P}_I \sum_{b_1,b_2,b_3}\sum_{g,m,n} f_{b_1,g}(\boldsymbol{k})\sum_{k_t}\frac{\mu^i_{12,gm}\mu^j_{23,mn}\mu^k_{31,ng}}{\left(\omega_{21,mg}(\boldsymbol{k}_t) - \omega_1 - \omega_2\right)\left(\omega_{31,ng}(\boldsymbol{k}_t) - \omega_2\right)},$$

where ω_1 and ω_2 are the angular frequencies of the incident electric fields and N_z is number of quantum well periods per unit length. $f_{b_1,g}(\boldsymbol{k})$ is the Fermi function for band b_1 and subband g. Assuming intrinsic material with Fermi level in the middle of the gap, $f_{b_1,g}$ is unity for valence band states and zero for conduction band states. The complex angular

frequency $\omega_{21,mg}(\boldsymbol{k})$ for transitions from band b_2 and subband m to band b_1 and subband g is given by the difference between bound state energies:

$$\omega_{21,mg}(k_t) = \frac{E_{b_2,m}(\boldsymbol{k}_t) - E_{b_1,g}(\boldsymbol{k}_t)}{\hbar} - i\frac{\Gamma_{b_2,m}}{2}, \tag{40}$$

where $\Gamma_{b_2,m}$ is a dipole dephasing rate that is used to model damping phenomena such as LO phonon scattering and interface scattering in the perturbation solution to Schrödinger's equation.[59] The dephasing rates are a product of various scattering and recombination mechanisms.[55,93] In this work, the dephasing rate is treated as an adjustable broadening parameter with a typical value $\hbar\Gamma$ = 5 meV. [44,56] The bound state energy dispersion is assumed to be isotropic with respect to the in-plane wavevector k_t in the parabolic band (effective mass) approximation.

The first summation in Eq. 39 proceeds over all possible band triplets b_1, b_2, b_3; e.g. heavy hole subband 1 (hh_1), electron subband 1 (e_1), light hole subband 1 (lh_1), or hh_1, e_1, lh_1, etc. The second summation proceeds over all possible initial, intermediate, and final states triplets, which includes contributions from all bound states in the AQW. The intrinsic permutation operator $\mathcal{P}_I$ sums over all permutations of $(-\omega_1 - \omega_2, i)$, (ω_1, j), and (ω_2, k). Expressing Eq. 39 in integral form in terms of the isotropic in-plane wavevector k_t yields:

$$\chi^{(2)}_{ijk}(\omega_1 + \omega_2, \omega_1, \omega_2) \tag{41}$$

$$= \frac{N_z}{\pi\varepsilon_0\hbar^2}\mathcal{P}_I \sum_{b_1,b_2,b_3}\sum_{g,m,n}\int f_{b_1,g}(k_t)\frac{\mu^i_{12,gm}\mu^j_{23,mn}\mu^k_{31,ng}}{\left(\omega_{21,mg}(k_t) - \omega_1 - \omega_2\right)\left(\omega_{31,ng}(k_t) - \omega_2\right)}k_t dk_t$$

For intrinsic material with Fermi level in the middle of the band gap, the Fermi function $f_{b_1,g}(k_t)$ is unity for valence bands $b_1 = hh$ or lh, and is zero for conduction band $b_1 = e$. Eq. 39 can be further simplified as

$$\chi_{ijk}^{(2)}(\omega_1 + \omega_2, \omega_1, \omega_2) \tag{42}$$

$$= \frac{N_z}{\pi\varepsilon_0\hbar^2}\mathcal{P}_I \sum_{hh,b_2,b_3}\sum_{g,m,n}\int \frac{\mu_{2,gm}^i \mu_{23,mn}^j \mu_{31,ng}^k}{\left(\omega_{21,mg}(k_t) - \omega_1 - \omega_2\right)\left(\omega_{31,ng}(k_t) - \omega_2\right)} k_t dk_t$$

$$+ \frac{N_z}{\pi\varepsilon_0\hbar^2}\mathcal{P}_I \sum_{lh,b_2,b_3}\sum_{g,m,n}\int \frac{\mu_{12,gm}^i \mu_{23,mn}^j \mu_{31,ng}^k}{\left(\omega_{21,mg}(k_t) - \omega_1 - \omega_2\right)\left(\omega_{31,ng}(k_t) - \omega_2\right)} k_t dk_t.$$

It is apparent from the orthogonality property of the Bloch functions that only the $\chi_{xxz}^{(2)}$, $\chi_{xzx}^{(2)}$, $\chi_{zxx}^{(2)}$, and $\chi_{zzz}^{(2)}$ tensor elements are nonzero. This works considers only the interband $\chi^{(2)}$ tensor elements, we thus do not consider the ISB $\chi_{zzz}^{(2)}$ tensor element any further. The triple product of electric dipole moments in the numerator of Eq. 39 are computed according to Eq. 22. The envelope wavefunction overlaps are straightforwardly computed from the 1D quantum-confined wavefunctions in the z direction, while the interband dipole matrix elements $\langle u_{b_1,g}|x|u_{b_2,m}\rangle$ are calculated from the momentum matrix elements $\left|\hat{\boldsymbol{x}} \cdot \boldsymbol{p}_{12,gm}\right|^2$[44,93] At the Γ point with k_t = 0 the momentum matrix elements squared for hh – e and lh – e transitions are $m_0E_p/4$ and $m_0E_p/12$ respectively,[93] where the Kane potential E_p ranges from 15 to 25 eV for all common semiconductors.[93]

Near the electron - heavy hole interband resonance, the summation in Eq. 10 is dominated by a single term,[57] namely the product of the interband dipole matrix elements and the charge shift Δz_{11} between the first electron and heavy hole envelope wavefunctions, with

$$\chi_{ijk}^{(2)}(\omega_1+\omega_2,\omega_1,\omega_2) \tag{43}$$

$$\approx \frac{N_z}{3\pi\varepsilon_0\hbar^2}\langle u_{c,1}|x|u_{hh,1}\rangle^2 \int \frac{\langle\psi_{e,1}|\psi_{hh,1}\rangle\langle\psi_{hh,1}|\psi_{e,1}\rangle[\langle\psi_{e,1}|z|\psi_{e,1}\rangle-\langle\psi_{hh,1}|z|\psi_{hh,1}\rangle]}{(\omega_{21,mg}(k_t)-\omega_1-\omega_2)(\omega_{31,ng}(k_t)-\omega_2)}k_t k_t$$

$$=\frac{N_z}{3\pi\varepsilon_0\hbar^2}\langle u_{c,1}|x|u_{hh,1}\rangle^2 \int \frac{\langle\psi_{e,1}|\psi_{hh,1}\rangle\langle\psi_{hh,1}|\psi_{e,1}\rangle\Delta z_{11}}{(\omega_{21,mg}(k_t)-\omega_1-\omega_2)(\omega_{31,ng}(k_t)-\omega_2)}k_t dk_t.$$

It is strongly dependent on charge shift that clearly shows the advantages of T2 AQW structure, particularly advantageous for nearly-resonant optical rectification and difference frequency generation applications in the far IR and THz spectrum where powerful laser sources are not available.

2.8 Comparison of $\chi^{(2)}$ in Different Types of Quantum Wells

Three types of asymmetric quantum well structures have been compared to demonstrate the advantages of the type-II band alignment: (i) asymmetric coupled quantum well (ACQW), (ii) type-I asymmetric stepped quantum well (T1 ASQW), and (iii) type-II asymmetric quantum well (T2 AQW). The $\chi^{(2)}$ of each structure is product of the electric dipole moments and envelope wavefunction overlaps (numerator in Eq. 10), but also the transition frequencies $\omega_{21,mg}$ (denominator in Eq. 10). To elucidate the differences between structures which are due solely to the quantum well potential profile, a two-step design process is undertaken. First, the well widths of a lattice-matched InP/$Al_{0.38}Ga_{0.10}In_{0.52}As$ T2 AQW are optimized to yield maximum $\chi^{(2)}$ for nearly-resonant optical rectification. Then, the well widths of a lattice-matched $Al_{0.35}Ga_{0.12}In_{0.53}As/Al_{0.48}In_{0.52}As$ ACQW and a $Al_{0.27}Ga_{0.20}In_{0.53}As/Al_{0.42}Ga_{0.06}In_{0.52}As$ T1 ASQW are selected to yield the same ground state interband transition frequency between the e_1 and hh_1 bound states. With equal interband transition frequencies, equal total well width of 10 nm, identical $Al_{0.48}In_{0.52}As$ barriers, and approximately the same well material compositions, the three structures differ only in their potential profiles and envelope wavefunctions, permitting direct comparison of the T2 AQW to the previously studied ACQW and T1 ASQW structures.[55,56,90,91]

FIG. 28 shows the $\left|\chi^{(2)}_{xzx}\right|$ and $\left|\chi^{(2)}_{zxx}\right|$ tensor elements as a function of T2 AQW well width asymmetry $l_1/(l_1+l_2)$ for nearly-resonant optical rectification (OR). The $\chi^{(2)}_{xxz}$ tensor is vanishingly small for nearly-resonant OR and is not shown. Nearly-resonant OR

is a simple application of interband resonance[47,59] to enhance $\chi^{(2)}$ where the input optical fields ω_1 and ω_2 are equal in magnitude and opposite in sign and are detuned slightly from the first interband resonance. Mathematically, nearly-resonant OR is described by $\omega_1 = \omega_0 - \delta\omega$ and $\omega_2 = -\omega_1$, where ω_0 is the interband transition frequency and $\delta\omega$ is a detuning energy. In the limit as $\delta\omega$ approaches zero, full resonance is achieved. However, this results in large interband absorption and high loss.[47,59] Typical operation therefore utilizes small detuning $\delta\hbar\omega$ of ~10-100 meV such that absorption losses are minimal, but the magnitude of $\chi^{(2)}$ is enhanced. The FIG. shows that $\chi^{(2)}_{xzx}$ approaches a maximum at l_1 = 1.5 nm in the $l_1 + l_2$ = 10 nm wide well, corresponding to interband transition energy $\hbar\omega_0$ = 1.300 eV (954 nm) in the InP/$Al_{0.38}Ga_{0.10}In_{0.52}As$ well.

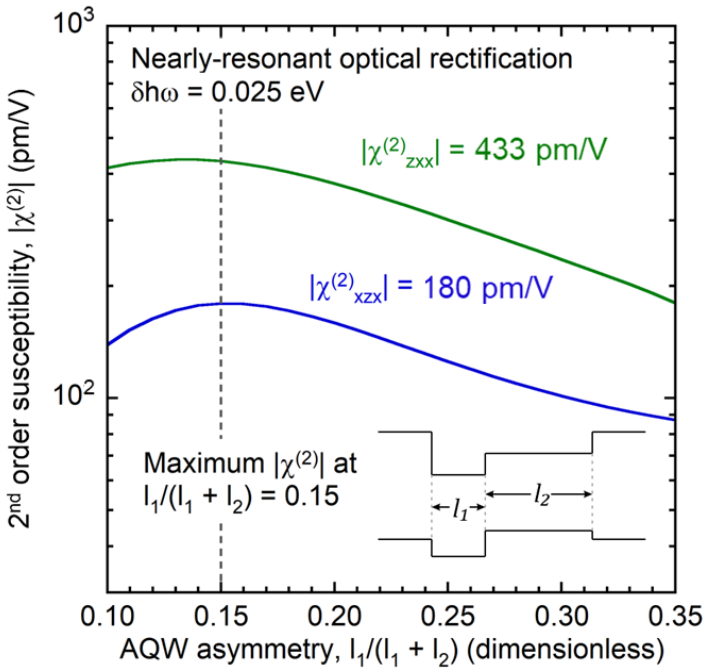

FIG. 28. Second order susceptibility tensor elements $\left|\chi^{(2)}_{xzx}\right|$ (blue curve) and $\left|\chi^{(2)}_{zxx}\right|$ (green line) as a function of the well width asymmetry $l_1/(l_1 + l_2)$ in the InP / $Al_{0.38}Ga_{0.10}In_{0.52}As$ T2 AQW structure. The total well width $l_1 + l_2$ is held constant at 10 nm. Nearly-resonant optical rectification (OR) with $\omega_1 = \omega_0 - \delta\hbar\omega$ and $\omega_2 = -\omega_1$ is shown, where the transition frequency ω_1 is detuned by $\delta\hbar\omega$ = 25 meV from the interband resonant transition frequency ω_0. The $\chi^{(2)}_{xzx}$ tensor element reaches a maximum for l_1 = 1.5 nm. [92]

The well widths of an $Al_{0.35}Ga_{0.12}In_{0.53}As/Al_{0.48}In_{0.52}As$ ACQW and an $Al_{0.27}Ga_{0.20}In_{0.53}As$ / $Al_{0.42}Ga_{0.06}In_{0.52}As$ T1 ASQW lattice-matched to InP are selected to yield the same interband transition energy $\hbar\omega_0$ = 1.3 eV as in the T2 AQW structure optimized in FIG. 27. The resulting quantum well potential profiles are illustrated in FIG. 29, along with the electron, heavy hole, and light hole envelope wavefunctions squared. FIG. 29(a) shows the ACQW structure with l_1 = 2.6 nm, l_b = 2.0 nm, and l_2 = 5.4 nm. The ACQW design is similar to InGaAs / AlInAs structures previously studied for ISB second harmonic generation.[49,55,57] FIG. 29(a) shows the T1 ASQW structure with l_1 = 1.8 nm and l_2 = 8.2 nm. Fig. 3c shows the T2 AQW structure with l_1 = 1.5 nm and l_2 = 8.5 nm. The first two electron, first two heavy hole, and first light hole bound states are calculated.

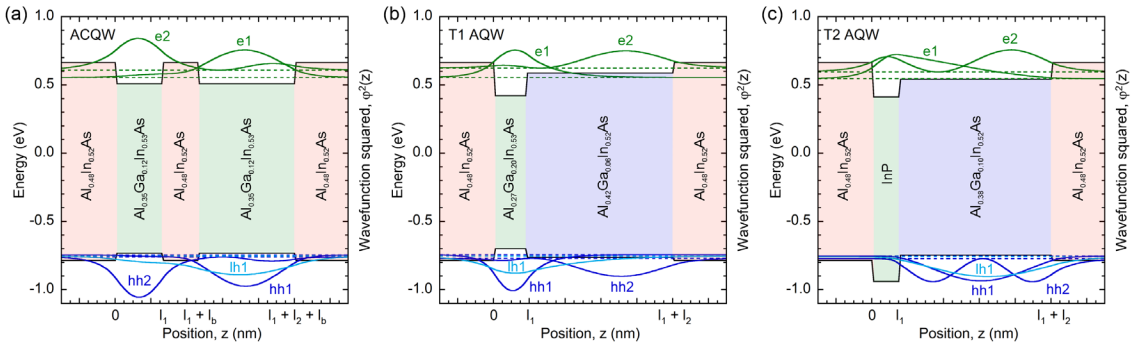

FIG. 29. Schematic layer structure of band offsets and envelope wavefunctions squared for (a) ACQW structure, (b) T1 ASQW structure, and (c) T2 AQW structure. All three quantum well structures are lattice-matched to InP with a ground state $e_1 - hh_1$ transition energy of 1.300 eV. [92]

The transition energies, envelope wavefunction overlap, interband transition dipole matrix element, and interband charge shift are shown in Table 3 for each interband transition in the three AQWs. The six interband transition energies between electron and hole states are nearly identical for the three AQWs and differ by less than -0.2/+1.9% from the T2 AQW structure. Likewise, the interband dipole matrix elements vary within +1.2/-1.5% of the T2 AQW structure, a consequence of the similar effective masses and Kane potentials for the well materials. The structures differ significantly in their envelope wavefunction overlaps, however, with both ACQW and T1 ASQW structures exhibiting nearly unity overlap between the e_1 - hh_1, e_1 - lh_1, and $e_2 - hh_2$ states, and small overlap between the other states. In contrast, the T2 AQW exhibits moderate overlap between all quantum confined states. The T1 and T2 structures also differ greatly in the charge shift $\Delta z_{12,gm}$. Most importantly, the T2 AQW exhibits large $\Delta z_{12,gm}$ between the $e_1 - hh_1$ and $e_1 - lh_1$ states, whereas $\Delta z_{12,gm}$ between the first quantum-confined states is minimal in the T1 ASQW and ACQW. This is evident in Fig. 29 where the 1st electron and hole bound states are observed to be confined within the same well layer for the ACQW and T1 ASQW

structures but are spatially separated across the two well layers in the T2 AQW structure. Additionally, the sign of $\Delta z_{12,gm}$ is the same for each interband transition in the T2 AQW and the electric dipoles sum constructively, in contrast to the T1 structures where the sign varies and cancellations occur.

Structure	Interband transition	Transition energy, $\hbar\omega_{12,gm}$ (eV)	Envelope wavefunction overlap, $\langle\psi_{b_1,g}\|\psi_{b_2,m}\rangle$	Interband dipole matrix element, $\|\hat{\boldsymbol{x}}\cdot\boldsymbol{r}_{12,gm}\|$ (Å)	Charge shift , $\Delta z_{12,gm}$ (nm)
ACQW (Fig. 29a)	$e_1 - hh_1$	1.300	0.993	5.01	-0.25
	$e_1 - lh_1$	1.307	0.971	2.88	0.61
	$e_1 - hh_2$	1.315	0.097	4.96	4.98
	$e_2 - hh_1$	1.354	-0.093	4.81	-4.83
	$e_2 - lh_1$	1.362	0.173	2.76	-3.97
	$e_2 - hh_2$	1.369	0.985	4.76	0.39
T1 ASQW (Fig. 29b)	$e_1 - hh_1$	1.298	0.984	4.98	0.27
	$e_1 - lh_1$	1.309	0.962	2.85	-0.49
	$e_1 - hh_2$	1.325	-0.136	4.88	-5.36
	$e_2 - hh_1$	1.367	0.093	4.73	5.80
	$e_2 - lh_1$	1.378	-0.243	2.71	5.04
	$e_2 - hh_2$	1.395	0.990	4.64	0.17
T2 AQW (Fig. 29c)	$e_1 - hh_1$	1.300	0.771	4.97	-3.94
	$e_1 - lh_1$	1.307	0.790	2.86	-4.53
	$e_1 - hh_2$	1.315	0.337	4.90	-4.50
	$e_2 - hh_1$	1.354	-0.617	4.78	-0.17
	$e_2 - lh_1$	1.362	-0.598	2.75	-0.76
	$e_2 - hh_2$	1.369	0.586	4.71	-0.73

Table 3. Interband transition energies, envelope wavefunction overlap, interband dipole matrix elements, and difference of center of charge for the AQW structures shown in Fig. 29. The first two electron, first two heavy hole, and first light hole bound states are considered[92].

From a practical point of view, the application of SHG makes little sense for mid IR due to the limited efficiency and availability of the powerful laser sources. Therefore, the interband $\chi^{(2)}$ tensor elements for the three AQW structures are only calculated for (a)

nearly-resonant OR, (b) singly-resonant difference frequency generation (DFG) at 25 THz (0.103 eV), and (c) doubly-resonant DFG near the $e_2 - e_1$ ISB transition. Singly-resonant DFG makes use of the large increase in $\chi^{(2)}$ in interband type-II AQWs as the field frequency approaches the interband resonance and is suitable for the generation of THz radiation from a near-infrared pump laser.[93] The first field component (pump field) ω_1 is detuned slightly from the first interband resonant transition, and the second field component (output field) is held constant at 25 THz. Singly-resonant DFG can be described by $\omega_1 = \omega_0 + \omega_2 - \delta\omega$, where ω_0 is the interband transition frequency, $\delta\omega$ is a detuning energy, and the output field component ω_2 = -25 THz is held fixed. Doubly-resonant DFG enhances $\chi^{(2)}$ further by placing the output field component ω_2 in resonance with an ISB transition;[56,95] e.g. the $e_2 - e_1$ transition. This relationship is expressed by $\omega_2 = -\omega_{0,ISB}$ and $\omega_1 = \omega_{0,IB} + \omega_2 - \delta\omega$, where $\omega_{0,ISB}$ and $\omega_{0,IB}$ are the ISB and IB transition frequencies, respectively. A constant detuning energy $\delta\hbar\omega$ = 25 meV, broadening parameter $\hbar\Gamma$ = 5 meV, and mid-gap Fermi level E_F = -0.1 eV is used in the calculation of $\chi^{(2)}$ at room temperature, 300 K.

FIG. 30 directly compares the IB $\chi^{(2)}$ tensor elements of the three AQW structures. The T2 AQW structure (green bars) exhibits enhanced $\chi^{(2)}$ in all applications except for the small $\chi^{(2)}_{zxx}$ tensor element for singly-resonant 25 THz DFG. In particular, the $\chi^{(2)}_{xzx}$ tensor element is enhanced by approximately one order of magnitude in the T2 AQW vs the ACQW and T1 ASQW structures. The ACQW and T1 ASQW structures exhibit approximately equal $\chi^{(2)}$ values which can be intuitively understood from their nearly

identical envelope wavefunction overlaps and dipole matrix elements shown in table 3. The enhancement of $\chi^{(2)}$ in the T2 AQW is a result of the large center of charge difference between the $e_1 - hh_1$ and $e_1 - lh_1$ states, in contrast to the ACQW and T1 ASQW structures with small separation of charge for the first quantum-confined states. The electron and hole envelope wavefunction peaks in the T2 AQW are confined in separate well layers at each subband; e.g. the e_1 wavefunction is confined to the InP well while the hh_1/lh_1 wavefunctions are confined to the AlGaInAs well. The spatial separation of the electron and hole wavefunctions within each subband contributes to a large interband electric dipole moment in the type-II aligned structure and thus increases the achievable $\chi^{(2)}$. This spatial separation of wavefunction peaks within each subband is absent in the type-I aligned structures where significant cancellations between inter- and intra-band transition dipole moments occur.[96]

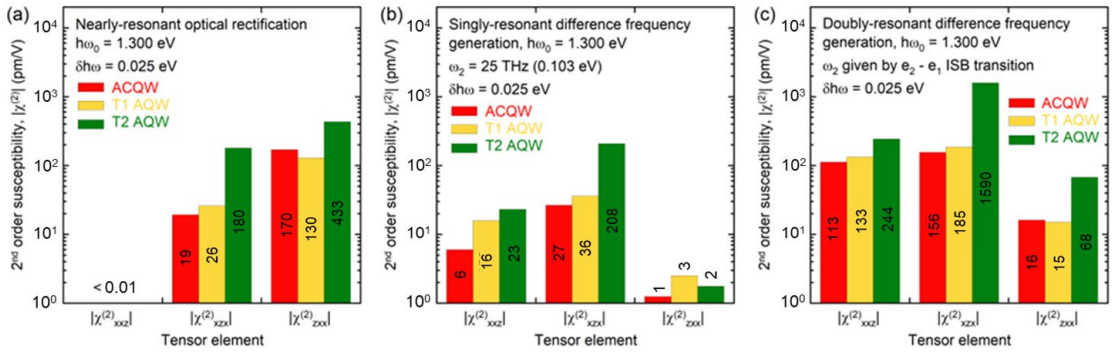

FIG. 30. Second order susceptibility tensor elements $\left|\chi^{(2)}_{xxz}\right|$, $\left|\chi^{(2)}_{xzx}\right|$, and $\left|\chi^{(2)}_{zxx}\right|$ for (a) nearly-resonant optical rectification, (b) singly-resonant difference frequency generation at 25 THz (103 meV), and (c) doubly-resonant difference frequency generation at the $e_2 - e_1$ ISB transition, all at a detuning energy $\delta\hbar\omega$ = 25 meV.

The $\chi^{(2)}_{xzx}$ tensor element in the T2 AQW (FIG. 29c) ranges from 180 to 1.60×10^3 pm/V and exceeds the values reported for an electrically biased GaAs / $Al_{0.4}Ga_{0.6}As$ quantum

well with $\chi_{xzx}^{(2)} \approx$ 20 pm/V,[43] as wells as a type-I GaAs/AlGaAs AQWs with reported values[45] of ~1000 pm/V and a type-I GaAs/$Al_{0.15}Ga_{0.85}As$ THz quantum cascade structure[98] operated near interband resonance with $\chi_{xzx}^{(2)}$ ~450 pm/V. Conversely, the $\chi_{xzx}^{(2)}$ in the AlGaInAs/AlInAs T1 ASQW (FIG. 28(b)) agrees well with the values reported GaAs/AlGaAs structures.[45,95] The interband $\chi^{(2)}$ in the T2 AQW is enhanced by 1-2 orders of magnitude over natural bulk crystals[96,97] such as $LiNbO_3$ with $\chi_{zxx}^{(2)}$ = 8.6 pm/V and $\chi_{zzz}^{(2)}$ = 50.4 pm/V, KTP with $\chi_{zxx}^{(2)}$ = 7.4 pm/V and $\chi_{zzz}^{(2)}$ = 29.2 pm/V, or GaAs with$\chi_{zxy}^{(2)}$ = 340 pm/V.

2.9 Optimization of $\chi^{(2)}$ in Type-II Asymmetric Quantum Wells

The interband second order susceptibility can be further enhanced by optimizing the asymmetric quantum well widths and band offsets. The conduction band offset ($\Delta E_{c2,c1}$) and valence band offset ($\Delta E_{v2,v1}$) are defined in Eq. 44(a) and (b) such that $\Delta E_{c2,c1}$ and $\Delta E_{v2,v1}$ are defined as step well band edges subtracted by the InP band edges. There should exist a global maximum (and numerous local maxima) in the $\chi^{(2)}$ tensor elements as l_1 and $\Delta E_{c2,c1}$ and $\Delta E_{v2,v1}$ are varied. To maintain the type-II band alignment, the conduction band offsets $\Delta E_{c2,c1}$ varies from 0.025 to 0.250 eV ($\Delta E_{c2,c1} > 0$), while valence band offsets $\Delta E_{v2,v1}$ varies from 0.180 to 0.300 eV ($\Delta E_{v2,v1} > 0$), and the electron well width and l_1 varies from 1 to 8 nm. The corresponding ground state $\mathrm{e}_1 - \mathrm{hh}_1$ transition energy E_0 as a function of electron well width l_1, conduction band offset $\Delta E_{c2,c1}$, and valence band offset $\Delta E_{v2,v1}$ranges from 1.180 to 1.377 eV, smaller than the bandgap of $Al_{0.48}In_{0.52}As$. This confirms that the $\mathrm{e}_1 - \mathrm{hh}_1$ interband transition is confined within the quantum well. The ground state transition energies vary by less than 0.2 eV and therefore the influence of this variation on the magnitude of $\chi^{(2)}$ is minimal.

$$\Delta E_{c2,c1} = E_{c2} - E_{c1} \tag{44a}$$

$$\Delta E_{v2,v1} = E_{v2} - E_{v1} \tag{44b}$$

The second order susceptibility tensor elements increase with narrower interband transition energies as seen in the denominator of Eq. 39. Therefore, a fair comparison of tensor elements between structures with varying interband transition energies can be achieved by normalizing the $\chi^{(2)}$ tensor values by the interband transition energies $E_0 = \hbar(\omega_{e1} - \omega_{hh1})$. The resulting figures of merit $\left|\chi^{(2)}\right| \cdot E_0$, FIG 31, has units of length$\cdot q$

(picometers $\cdot\, q$).[92] With the parameters listed above, maximum normalized tensor elements $\left|\chi^{(2)}_{xzx}\right| \cdot E_0$ and $\left|\chi^{(2)}_{zxx}\right| \cdot E_0$ are calculated for nearly-resonant OR (see Fig 31). Compared with the original T2 AQW design demonstrated in Fig. 28(c), the normalized $\chi^{(2)}_{xxz}$ tensor is again vanishingly small, but the normalized $\chi^{(2)}_{xzx}$ and $\chi^{(2)}_{zxx}$ are approximately 2~3 times larger. This optimization study of T2 AQW structures suggests that narrower electron and wider hole wells give larger second order susceptibility tensor elements than wider electron and narrower hole wells. Larger conduction band and valence band offsets tend to enhance the $\chi^{(2)}_{xzx}$ tensor element but reduce the $\chi^{(2)}_{zxx}$ tensor element. These general guidelines suggest that the optimum T2 AQW design will vary depending on the geometry of incident and extracted electric fields on a nonlinear optical device and thus the $\chi^{(2)}$ tensor element utilized.

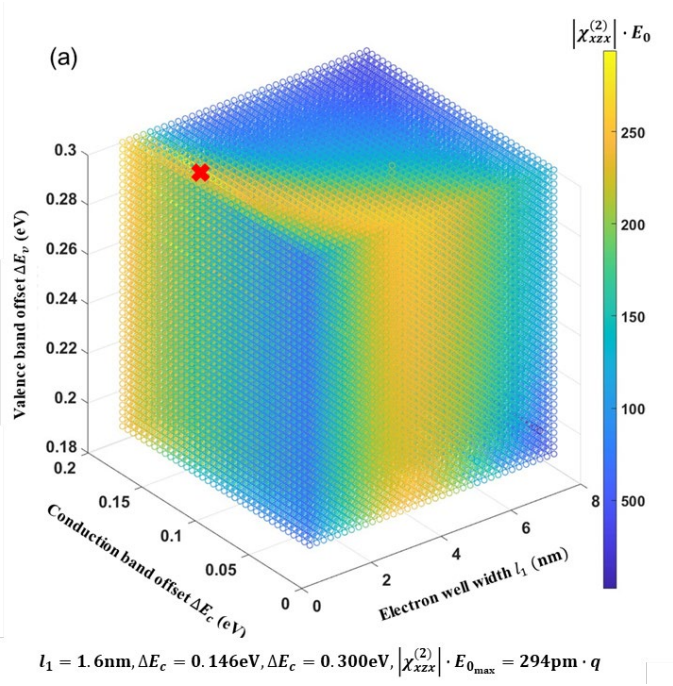

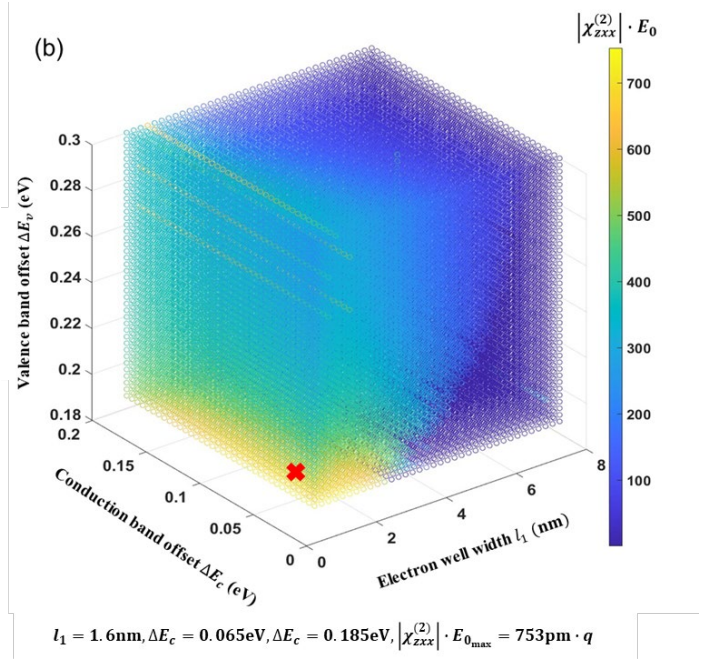

FIG. 31. Normalized second order susceptibility tensor elements (a) $\left|\chi^{(2)}_{xzx}\right| \cdot E_0$, and (b) $\left|\chi^{(2)}_{zxx}\right| \cdot E_0$ for nearly-resonant OR at constant detuning energy $\delta\hbar\omega$ = 25 meV as a function of T2 AQW width l_1 and band offsets ΔE_c and ΔE_v. The optimized parameters for all three tensor elements are marked with red crosses which give the maximum normalized values.[92]

The resonant enhancement achieved by the interband nonlinearity is smaller than that achieved for intersubband nonlinearity with $\chi_{zzz}^{(2)}$ up to ~10^5 pm/V demonstrated for second harmonic generation in type-I GaInAs/AlInAs ACQWs.[53] However, the IB nonlinearity has the advantage of engendering large off-diagonal $\chi^{(2)}$ tensor elements which enable nonlinear optical response to both s- and p-polarized electric fields, whereas the $\chi_{zzz}^{(2)}$ tensor for the ISB nonlinearity is only excited by electric fields polarized normal to the growth plane (s-polarization).[48,50,52,58] The IB nonlinearity enables additional geometries for quasi-phase matching and additional operating wavelengths for photonic devices that are inaccessible by the extensively studied ISB nonlinearity.

CHAPTER 3

CdSe THIN FILM WITH MIXED ZINCBLENDE AND WURTZITE PHASES GROWN ON InAs USING MOLECULAR BEAM EPITAXY

3.1 Molecular Beam Epitaxy of CdSe growth on InAs

The CdSe thin films were grown by the II-VI MBE system, on (100) and (111)B-oriented InAs substrates that are indium-mounted to Si wafers. The ZB InAs(111) crystal plane with an in-plane lattice constant of 4.28 Å is highly suitable as a substrate for the epitaxial growth of monocrystalline wurtzite CdSe, which has a lattice constant a = 4.30 Å, making InAs an attractive choice due to its small lattice mismatch with the WZ phase is only -0.35%. [69] The substrate preparation, including oxide desorption and growth of a 100 – 500 nm-thick As-terminated InAs buffer layer, is carried out in the III-V chamber, followed by transfer under ultrahigh-vacuum to the II-VI chamber for CdSe epitaxy. The InAs buffer layer growth proceeds at a temperature of 500 °C, flux ratio As/In = 5 for 1 monolayers per/s monolayers per second (ML/s), and As/In = 20 for 0.12 monolayers per second (ML/s) on (100) and (111)B-oriented substrates, respectively. The substrate temperature for the CdSe growth is calibrated using an Ircon Modline 3 (model 3G-10C05) pyrometer, and ranges from 250 °C to 350 °C. Effusion cells containing elemental Cd and Se source materials enable their independent flux controls. The Cd/Se flux ratios range from 0.74 for Se-rich (Cd-limited) growth to 6.75 for Cd-rich (Se-limited) growth. The CdSe growth rate ranges from 0.14 to 0.84 ML/s. Reflection-high-energy electron diffraction (RHEED) monitors the surface reconstructions during the growth of the InAs

buffer layers and the bulk CdSe layers. Information about the samples and their growth conditions are summarized in Table 4.

Sample number	InAs substrate orientation	CdSe growth temperature (°C)	Cd/Se flux ratio	CdSe growth rate (ML/s)
1 (A1950)	(100)	250	1.35	0.84
2 (A1952)	(111)	250	1.35	0.84
3 (A1957)	(111)	300	0.74	0.55
4 (A1953)	(111)	300	1.35	0.80
5 (A1955)	(111)	300	6.75	0.14
6 (A1956)	(111)	350	1.35	0.83

Table 4. Summary of the CdSe samples and their growth conditions.

The RHEED patterns for CdSe grown on InAs(111) at different stages are shown in Fig. 31. Prior to initiation of CdSe growth, the prepared InAs substrate exhibits a streaky 1×1 surface reconstruction with four-fold symmetry, which is characteristic of an atomically-smooth ZB crystal surface. The 1×1 reconstruction is initially present during the CdSe layer growth (Fig. 32a), followed by the gradual appearance of doubled spots on the 1× streaks connected by Kikuchi lines (Fig. 32b). Finally, a complete transition to a spotty/streaky 1×1 surface reconstruction with six-fold symmetry appears (Fig. 32c), which is characteristic of a roughened wurtzite (0001) crystal surface.

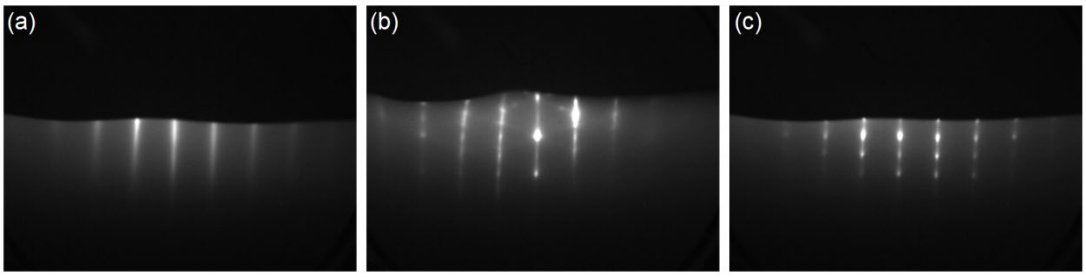

FIG. 32. RHEED patterns for CdSe grown on InAs(111) (a) at initiation of CdSe growth, (b) after 4 minutes of CdSe growth, and (c) after 9 minutes of CdSe growth.

3.2 Structural and Optical Measurement of CdSe Thin Films

Scanning electron microscopy (SEM) images of the CdSe thin film samples are acquired using a Hitachi S-4700 field emission microscope at a beam-accelerating voltage of 15 kV. FIG. 32 shows cross-section SEM images of the CdSe thin films grown on InAs(100) and (111) substrates at different temperatures and with different Cd/Se flux ratios. CdSe thin film grown under Cd-rich conditions at 250 °C (Fig. 33a) on the InAs(100) substrate results in a high-quality with a well-defined interface between the CdSe layer and the underlying InAs buffer layer. CdSe grown under Cd-rich condition on InAs(111)B substrate at 250 °C (Fig. 33b) yields a relatively uniform thin film with an apparent phase transition after the first ~100 nm, which is indicated by the change in the cleavage plane. In contrast, CdSe grown under Cd-rich conditions at 350 °C (Fig. 33c) yields a rough with numerous polygonal crystallites on InAs buffer. CdSe grown on InAs(111)B under Se-rich conditions at 300 °C (as shown in Fig. 33d) yields nanocolumns with approximately hexagonal cross-sections, indicating the presence of wurtzite (WZ) crystal structure. These results reveal that the film morphology is strongly dependent on both the growth temperature and the Cd/Se flux ratio.

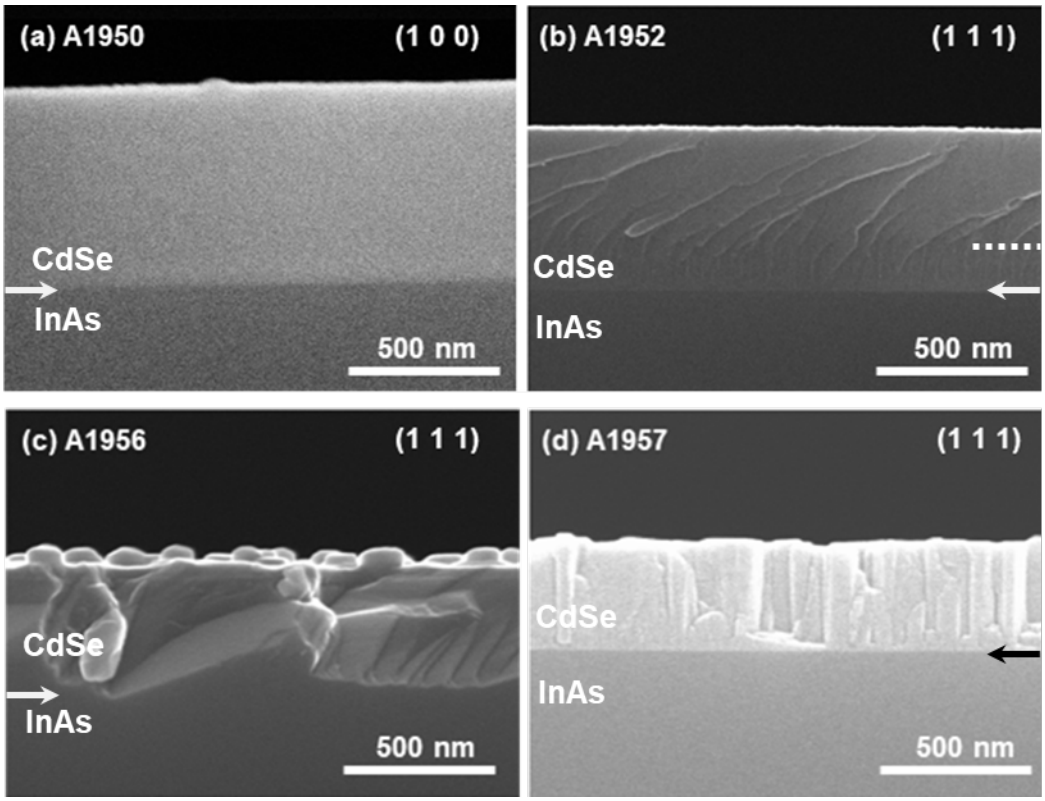

FIG. 33. Cross-section SEM images of CdSe thin films grown on InAs(100) and (111)B: (a) (100), 250 °C, Cd/Se flux ratio = 1.35, (b) (111), 250 °C, Cd/Se flux ratio = 1.35, (c) (111), 350 °C, Cd/Se flux ratio = 1.35, and (d) (111), 300 °C, Cd/Se flux ratio = 0.74. The CdSe and InAs layers are labeled, and the interfaces are indicated with arrows.

High-resolution coupled ω-2θ X-ray diffraction (XRD) scans of the (100) and (111) crystal planes are acquired using a Panalytical X'Pert Pro MRD triple-axis diffractometer, and are also simulated using the Panalytical X'Pert Epitaxy dynamical diffraction modeling program. A four-bounce hybrid monochromator provides Cu K-α illumination with wavelength λ = 1.5406 Å. The CdSe material parameters, including lattice constant, Poisson ratio, Debye-Waller factor, and X-ray scattering factors, are obtained from the literature[69,98-100]. FIG. 34(a) shows the ω-2θ XRD scan of (400) planes for the CdSe layers grown on InAs(100)-oriented substrates at 250 °C with Cd-rich growth condition. A distinguishable CdSe layer peak indicates the growth of ZB structure with lattice constant

$a_0 = 6.077$Å which matches previous reported lattice constant of ZB CdSe.[98,99] Coupled ω-2θ XRD scans of the (111) planes for CdSe layers grown on InAs(111)B-oriented substrates, as shown in Fig. 34(b), indicate primarily compressively strained material in agreement with the reported values for possible ZB and WZ lattice constants of the two phases.[69,99] Both samples are grown at 300 °C under Cd-rich conditions, and show pronounced epilayer peaks, which are attributed to the highly uniform film morphology and the presence of phase transition (Fig. 33(b)). However, the phases of the CdSe films cannot be easily identified due to the proximity of the ZB CdSe (111) peak with the WZ CdSe (0002) peak. The positions of the CdSe layer peaks and broad shoulders which are located in between the fully strained and fully relaxed CdSe angles possibly are attributed to the presence of mixed-phase CdSe.

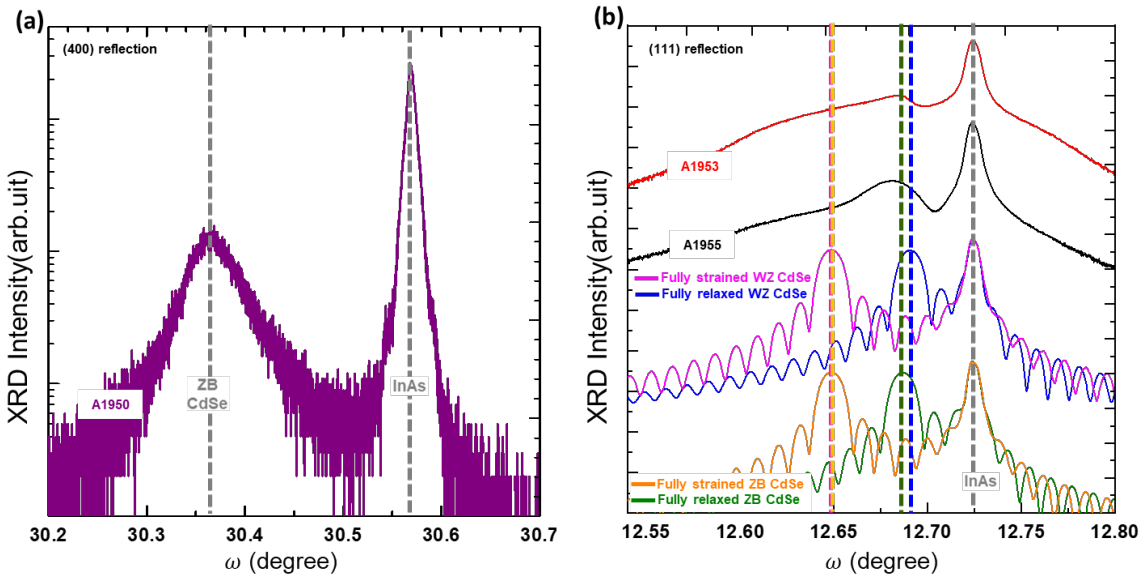

FIG. 34. Coupled ω-2θ scans of the (a) (400) and (b) (111) reflections for the CdSe layers grown on InAs (100) and (111)-oriented substrates, respectively. The simulation curves of fully strained and fully relaxed ZB and CdSe on InAs (111) substrate are plotted in (b). Vertical dashed lines are for clear indications of the Bragg angles for ZB InAs, fully strained and fully relaxed ZB CdSe, and fully strained and fully WZ CdSe. Sample numbers are labeled on each curve.

CdSe thin film cross-section samples suitable for TEM observation are prepared by gallium ion milling using a dual-beam Thermo Fisher Helios 5G UX system, initially at 30keV with subsequent thinning at 5kV and 2kV to reduce the amount of surface damage. Electron micrographs were recorded with an image-corrected Thermo Fisher Titan 80-300 operated at 300 kV. TEM and fast Fourier-transform (FFT) analyses are performed on (100) and (111)-oriented samples to accurately determine the phases of CdSe grown, as depicted in FIG. 35 showcasing TEM results for two of the as-grown CdSe thin films. FIG. 34(a) shows the TEM results of the CdSe layer grown on InAs (100) substates with occasional inclined (111)-type stacking faults, while its corresponding FFT patterns verify the ZB phase structure throughout the CdSe thin film. Numerous stacking faults are present in CdSe layers in FIG. 35(b), the corresponding Fast Fourier-transform (FFT) patterns for the [110] projection reveal mostly WZ phase, but patches of the ZB phase, which confirm the mixed-phase growth of the CdSe thin film, are also present.

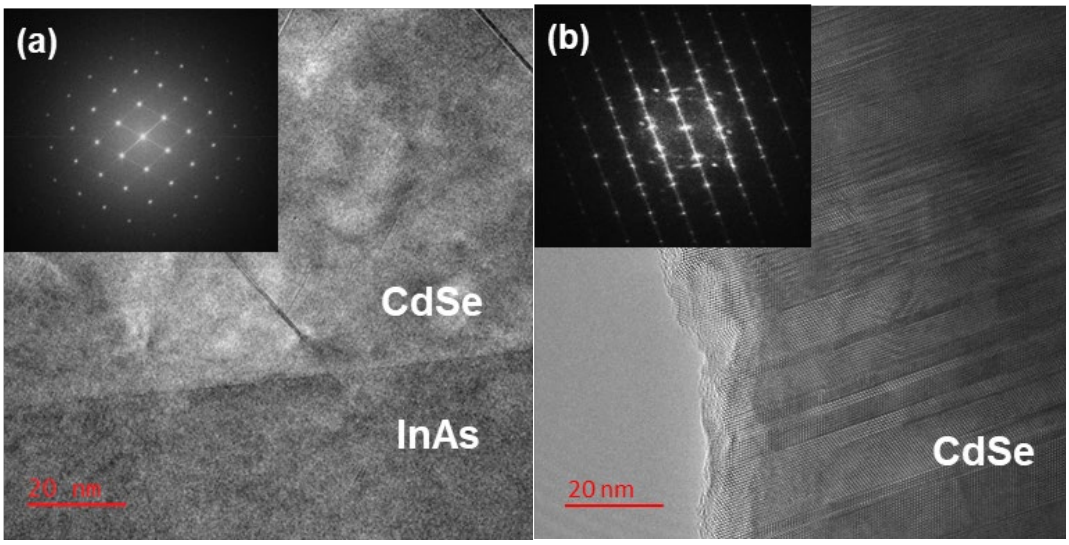

FIG. 35. TEM images and corresponding FFTs of bulk CdSe layers grown on (a) InAs(100) substrate at 250 °C, Cd/Se flux ratio of 1.35, and (b) InAs(111) at 300 °C, Cd/Se flux ratio of 6.75. **Image acquired by Dr. Martha McCartney and Dr. David Smith at ASU.*

PL spectroscopy measurements are acquired using a Horiba iHR 550 monochromator equipped with a CCD detector and InGaAs array detector. A 532 nm CW diode laser is used for sample excitation. Optical properties of the CdSe thin films grown on different substrates under different conditions are characterized by using room-temperature PL. As shown in Fig. 36, the PL peak of the CdSe thin film grown on (100) substrate is at 743 nm (1.67 eV) which is consistent with earlier research that proposed a ZB CdSe bandgap of 1.67 eV.[99] The peak position and the strong PL intensity further confirms the excellent crystal quality and monocrystalline of ZB CdSe grown on InAs (100) substrates. The PL peaks of CdSe thin films grown on (111)B substrates with a Cd/Se flux ratio of 1.35, are between 713 nm (1.74 eV) and 743 nm, which is due to the mixed phases of ZB and WZ present in the thin films. Thin films grown at higher temperatures exhibit stronger PL with peaks closer to 713 nm, which indicates better crystallization of the thin films and a dominant WZ-phase. The CdSe thin film grown at 350 °C exhibits almost the same PL peak wavelength as that grown via rapid thermal evaporation (RTE).[61] However, the full-width half-maximum (FWHM) of the PL peak is 46 nm, which is twice the value reported previously[61], indicating the mixture of WZ and ZB phases in the thin film. The CdSe thin film grown with a Cd/Se flux ratio of 6.75 demonstrates reduced PL intensity and longer peak wavelength in comparison to films grown with lower Cd/Se flux ratios. These are attributed to a higher defect density, along with the presence of significant ZB-phase crystals, as confirmed by TEM observations shown in Fig 35(b). The PL spectrum of the CdSe thin film grown with a Cd/Se flux ratio of 0.74 is extremely broadened, which suggests a high density of defects and a mixture of different phases, as shown in Fig. 37.

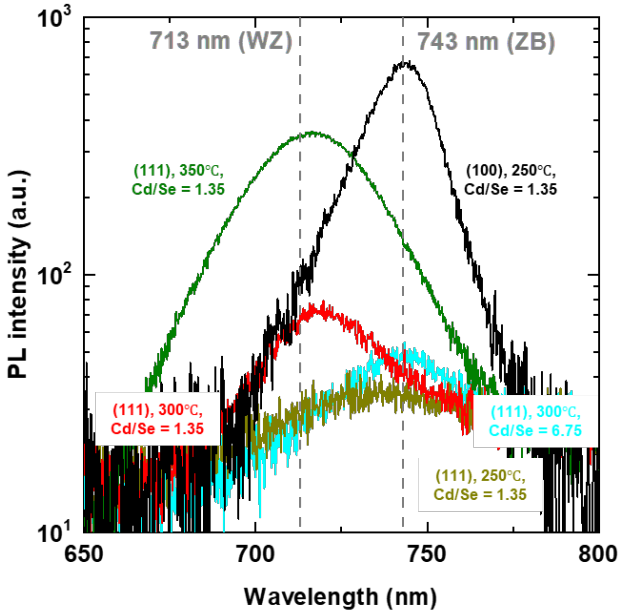

FIG. 36. Room temperature PL spectra for CdSe layers grown on InAs(100) and (111) substrates. Substrates and growth conditions are indicated in the figure. Dashed lines indicate the PL peaks attributed to ZB and WZ CdSe at 743 nm and 713 nm, respectively.

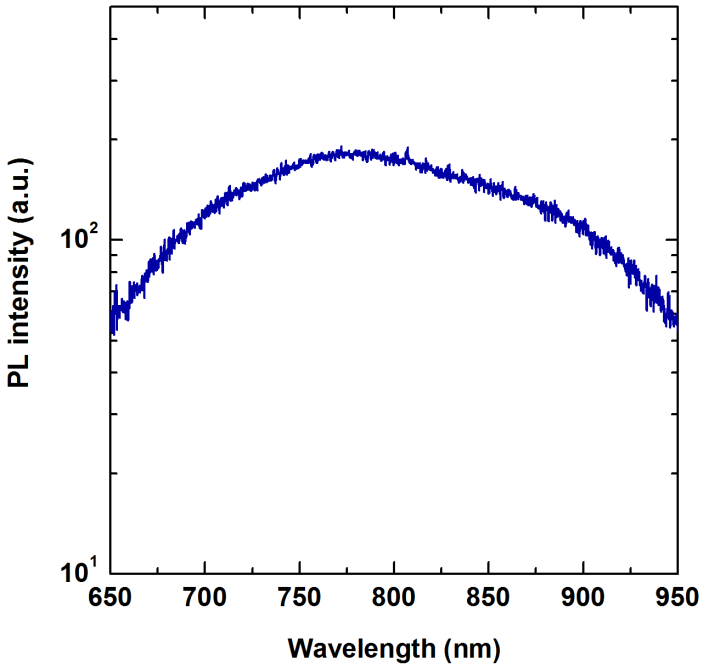

FIG. 37. Room temperature PL spectra for bulk CdSe layers grown on InAs(111)B substrates at 300 °C at Cd/Se flux ratio of 0.74. The extremely broadened PL spectrum suggests mixed phases and defects.

Post-growth annealing on the CdSe thin film grown at 250 °C with a Cd/Se flux ratio of 1.35 is carried out to study phase transitions of the CdSe films. To protect the CdSe thin film, a 100-nm-thick SiN_x layer is deposited onto the CdSe sample via plasma-enhanced chemical vapor deposition (PECVD) at 250 °C prior to annealing. The sample is then loaded into a furnace to process annealing for 5 minutes. PL spectra of the CdSe thin film before and after annealing are shown in Fig. 38a. In the range from 300 °C to 400 °C, the CdSe thin films annealed at higher temperatures exhibit almost 3 times stronger PL peak intensity with peak wavelength closer to 713 nm, which is the wavelength of WZ CdSe. This trend is consistent with the relationship between PL performance and growth temperature shown in Fig. 36. However, annealing at 450 °C does not further increase the PL peak intensity, and the PL peak position blue-shifts past the recorded WZ CdSe wavelength, which is a result that we currently cannot explain. The relation between PL peak position, PL intensity and annealing temperature is shown in Fig. 39b.

The phase transition of CdSe crystals after annealing is further studied by TEM, as shown in Fig. 39. High-resolution TEM image and the corresponding FFTs confirm the WZ structure of the CdSe crystals after annealing at 450 °C. No sign of ZB structure is observed. The results of both PL and TEM characterizations reveal that CdSe crystals tend to become WZ phase at higher temperatures, which reduces the amount of mixed phase and thus reduces the boundaries between two different phases. This result also reveals that the ZB structure remains stable when the annealing temperature is elevated to 300 °C, indicating good thermal stability of the ZB phase below 400 °C, which is comparable to the value of 460 °C reported from the previous study of the ZB CdSe grown on GaAs.[100]

Conversely, the WZ phase exhibits greater favorability and stability at elevated temperatures.

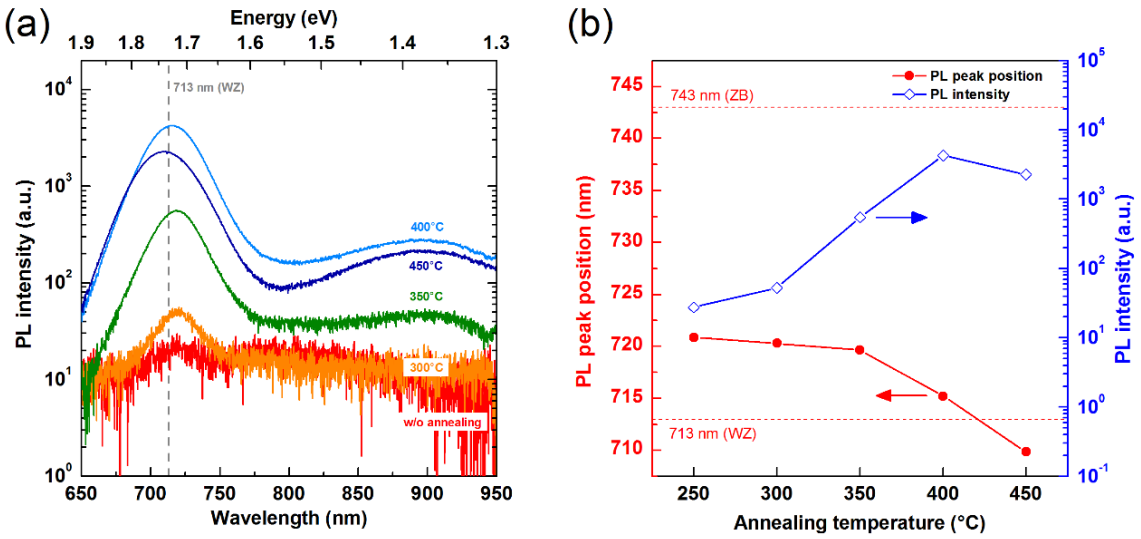

FIG. 38. (a) Room-temperature PL spectra for bulk CdSe layers annealed at different conditions. Annealing temperatures are labeled on each curve. (b) Plot of PL peak position and PL intensity vs. annealing temperature.

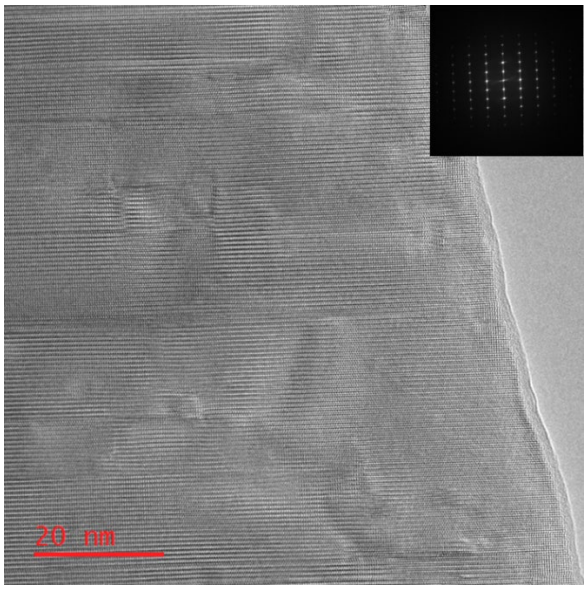

FIG. 39. TEM images of CdSe thin film grown at 250 °C at a Cd/Se flux ratio of 1.35 after 450 °C annealing. **Image acquired by Dr. Martha McCartney and Dr. David Smith at ASU.*

3.3 Density Functional Theory of Mixed Phases in CdSe

DFT simulations are used to elucidate the energy differences between the ZB and WZ phases for III-V systems, and to examine the orientation dependence of the interface energy for the WZ and ZB phases of CdSe on ZB InAs. All calculations are carried out using VASP[103,104] code and PAW-LDA (Ceperley-Alder based) pseudopotential[103] in the static lattice limit (no thermal or zero-point energy corrections). The local density approximation (LDA) is adopted since the corresponding static lattice parameters obtained from the generalized gradient approximation (GGA) either match or exceed the observed lattice constants even without the inclusion of thermal corrections. Convergence tolerances, number of planes waves and reciprocal lattice grids, are optimized to ensure high energy and structure convergence. Atomic positions and cell dimensions are all simultaneously optimized.

The coexistence of both ZB and WZ phases within compound semiconductor epitaxial thin films is uncommon. In order to elucidate the origin of mixed-phases observed in the CdSe growth on InAs(111)B substrates we therefore first compare the energy differences in bulk phases of III-V materials using DFT simulation. Table 5 provides a summary of structural parameters obtained for CdSe and several common III-V compound semiconductors GaN, InAs and GaAs, as well as the static lattice energy differences between the ZB and WZ phases. The energy difference between ZB and WZ CdSe (only a few meV per formula unit) is markedly smaller than and approximately only 20% of those for other common III-V compound semiconductors. This slight energy difference may in part account for the observed coexistence of the ZB and WZ phases within CdSe films.

	ZB	WZ		ΔE_0(ZB-WZ)
	a (Å)	a(Å)	c (Å)	(meV)
CdSe	6.019 (6.050)[100]	4.256 (4.299)[106]	6.955 (7.015)[106]	3.4
GaN	4.453 (4.503)[107]	3.150 (3.189)[108]	5.136 (5.185)[108]	12.2
InAs	6.032 (6.058)[102]	4.254 (4.274)[109]	6.995 (7.025)[109]	15.5
GaAs	5.627 (5.653)[110]	3.865 (3.898)[110]	6.538 (6.564)[110]	22.1

Table 5. Static lattice ground state structures of CdSe and some III-V systems, and the energy difference between their ZB and WZ phases. The values in the parenthesis are experimental values of the lattice constants.[55,100,106-110] **Values calculated by Dr. Andrew Chizmeshya at ASU.*

Simulations of the interfaces corresponding to ZB CdSe (111) and WZ CdSe (0001) epilayers grown on ZB InAs(111)B were also carried out. These were studied using 64-atom slabs in which the "top" and "bottom" half-slab portions each contains 32 atoms and thus one interface and two free surfaces. The in-plane dimensions of the supercells were fixed at the substrate (InAs) equilibrium values and all remaining spatial atomic positions were optimized. The various interfaces were simulated by selecting the group-III or group-V atom species corresponding to "A" or "B" type surface termination, as well as the ZB (A-B-C-A-…) or WZ (A-B-A-B-…) type stacking sequence for the CdSe epilayer. In all cases, the calculations predict that A-B and B-A type interfaces (In-Se and As-Cd, respectively) are much more favorable than their A-A or B-B type (As-Se and In-Cd, respectively) counterparts. FIG. 40 shows the structures of the three lowest energy models containing As-Cd type interfaces with a common InAs(111)B substrate, either WZ or ZB B-type CdSe overlayers, and Cd-Se different stacking sequences. The lowest energy model

was found to be (c), consisting of CdSe(ZB) on InAs(ZB). The dashed red line in the figure circumscribes the common structure in models (b) and (c), Here, specifically, the InAs substrate portion and the first two layers of CdSe are identical but subsequent Cd-Se layers differ. The 1.0 meV per III-V pair energy differences between the two models originates in the bonding sequence of the last two layers. As shown in Table 5 (above), this energy difference is comparable to the formation energy of bulk ZB and WZ phases of CdSe. Finally, those interface calculations were repeated with defects (vacancies and group V-atom exchange) in the interface layer and no change in relative energetics or ordering of the models shown in FIG. 40 was found. Full structural relaxation of the models in the presence of ±1% tensile/compressive basal strain slightly reduces the energy differences uniformly while preserving all trends.

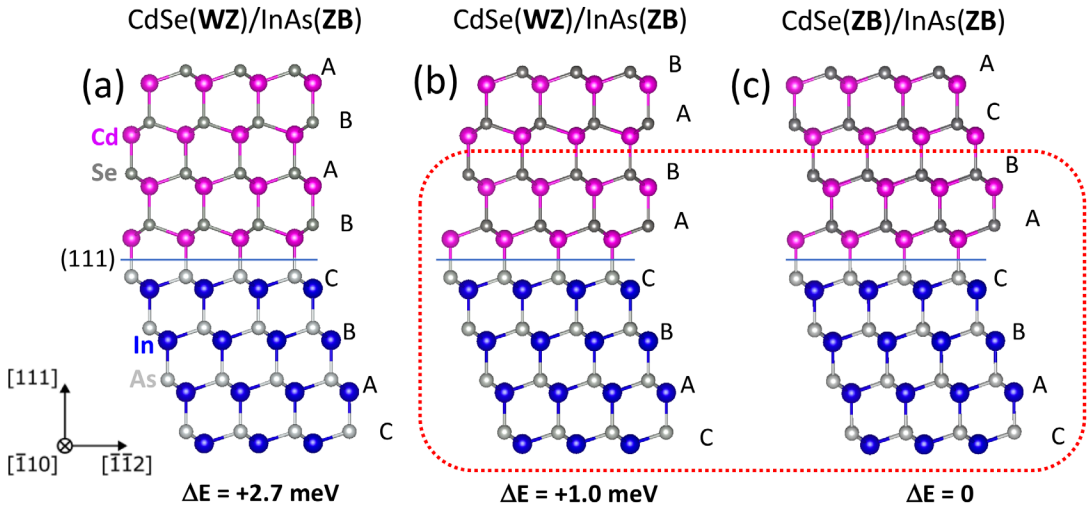

FIG. 40. The schematic models of CdSe layers on ZB InAs (111)B contain As-Cd bonded interfaces. The dashed red line indicates the interface and stacking sequence common to models (b) and (c). Energy differences between models are given in meV per formula unit (III-V pair). **Diagram generated by Dr. Andrew Chizmeshya at ASU.*

Referring back to the ZB monocrystalline CdSe grown on InAs (100)B substrate, it remains evident that the CdSe epitaxial layers maintain interaction with the ZB substrate

and continue to align with its structural orientation throughout the growth process. Both the interfacial layer of atoms and the arrangement of the subsequent layer beneath play a crucial role in influencing and restricting initiation of the uppermost epitaxial layers. The CdSe layers grown on InAs(111)B substrates are expected to conform to the same underlying physical principle, leading to the adoption of a ZB (111) structural orientation in the epitaxial layers. However, this anticipated behavior is challenged by the relatively minor energy difference in formation between ZB and WZ CdSe, which poses a unique complication.

CHAPTER 4

CONCLUSION AND FUTURE WORK

4.1 Conclusion

A dual-band short- and mid-wavelength infrared optically-addressed photodetector based on type-II InAs/$InAs_xSb_{1-x}$ superlattices and GaSb is designed, simulated, and grown by molecular beam epitaxy. High-resolution x-ray diffraction and photoluminescence measurements indicate the active layers are of excellent crystalline quality and exhibit first-rate optical performance. Additionally, secondary ion mass spectrometry measurements confirm Te and Be doping levels in GaSb and the T2SL layers up to the level which are mandatory for the device fabrication. The design and fabrication of optically-addressed tri-band IR detectors extended to long-wavelength infrared is theoretically examined. An analytical model is developed and utilized for the design and simulation of luminescence coupling and light leakage effects in optically-addressed tri-band photodetectors. A method to reduce crosstalk is identified by increasing the absorber thickness and diminishing luminescence efficiency. The processing flow with innovative contact pads design and fabrication recipe have completed developed. Dark current, external quantum efficiency, and spectral responsivity measurements are identified as methods that will provide a comprehensive understanding of the device performance.

Utilizing its physical property, asymmetric quantum wells with type-II band alignment exhibit enhanced interband second-order susceptibility $\chi^{(2)}$ are compared with conventional type-I aligned structures. Direct comparison between type-I and type-II band alignment is accomplished by designing structures with identical total well width of 10 nm and interband transition energy of 1.3 eV using the lattice-matched InP/AlInAs/AlGaInAs

materials system. Further optimization of the type-II asymmetric quantum well width, conduction band offset, and valence band offset identifies global maxima in $\chi^{(2)}$ for nearly-resonant optical rectification. The optimization study suggests that comparatively narrow electron well widths and large valence band offset between electron and hole wells are key to achieving high interband $\chi^{(2)}$. The $\chi^{(2)}$ enhancement is a result of the spatial separation between electron and hole wavefunction peaks into separate well layers in the type-II structure. The separation of electron and hole wavefunctions within each subband results in larger electric dipole moments than can be achieved in type-I aligned structures. Additionally, operation near the interband resonance at a suitable detuning energy of 25 meV greatly enhances $\chi^{(2)}$ by 1-2 orders of magnitude over natural bulk crystals such as $LiNbO_3$, KTP, or GaAs. The InP/AlGaInAs type-II asymmetric quantum well is composed of mature III-V compound semiconductor materials which can be grown by standard techniques such as MBE or CVD. These properties recommend type-II asymmetric quantum wells for future ultra-compact on-chip integrated photonics.

The molecular beam epitaxy growth of II-VI CdSe thin films on III-V InAs(100) and (111)B substrates is investigated. The transition of RHEED pattern during the CdSe growth on InAs(111)B substrates reveals 3D island growth which is consistent with observed scanning electron microscopy results. Photoluminescence, X-ray diffraction, and transmission electron microscopy measurements indicate that the optical and structural properties of the CdSe films are strongly dependent on substrate orientation, growth temperature, and the Cd/Se flux ratio. The epitaxial material grown on the (111)B substrate displays the coexistence of ZB and WZ phases, as confirmed by XRD, TEM, and PL measurements. Only the single ZB phase is evident in the material grown on the (100)

substrate. DFT calculations reveal that the coexistence of ZB and WZ phases of CdSe on InAs(111)B is due to their small formation energy difference and the similar energies of their interfacial bonding sequence. Annealing experiments demonstrate a phase transition in CdSe crystals, shifting from a ZB to a WZ structure at elevated temperatures. No obvious ZB phase CdSe is observed in the annealed sample by TEM and its corresponding FFT.

4.2 Future Work

The dual-band short- and mid-wavelength infrared optically-addressed photodetector are currently in the process of fabrication with the primary aim of showcasing the operational principles of optical addressing. Work should continue on revising the structure design and fabricating optically-addressed tri-band IR detectors using GaSb and InAs/InAsSb type-II superlattices. Additionally, in the development of a tri-band device, several crucial steps need to be undertaken to ensure its performance and functionality. A more comprehensive model will need to be created to account for all noise sources inherent in the device, including shot noise, Johnson/thermal noise, and 1/f noise. Additional modeling will help in understanding and quantifying the noise characteristics of the device. Secondly, the noise equivalent power (NEP) and specific detectivity (D*) of the triple-band device will be modeled. The results should be compared with the background-limited performance, ensuring that the device meets or exceeds the minimum sensitivity required for its intended applications. Lastly, the impact of parasitic absorption caused by bias illumination on the NEP and specific detectivity for each band should be assessed to optimize the device's performance under various operating conditions. A novel design that uses both PIN and nBn structures, and a combined polarity and optical addressing for a tri-band photodetector whose major advantage of this design is that it needs only one LED can be attempted in the future.

Future research needs to focus on refining the MBE growth parameters to achieve monocrystalline WZ CdSe thin films, aimed at enhancing their suitability for solar cell applications. The MgCdSe/CdSe double-heterostructure can be further developed to demonstrate the complete device with expected high V_{OC} and external quantum efficiency.

REFERENCES

[1] Z. I. Alferov, "Nobel lecture: The double heterostructure concept and its applications in physics, electronics, and technology," *Rev. Mod. Phys.* **73**, no. 3, pp. 767–782, 2001

[2] L. Esaki and R. Tsu, "Superlattice and Negative Differential Conductivity in Semiconductors," *IBM J. Res. Dev.* **14,** no. 1, pp. 61–65, 1970

[3] H. Schneider and H. C. Liu, *Quantum Well Infrared Photodetectors*. 2007

[4] A. Y. Cho and J. R. Arthur, "Molecular beam epitaxy," *Prog. Solid-State Chem.* **10**, no. 3, pp. 157–191, 1975

[5] Q. Liu, X. Zhang, L. B. Abdalla, and A. Zunger, "Transforming Common III-V and II-VI Semiconductor Compounds into Topological Heterostructures: The Case of CdTe/InSb Superlattices," *Adv. Funct. Mater.* **26**, no. 19, pp. 3259–3267, 2016

[6] M. Razeghi and B. M. Nguyen. "Advances in Mid-Infrared Detection and Imaging: a Key Issues Review." *Reports on progress in physics* **77**, no. 8, 2014

[7] A. Rogalski, "Infrared Detectors: An Overview." *Infrared physics & technology* **43**, no. 3, 2002

[8] A. Rogalski, Infrared Detectors. Amsterdam: Gordon & Breach, 2000.

[9] W.D. Lawson, S. Nielsen, E.H. Putley and A.S. Young, "Preparation and Properties of HgTe and Mixed Crystals of HgTe-CdTe." *The Journal of Physics and Chemistry of Solids* **9**, no. 3, 1959

[10] A. Rogalski, M. Kopytko, P. Martyniuk, and W. Hu. "Comparison of Performance Limits of the HOT HgCdTe Photodiodes with Colloidal Quantum Dot Infrared Detectors." *Bulletin of the Polish Academy of Sciences. Technical sciences* **68**, no. 4, 2020

[11] M. Kinch, A. *Fundamentals of Infrared Detector Materials*. 1st ed. Vol. v.TT76. Berlin: SPIE, 2007

[12] J. Schulman and T. Mcgill, "CdTe-HgTe super-lattice - proposal for a new infrared material." *Appl. Phys. Lett.* **34** (10), 663–665, 1979

[13] G. A. Sai-Halasz, R. Tsu, and L. Esaki, "A new semiconductor superlattice," *Appl. Phys. Lett.* **30**, no. 12, pp. 651–653, 1977

[14] H. Sakaki, L. L. Chang, G. A. Sai-Halasz, C. A. Chang, and L. Esaki, "Two-

dimensional electronic structure in InAs-GaSb superlattices," *Solid State Commun.* **26**, pp. 589–592, 1978.

[15] P. Martyniuk and A. Rogalski. "Performance Comparison of Barrier Detectors and HgCdTe Photodiodes." *Optical Engineering* **53**.10: 106105-106105. 2014

[16] J. B. Rodriguez, P. Christol, L. Cerutti, F. Chevrier, and A. Joullié, "MBE growth and characterization of type-II InAs/GaSb superlattices for mid-infrared detection," *J. Cryst. Growth* **274**, no. 1–2, pp. 6–13, 2005

[17] E. H. Steenbergen, B. C. Connelly, G. D. Metcalfe, H. Shen, M. Wraback, D. Lubyshev, Y. Qiu, J. M. Fastenau, A. W. K. Liu, S. Elhamri, O. O. Cellek and Y.-H. Zhang, Y.-H, "Significantly improved minority carrier lifetime observed in a long-wavelength infrared III-V type-II superlattice comprised of InAs/InAsSb," *Appl. Phys. Lett.* **99**, p. 251110, 2011

[18] D. Donetsky, S. P. Svensson, L. E. Vorobjev, and G. Belenky, "Carrier lifetime measurements in short-period InAs/GaSb strained-layer superlattice structures," *Appl. Phys. Lett.* **95**, no. 21, pp. 14–17, 2009.

[19] Tsai, Cheng-Ying. "Vertical Carrier Transport Properties and Device Application of InAs/$InAs_{1-x}Sb_x$ Type-II Superlattice and a Water-Soluble Lift-Off Technology". *Thesis (Ph.D.)*--Arizona State University, 2020.

[20] C.-Y. Tsai, Y. Zhang, Z. Ju, and Y.-H. Zhang, "Study of vertical hole transport in InAs/InAsSb type-II superlattices by steady-state and time-resolved photoluminescence spectroscopy," *Appl. Phys. Lett.*, vol. 116, no. 20, p. 201108, 2020.

[21] A. D. Prins, M. K. Lewis, Z. L. Bushell, S. J. Sweeney, S. Liu, and Y.-H. Zhang, Evidence for a defect level above the conduction band edge of InAs/InAsSb type-II superlattices for applications in efficient infrared photodetectors, *Appl. Phys. Letts.* **106**, 171111(2015).

[22] E. H. Steenbergen, B. C. Connelly, G. D. Metcalfe, H. Shen, M. Wraback, D. Lubyshev, Y. Qiu, JM. Fastenau, A.W.K. Liu, S. Elhamri, O. O. Cellek and Y.-H Zhang,"Significantly improved minority carrier lifetime observed in a long-wavelength infrared III-V type-II superlattice comprised of InAs/InAsSb, *Appl. Phys. Lett*. **99**, p. 251110, 2011.

[23] A. Rogalski , P. Martyniuk, M. Kopytko, P. Madejczyk, and S. Krishna. "InAsSb-Based Infrared Photodetectors: Thirty Years Later On." *Sensors (Basel, Switzerland)* **20**, no. 24, 2020

[24] D. H. Wu, A. Dehzangi, Y. Y. Zhang, and M. Razeghi. "Demonstration of Long Wavelength Infrared Type-II InAs/$InAs_{1-x}Sb_x$ Superlattices Photodiodes on GaSb Substrate Grown by Metalorganic Chemical Vapor Deposition." *Appl. Phys. Lett.* **112**, no. 24, 2018

[25] D. H. Wu, Q. Durlin, A. Dehzangi, Y. Zhang, and M. Razeghi. "High Quantum Efficiency Mid-Wavelength Infrared Type-II InAs/$InAs_{1-x}Sb_x$ Superlattice Photodiodes Grown by Metal-Organic Chemical Vapor Deposition." *Appl. Phys. Lett.* **114**, no. 1, 2019

[26] H.S. Kim, O.O. Cellek, Z.-Y. Lin, Z. -Y He, X. -H. Zhao, S. Liu, H. Li, and Y.-H. Zhang. "Long-Wave Infrared nBn Photodetectors Based on InAs/InAsSb Type-II Superlattices." *Appl. Phys. Lett.* **101**, no. 16, 2012

[27] A. Khoshakhlagh, J. B. Rodriguez, E. Plis, G. D. Bishop, Y. D. Sharma, H. S. Kim, L. R. Dawson, and S. Krishna. "Bias Dependent Dual Band Response from InAs/Ga(In)Sb Type II Strain Layer Superlattice Detectors." *Appl. Phys. Lett.* **91**, no. 26, 2007

[28] E. Plis, S. A. Myers, D. A. Ramirez, and S. Krishna. "Development of Dual-Band Barrier Detectors." In *Proceedings of SPIE - The International Society for Optical Engineering*, 9819:981911–981911–6. SPIE, 2016

[29] A. Haddadi, R. Chevallier, G. Chen, A.M. Hoang, and M. Razeghi. "Bias-Selectable Dual-Band Mid-/long-Wavelength Infrared Photodetectors Based on InAs/$InAs_{1-x}Sb_x$ Type-II Superlattices." *Appl. Phys. Lett.* **106**, no. 1, 2015

[30] A. Haddadi, A. Dehzangi, R. Chevallier, S. Adhikary, and M. Razeghi. "Bias-Selectable nBn Dual-Band Long-/very Long-Wavelength Infrared Photodetectors Based on InAs/$InAs_{1-x}Sb_x$/$AlAs_{1-x}Sb_x$ Type-II Superlattices." *Scientific reports* **7**, no. 1, 2017

[31] A.M. Hoang., G. Chen, R. Chevallier, A. Haddadi, and M. Razeghi. "High Performance Photodiodes Based on InAs/InAsSb Type-II Superlattices for Very Long Wavelength Infrared Detection." *Appl. Phys. Lett.* **104**, no. 25, 2014

[32] A. Haddadi, G. Chen, R. Chevallier, A.M. Hoang, and M. Razeghi. "InAs/$InAs_{1-x}Sb_x$ Type-II Superlattices for High Performance Long Wavelength Infrared Detection." *Appl. Phys. Lett.* **105**, no. 12, 2014.

[33] A. Haddadi, A. Dehzangi, S. Adhikary, R. Chevallier, and M. Razeghi. "Background–limited Long Wavelength Infrared InAs/$InAs_{1-x}Sb_x$ Type-II Superlattice-Based Photodetectors Operating at 110 K." *APL materials* **5**, no. 3 2017

[34] Teledyne Judson Technologies. MWIR InAsSb SLS Detectors. Available online: http://www.teledynejudson.com/news/Documents/TJT%20SLS%20detector%20data%20charts%2009192017%20Final%20101317.pdf, 2020

[35] J. -P. Perez, Q. Durlin, C. Cervera, and P. Christol. "New Ga-Free InAs/InAsSb Superlattice Infrared Photodetector." In *PHOTOPTICS 2018 - Proceedings of the 6th International Conference on Photonics, Optics and Laser Technology*, 2017-:232–237, 2017

[36] D. -Z. Ting, A. Soibel, A. Khoshakhlagh, Sir B. Rafol, S. A. Keo, L. Höglund, A. M. Fisher, E. M. Luong, and S. D. Gunapala. "Mid-Wavelength High Operating Temperature Barrier Infrared Detector and Focal Plane Array." *Appl. Phys. Lett.* **113**, no. 2, 2018

[37] Q. Durlin, J.P. Perez, L. Cerutti, J.B. Rodriguez, T. Cerba, T. Baron, E. Tournié, and P. Christol. "Midwave Infrared Barrier Detector Based on Ga-Free InAs/InAsSb Type-II Superlattice Grown by Molecular Beam Epitaxy on Si Substrate." *Infrared physics & technology* **96**, 2019

[38] D. H. Wu, J. Li, A. Dehzangi, and M. Razeghi. "Mid-Wavelength Infrared High Operating Temperature pBn Photodetectors Based on Type-II InAs/InAsSb Superlattice." *AIP advances* **10**, no. 2, 2020

[39] E. Delli , V. Letka, P. D. Hodgson, E. Repiso, J. P. Hayton, A. P. Craig, Q. Lu, R. Beanland, A. Krier, A. R. J. Marshall and P. J. Carrington, "Mid-Infrared InAs/InAsSb Superlattice nBn Photodetector Monolithically Integrated onto Silicon." *ACS photonics* **6**, no. 2, 2019

[40] D. H. Wu, A. Dehzangi, J, Li, and M. Razeghi. "High Performance Zn-Diffused Planar Mid-Wavelength Infrared Type-II InAs/InAs1−xSbx Superlattice Photodetector by MOCVD." *Appl. Phys. Lett.* **116**, no. 16, 2020

[41] J. W. Kim, H. Yuan, J. Kimchi, J. Lei, E. Rangel, P. Dreiske, and A. Ikhlassi. "HOT MWIR InAs/InAsSb T2SL Discrete Photodetector Development." In *Proceedings of SPIE - The International Society for Optical Engineering*, 10624:1062412–1062412–8. SPIE, 2018

[42] D. Lubyshev , J. M. Fastenau, M. Kattner, P. Frey, S. A. Nelson, R. Flick, M. Rogers, Amy W.K. Liu, Patrick Flint, and Nikolai Faleev. "Effect of Substrate Orientation on Sb-Based MWIR Photodetector Characteristics." *Infrared physics & technology* **95** 2018

[43] A. Haddadi, X.V. Suo, S. Adhikary, P. Dianat, R. Chevallier, A.M. Hoang, and M. Razeghi. "High-Performance Short-Wavelength Infrared Photodetectors Based on Type-II InAs/$InAs_{1-x}Sb_x$/$AlAs_{1-x}Sb_x$ Superlattices." *Appl. Phys. Lett.* **107**, no. 14

(2015).

[44] E. Rosencher, A. Fiore, B. Vinter, V. Berger, Ph. Bois, and J. Nagle, "Quantum engineering of optical nonlinearities", *Science* **271**, 168-173, 1996

[45] L. C. West and S. J. Eglash, "First observation of an extremely large-dipole infrared transition within the conduction band of a GaAs quantum well", *Appl. Phys. Lett.* **46**, 1156-1158, 1985

[46] B. F. Levine, "Bond-Charge Calculation of Nonlinear Optical Susceptibilities for Various Crystal Structures", *Phys. Rev. B* **7**, 2600-2626, 1973

[47] F. Capasso and A. Y. Cho, "Bandgap engineering of semiconductor heterostructures by molecular beam epitaxy: physics and applications", *Surf. Sci.* **299/300**, 878-891, 1994

[48] M. M. Fejer, S. J. B. Yoo, R. L. Byer, A. Harwit, and J. S. Harris Jr, "Observation of extremely large quadratic susceptibility at 9.6-10.8 μm in electric-field-biased AlGaAs quantum wells", *Phys. Rev. Lett.* **62**, 1041-1044, 1989

[49] E. Rosencher, P. Bois, J. Nagle, and S. Delattre, "Second harmonic generation by intersub-band transitions in compositionally asymmetrical MQWs", *Electronics Letters* **25**, 1063-1065, 1989

[50] C. Sirtori, F. Capasso, D. L. Sivco, S. N. G. Chu, and A. Y. Cho, "Observation of large second order susceptibility via intersubband transitions at $\lambda \sim 10$ μm in asymmetric coupled AlInAs/GaInAs quantum wells", *Appl. Phys. Lett.* **59**, 2302-2304, 1991

[51] L. C. Lew Yan Voon and L. R. Ram-Mohan, "Calculations of second-order nonlinear optical susceptibilities in III-V and II-VI semiconductor heterostructures", *Phys. Rev. B* **50** (19), 14421-14434, 1994

[52] A. Mekawy and A. Alù, "Giant midinfrared nonlinearity based on multiple quantum well polaritonic metasurfaces", *Nanophotonics* **10**, 667-678, 2021

[53] N. D. Foster, A. K. Rockwell, J. A. McArthur, B. S. Mendoza, S. R. Bank, and M. C. Downer, "A Study of Second-Order Susceptibility in Digital Alloy-Grown InAs/AlSb Multiple Quantum Wells", *Adv. Optical Mater*. 2102845, 2022

[54] J. R. Meyer, C. A. Hoffman, F. J. Bartoli, and L. R. Ram-Mohan, "Intersubband second-harmonic generation with voltage-controlled phase matching", *Appl. Phys. Lett*. **67**, 608-610, 1995

[55] H. Xie, L. R. Friedman, and L. R. Ram-Mohan, "Nonlinear optical properties of

GaAs/$Ga_{1-x}Al_xAs$ superlattices", *Phys. Rev. B* **42** (11), 7124-7131, 1990

[56] I. Vurgaftman, J. R. Meyer, and L. R. Ram-Mohan, "Optimized Second-Harmonic Generation in Asymmetric Double Quantum Wells", *IEEE J. Quant. Elec* **32** (8), 1334-1346, 1996

[57] J. Khurgin, "Second-order nonlinear effects in asymmetric quantum-well structures", *Phys. Rev. B* **38** (6), 4056-4066, 1988

[58] A. Soriano, E. A. Navarro, J. A. Portí, and V. Such, "Analysis of the finite difference time domain technique to solve the Schrodinger equation for quantum devices", *J. Appl. Phys.* **95** (12) 8011-8018, 2004

[59] R. W. Boyd, "Nonlinear Optics," 4th Ed. (Elsevier Inc, 2020).

[60] D. Ding, S R Johnson, S.-Q Yu, S.-N Wu, and Y.-H Zhang. "A Semi-Analytical Model for Semiconductor Solar Cells." *J. Appl. Phys.***110**, no. 12, 2011

[61] W. Shan, W. Walukiewicz, J.W. Ager III, K.M. Yu, J. Wu, and E.E. Haller. "Pressure Dependence of the Fundamental Band-Gap Energy of CdSe." *Appl. Phys. Lett.* **84**, no. 1, 2004

[62] K. Li, X. Lin, B. Song, R. Kondrotas, C. Wang, Y. Lu, X. Yang, C. Chen, and J. Tangm "Rapid Thermal Evaporation for Cadmium Selenide Thin-Film Solar Cells." *Frontiers of Optoelectronics (Online)* **14**, no. 4, 2021

[63] J. Gutowski, K. Sebald and T. Voss, Semiconductors, vol. 44B (Berlin: Springer) p. 75, 2009

[64] J. Ma, D. Kuciauskas, D. Albin, R. Bhattacharya, M. Reese, T. Barnes, J. V. Li, T. Gessert, and S.-H. Wei, "Dependence of the Minority-Carrier Lifetime on the Stoichiometry of CdTe Using Time-Resolved Photoluminescence and First-Principles Calculations." *Phys. Rev. Lett.* **111**, no. 6, 2013

[65] S. Ninomiya and S. Adachi. "Optical Properties of Cubic and Hexagonal CdSe." *J. Appl. Phys.* **78,** no. 7, 1995

[66] B. Bagheri, Research project to study cadmium selenide (CdSe) solar cells, Iowa State University, 2020

[67] Plant PV Inc., "Low Cost, Epitaxial Growth of II-VI Materials for Multijunction Photovoltaic Cells", 2014

[68] A. V. Shaikh, S. G. Sayyed, S. Naeem, S. F. Shaikh, and R. S. Mane, "Electrodeposition of n-CdSe/p-Cu2Se Heterojunction Solar Cells." *Engineered Science* **13**, 2021

[69] A.W. Stevenson and Z. Barnea, "Anharmonic Thermal Vibrations and the Position Parameter in Wurtzite Structures; II, Cadmium Selenide." *Acta crystallographica* **40**, no. 6, 1984

[70] E.T. Simola, V. Kiyek, A. Ballabio, V. Schlykow, J. Frigerio, C. Zucchetti, A. D. Iacovo, L. Colace, Y. Yamamoto, G. Capellini, D. Grützmacher, D. Buca and G. Isella, "CMOS-Compatible Bias-Tunable Dual-Band Detector Based on GeSn/Ge/Si Coupled Photodiodes." *ACS photonics* **8**, no. 7, 2021

[71] W.H. Rolls, "TWO-COLOR INFRARED DETECTOR." *Electro Opt Syst Des* **9**, no. 11 (n.d.): 10–13, 1977

[72] J.C. Campbell, T.P. Lee, A.G. Dentai, and C.A. Burrus. "Dual-Wavelength Demultiplexing InGaAsP Photodiode." *Appl. Phys. Lett* **34**, no. 6, 1979

[73] M.J. Sun, W.S.C. Chang, and C.M. Wolfe. "Frequency Demultiplexing in GaAs EAP Waveguide Detectors." *Applied Optics* **17**, no. 22, 1978

[74] E.F. Schulte, *Two Terminal Multi-Band Infrared Radiation Detector*, United States Patent 5113,076, 1992

[75] E. R. Blazejewski, J. M. Arias, G. M. Williams, W. McLevige, M. Zandian, and J. Pasko. "Bias-switchable Dual-band HgCdTe Infrared Photodetector." In *Journal of Vacuum Science & Technology B: Microelectronics and Nanometer Structures* **10**:1626–1632. WOODBURY: Amer Inst Physics, 1992.

[76] A. Rogalski, "New Material Systems for Third Generation Infrared Photodetectors." *Opto-electronics review* **16**, no. 4, 2008

[77] K. Kosai, *Three Band and Four Band Multispectral Structures having Two Simultaneous Signal Outputs*, United States Patent 5731,621, 24 March 1998.

[78] T. Chu, *Multi-color Coincident Infrared Detector*, United States Patent 5059,786, 22 October 1991.

[79] E. H. Steenbergen, M J DiNezza, W H. G Dettlaff, S H Lim, and Y.-H Zhang. "Optically-Addressed Two-Terminal Multicolor Photodetector." *Appl. Phys. Lett* **97**, no. 16, 2010

[80] O.O. Cellek, J.L. Reno, and Y.-H. Zhang. "Optically Addressed Near and Long-Wave Infrared Multiband Photodetectors." *Appl. Phys. Lett* **100**, no. 24 (2012).

[81] O.O. Cellek, and Y.-H. Zhang. “Optically Addressed Multiband Photodetector for Infrared Imaging Applications.” In *Proceedings of SPIE - The International Society for Optical Engineering*. Vol. 8268, 2012.

[82] Z. Ju, A. McMinn, X. Qi, X. Liu, S. Schaefer, T. McCarthy, and Y.-H Zhang, “Optically-Addressed Monolithically-Integrated Multi-band Photodetectors Using Type-II Superlattice Materials”, *37th North American Conference on Molecular Beam Epitaxy*, Madison, WI, 2023

[83] Z. Ju, A. McMinn, X. Qi, X. Liu, S. Schaefer, T. McCarthy, and Y.-H Zhang, “The Design of Optically-Addressed Monolithically-Integrated Multiband Photodetectors Using Type-II Superlattice Materials”, *16th International Conference on Mid-Infrared Optoelectronics: Materials and Devices (MIOMD)*, Oklahoma City, OK, 2023

[84] G. Stollwerck, O.V. Sulima, and A.W. Bett, “Characterization and Simulation of GaSb Device-Related Properties,” *IEEE Transactions on Electron Devices* **47**, no. 2, pp. 448-457, 2000

[85] S. Adachi. *Properties of Group-IV, III-V and II-VI Semiconductors*. **1**. Aufl. Vol. 16. Newark: Wiley, 2005.

[86] P. C. Klipstein, Y. Livneh, A. Glozman, S. Grossman, O. Klin, N. Snapi, and E. Weiss, “Modeling InAs/GaSb and InAs/InAsSb Superlattice Infrared Detectors.” *Journal of electronic materials* **43**, no. 8, 2014

[87] D. Z. Ting, Sir B. Rafol, A. Khoshakhlagh, A. Soibel, S. A. Keo, A. M. Fisher, B. J. Pepper, C. J. Hill, and S. D. Gunapala. “InAs/InAsSb Type-II Strained-Layer Superlattice Infrared Photodetectors.” *Micromachines (Basel)* **11**, no. 11, 2020

[88] I. Vurgaftman, G. Belenky, Y. Lin, D. Donetsky, L. Shterengas, G. Kipshidze, W. L. Sarney, and S. P. Svensson. “Interband Absorption Strength in Long-Wave Infrared Type-II Superlattices with Small and Large Superlattice Periods Compared to Bulk Materials.” *Appl. Phys. Lett* **108**, no. 22, 2016

[89] J.W. Matthews, and A.E. Blakeslee. “Defects in Epitaxial Multilayers.” *J. Cryst. Growth.* **27**, 1974

[89] N. J Ekins-Daukes, K. Kawaguchi, and J. Zhang. “Strain-Balanced Criteria for Multiple Quantum Well Structures and Its Signature in X-Ray Rocking Curves.” *Crystal growth & design* **2**, no. 4, 2002

[90] J. Khurgin, “Second-Order Intersubband Nonlinear-Optical Susceptibilities of Asymmetric Quantum-Well Structures.” *Journal of the Optical Society of America. B, Optical physics* **6**, no. 9, 1989

[91] J. Khurgin, "Second-Order Susceptibility of Asymmetric Coupled Quantum Well Structures." *Appl. Phys. Lett* **51**, no. 25, 1987

[92] Z. Ju, S. Schaefer, J. Khurgin and Y.-H Zhang, "Enhanced Second-order Nonlinear Susceptibility in Asymmetric Type-II Quantum wells", *SPIE Photonics West*, 12405-48, San Fransico, CA, 2023

[93] A. Soriano, E. A. Navarro, J. A. Portí, and V. Such. "Analysis of the Finite Difference Time Domain Technique to Solve the Schrödinger Equation for Quantum Devices." *J. Appl. Phys* **95**, no. 12, 2004

[94] S.-L. Chuang, *Physics of Optoelectronic Devices*. New York: Wiley, 1995.

[95] S. Houver, A. Lebreton, T.A.S. Pereira, G. Xu, R. Colombelli, I. Kundu, L.H. Li, E.H linfield, A.G. Davies, J. Mangeney, R. Ferreira and S.S. Dhillon, "Giant Optical Nonlinearity Interferences in Quantum Structures." *Science advances* **5**, no. 10, 2019

[96] I. Shoji, Takashi Kondo, Ayako Kitamoto, Masayuki Shirane, and Ryoichi Ito. "Absolute Scale of Second-Order Nonlinear-Optical Coefficients." *Journal of the Optical Society of America. B, Optical physics* **14**, no. 9, 1997

[97] Phillips, J.C., and J.A. Van Vechten. "Nonlinear Optical Susceptibilities of Covalent Crystals." *Physical review* **183**, no. 3, 1969

[98] Z. Ju, X. Qi, S. Schaefer, M. McCartney, D. Smith, A. McMinn, T. McCarthy, A.V.G Chizmeshya, S. Grover, and Y.-H Zhang, "Structural and Optical Properties of CdSe grown on InAs", 36th North American Conference on Molecular Beam Epitaxy, Rehoboth Beach, DE, 2022

[99] S. Schaefer, Z. Ju, X. Qi, A. McMinn, and Y.-H. Zhang, "Molecular Beam Epitaxy Growth of CdSe for Si-based Tandem Cell Application", *The 21st International Conference on Molecular Beam Epitaxy*, Sheffield, UK, 2022

[100] P. D. Lao, Y. Guo, G.G. Siu, and S.C. Shen. "Optical-Phonon Behavior in $Zn_{1-x}Mn_xSe$: Zinc-Blende and Wurtzite Structures." *Phys. Rev. B, Condensed matter* **48**, no. 16, 1993

[101] A. J. C. Wilson, "International Tables for X-Ray Crystallography. Volume III. Physical and Chemical Tables Edited by K. Lonsdale (General Editor), C. H. MacGillavry and G. D. Rieck." *Acta Crystallographica*. 5 Abbey Square, Chester, Cheshire CH1 2HU, England: Blackwell Publishing Ltd, 1963.

[102] E. Deligoz, K. Colakoglu, and Y. Ciftci. "Elastic, Electronic, and Lattice Dynamical Properties of CdS, CdSe, and CdTe." *Physica. B, Condensed matter* **373**, no. 1, 2006

[103] N. Samarth, H. Luo, J.K. Furdyna, S.B. Qadri, Y.R. Lee, A.K. Ramdas, and N. Otsuka. “Growth of Cubic (zinc Blende) CdSe by Molecular Beam Epitaxy.” *Appl. Phys. Lett* **54**, no. 26, 1989

[104] Q. Yang, J. Zhao, M. Guan, C. Liu, D. Han and Y. Zeng, “Growth and Annealing of Zinc-Blende CdSe Thin Films on GaAs (0 0 1) by Molecular Beam Epitaxy.” *Appl. Surf. Scie.* **257**, no. 21, 2011

[103] G. Kresse, and J. Hafner. “Ab Initio Molecular Dynamics for Liquid Metals.” *Phys. Rev. B, Condensed matter* **47**, no. 1, 1993

[104] G. Kresse and J. Furthmüller. “Efficiency of Ab-Initio Total Energy Calculations for Metals and Semiconductors Using a Plane-Wave Basis Set.” *Computational materials science* **6**, no. 1, 1996

[105] G. Kresse and D. Joubert. “From Ultrasoft Pseudopotentials to the Projector Augmented-Wave Method.” *Phys. Rev. B, Condensed matter* **59**, no. 3, 1999

[106] K.K. Zhuravlev, “PbSe Vs. CdSe: Thermodynamic Properties and Pressure Dependence of the Band Gap.” *Physica. B, Condensed matter* **394**, no. 1, 2007

[107] T. Lei, M. Fanciulli, R.J. Molnar, T.D. Moustakas, R.J. Graham, and J. Scanlon. “Epitaxial Growth of Zinc Blende and Wurtzitic Gallium Nitride Thin Films on (001) Silicon.” *Appl. Phys. Lett* **59**, no. 8, 1991

[108] A. Yoshikawa, E. Ohshima, T. Fukuda, H. Tsuji, and K. Oshima. “Crystal Growth of GaN by Ammonothermal Method.” *J. Cryst. Growth.* **260**, no. 1, 2004

[109] D. Kriegner, C. Panse, B. Mandl, K. A. Dick, M. Keplinger, J. M. Persson, P. Caroff, D. Ercolani, L. Sorba, F. Bechstedt, J. Stangl, and G. Bauer, “Unit Cell Structure of Crystal Polytypes in InAs and InSb Nanowires.” *Nano letters* **11**, no. 4, 2011

[110] M. I. McMahon and R. J. Nelmes, “Observation of a Wurtzite Form of Gallium Arsenide.” *Phys. Rev. Lett.* **95**, no. 21, 2005

APPENDIX A

ARCHIVAL JOURNAL PAPERS

1. **Z. Ju**, X. Qi, S. Schaefer, M. McCartney, D. Smith, A.V.G Chizmeshya, A. McMinn, T. McCarthy, S. Grover, and Y.-H Zhang, "CdSe with Mixed Zincblende and Wurtzite Phases Grown on Lattice-Matched InAs Substrates Using Molecular Beam Epitaxy", submitted to *Applies Physics Letter Material, 2023*

2. S. Schaefer, **Z. Ju***, X. Liu, X. Qi, J. Khurgin and Y.-H Zhang, "Enhanced Second-Order Nonlinear Susceptibility in Type-II Asymmetric Quantum Well Structures", submitted to *Applies Physics Letter, 2023*

3. H. N. Abbasi, X. Qi, J. Gong, **Z. Ju**, S. Min, Y.-H Zhang and Z. Ma, "Passivation of CdTe/MgCdTe double heterostructure by dielectric thin films deposited using atomic layer deposition", *Journal of Applied Physics* 134, 135304, 2023

4. T. McCarthy, **Z. Ju**, S. Schaefer, S.-Q Yu, and Y.-H Zhang. "Momentum(k)-Space Carrier Separation Using SiGeSn Alloys for Photodetector Applications" *Journal of Applied Physics* 130, 223102, 2021

5. J. Ding, C.-Y. Tsai, **Z. Ju,** and Y.-H Zhang, "Epitaxial lift-off CdTe/MgCdTe double heterostructures for thin-film and flexible solar cells applications", *Applies Physics Letter*, vol. 118, no. 18, 181101, 2021

6. C.-Y. Tsai, Y. Zhang, **Z. Ju,** and Y.-H Zhang, "Study of vertical hole transport in InAs/InAsSb type-II superlattices by steady-state and time-resolved photoluminescence spectroscopy," *Applies Physics Letter*, vol. 116, no. 20, 201108, 2020

7. W. Zhang, **Z. Ju,** and W. Wu, "Intrinsic superstructure near atomically clean armchair step edges of graphite", *Physical Review B,*115120, 2019

APPENDIX B

ARCHIVAL CONFERENCE PUBLICATIONS

1. **Z. Ju**, X. Qi, A. McMinn, X. Liu, and Y.-H Zhang, "Optically-Addressed Monolithically-Integrated Multi-band Photodetectors Using Type-II Superlattice Materials", SPIE Photonics West, 12895-24, San Fransico, CA, 2024 (Oral *Accepted*)

2. **Z. Ju**, A. McMinn, X. Qi, X. Liu, S. Schaefer, T. McCarthy, and Y.-H Zhang, "Optically-Addressed Monolithically-Integrated Multi-band Photodetectors Using Type-II Superlattice Materials", 37th North American Conference on Molecular Beam Epitaxy, Madison, WI, 2023 (Oral)

3. **Z. Ju**, A. McMinn, X. Qi, X. Liu, S. Schaefer, T. McCarthy, and Y.-H Zhang, "The Design of Optically-Addressed Monolithically-Integrated Multiband Photodetectors Using Type-II Superlattice Materials", 16th International Conference on Mid-Infrared Optoelectronics: Materials and Devices (MIOMD), Oklahoma City, OK, 2023 (Oral)

4. **Z. Ju**, S. Schaefer, J. Khurgin and Y.-H Zhang, "Enhanced Second-order Nonlinear Susceptibility in Asymmetric Type-II Quantum wells", SPIE Photonics West, 12405-48, San Fransico, CA, 2023 (Oral)

5. **Z. Ju**, X. Qi, S. Schaefer, M. McCartney, D. Smith, A. McMinn, T. McCarthy, A.V.G Chizmeshya, S. Grover, and Y.-H Zhang, "Structural and Optical Properties of CdSe grown on InAs", 36th North American Conference on Molecular Beam Epitaxy, Rehoboth Beach, DE, 2022 (Oral)

6. **Z. Ju**, C.-Y Tsai, and Y.-H Zhang, "InAs/InAsSb Type-II Superlattice Barrier Infrared Photodetectors", Laser Components-LC talks, 1st Global Infrared Sessions, 2020 (Oral)

7. **Z. Ju**, W. Zhang, and W. Wu, "LT-STM/STS Studies of Clean Graphene Armchair Edge", APS March Meeting, Baltimore, MD, 2016 (Oral)

8. T. McCarthy, **Z. Ju**, X. Qi, A. McMinn, S.-Q. Yu, and Y.-H. Zhang, "Molecular Beam Growth and Characterization of SiGeSnPb Group-IV alloys", Tri-Service Workshop on GeSn and GeSiSn, Datyon, OH, 2023

9. T. McCarthy, R. Basnet, **Z. Ju**, X. Qi, A. McMinn, J. Hu, S.-Q. Yu, and Y.-H. Zhang. "Molecular Beam Epitaxy Grown Group-IV Alloys for Infrared Photodetector and Quantum Transport Applications." 37th North American Conference on Molecular Beam Epitaxy, Madison, WI, 2023

10. T. McCarthy, R. Basnet, **Z. Ju**, J. Hu, S.-Q. Yu, and Y.-H. Zhang, "SiGeSn Alloys: From MBE Growth to Quantum Transport and Photodetector Applications", Compound Semiconductor Week Workshop (CSW), Jeju, Korea, 2023

11. T. McCarthy, **Z. Ju**, S. Schaefer, S.-Q. Yu, and Y.-H. Zhang, "Momentum(k)-Space Carrier Separation Using SiGeSn Alloys for Photodetector Applications", Tri-Service Workshop on GeSn and GeSiSn, Dayton, OH, 2023

12. T. McCarthy, **Z. Ju**, A. McMinn, R. Kodama, F. Aqariden, P.-K. Liao, P. Mitra and Y.-H. Zhang. "CdTe/InSb(211) Virtual Substrates for IR Detector Applications." The US Workshop on the Physics & Chemistry of II-VI Materials, Tampa, FL, 2022

13. T. McCarthy, **Z. Ju**, S. Schaefer, X. Qi, A. McMinn, S.-Q. Yu, and Y.-H. Zhang. "Molecular Beam Epitaxy Grown Group-IV Alloys: Ideal Candidate for Momentum(k)-Space Carrier Separation Photodetectors.", The 36th North American Conference on Molecular Beam Epitaxy, Rehoboth Beach, DE, 2022

14. S. Schaefer, **Z. Ju**, X. Qi, A. McMinn, and Y.-H. Zhang, "Molecular Beam Epitaxy Growth of CdSe for Si-based Tandem Cell Application", The 21st International Conference on Molecular Beam Epitaxy, Sheffield, UK, 2022

15. T. McCarthy, R. Basnet, **Z. Ju**, A. McMinn, J. Hu, S.-Q. Yu, and Y.-H. Zhang. "α-Sn and $Sn_{1-x}Ge_x$ Thin Films Grown on CdTe/InSb(100) Substrate." The 21st International Conference on Molecular Beam Epitaxy", The 21st International Conference on Molecular Beam Epitaxy, Sheffield, UK, 2022

16. X. Qi, J. Ding, **Z. Ju**, S. Schaefer, and Y.-H. Zhang, "Flexible CdTe/MgCdTe Double-Heterostructure Solar Cells Made from Epitaxial Lift-off Thin Films", IEEE 49th Photovoltaics Specialists Conference, Philadelphia, PA, 2022

17. S. Schaefer, **Z. Ju**, X. Qi, A. McMinn, and Y.-H. Zhang, "Molecular Beam Epitaxy Growth of CdSe for Si-based Tandem Cell Application", IEEE 49th Photovoltaics Specialists Conference, Philadelphia, PA, 2022

18. T. McCarthy, **Z. Ju**, X. Qi, A. McMinn, M. McCartney, S. Schaefer, A. Chizmeshya, D.J. Smith, S. Grover, and Y.-H. Zhang, "Molecular Beam Epitaxy Growth of CdSe for Si-based Tandem Cell Application" – Industry Advisory Board Meeting for the IUCRC for a Solar Powered Future (SPF2050), Boulder, CO, 2022

19. T. McCarthy, **Z. Ju**, S. Schaefer, S.-Q. Yu, and Y.-H. Zhang, "Momentum (k)-Space Carrier-Separation Infrared Photodetectors Using SiGeSn Alloys" – The 15th International Conference on Mid-Infrared Optoelectronics: Materials and Devices, Surrey, UK, 2021

20. T. McCarthy, **Z. Ju**, S.-Q. Yu, and Y.-H. Zhang, "Momentum (k)-Space Carrier-Separation Infrared Photodetectors Using SiGeSn Alloys", IEEE Photonics Series Summer Topical (Virtual), 2021

21. R. Basnet, T. McCarthy, **Z. Ju**, Y.-H. Zhang, S.-Q, Yu, and J. Hu " Electronic Properties of Group-IV SnGe Alloy Topological Quantum Materials", IEEE Photonics Series Summer Topical (Virtual), 2021

22. C.-Y. Tsai, Y. Zhang, **Z. Ju**, and Y.-H. Zhang, "Vertical hole transport in $InAs/InAs_xSb_{1-x}$ type-II superlattices," presented at the 35th North American Conference on Molecular Beam Epitaxy, Ketchum, ID, USA, 2019.

APPENDIX C

PATENT

1. Y.-H. Zhang, X. Qi, Z. Ju, J. Ding, T. McCarthy, S. Schaefer. “Contacts of Solar Cells and other Optoelectronic devices”, US2023021591A1 (*Pending*)